Non-equilibrium self-assembly processes of complex dipolar colloids

vorgelegt von:
Diplomphysiker
Florian Kogler
aus
Ulm, Baden-Württemberg

Von der Fakultät II – Mathematik und Naturwissenschaften
der Technische Universität Berlin
zur Erlangung des akademischen Grades
Doktor der Naturwissenschaften
Dr. rer. nat.

genehmigte Dissertation

Promotionsausschuss:

Vorsitzender:	Prof. Dr. Martin Schoen
1. Gutachterin:	Prof. Dr. Sabine H. L. Klapp
2. Gutachter:	Prof. Dr. Joachim Dzubiella
3. Gutachterin:	Prof. Dr. Carol K. Hall

Tag der wissenschaftlichen Aussprache: 26.2.2016

Berlin, Deutschland.
2016

D-83

Declaration of Authorship

Ich versichere hiermit eidesstattlich, dass die vorliegende Dissertation selbständig verfasst wurde, die benutzten Hilfsmittel und Quellen korrekt aufgeführt sind und im Falle von Co-Autorenschaft die Darstellung des Eigenanteils zutreffend ist.

Acknowledgments

At this point I want to take the chance to say 'thank you' to all the people who supported me in writing this thesis, be it by scientific or personal means.
Special thanks go to Prof. Dr. Klapp for her endless efforts and all the *very* helpful advices, hints and discussions. Her commitment and support was crucial for the success of this work.
I also want to thank Prof. Dr. Hall for her hospitality during my stay in her group and her encouraging words. I always felt welcome and learned a lot. During this stay in Raleigh I spent a lot of time with Dr. Bharti, talking and discussing on science and everything else. Without him, everything would have been much more difficult. Also, I want to thank Prof. Dr. Velev for giving me the chance to relate my work to what happens in experiments.
My work was financed by the IRTG 1524, and I appreciate very much all the effort of Petra, Beatrix, Daniela and Prof. Dr. Schoen to keeping everything together. Additionally, I want to thank Prof. Dr. Schoen and Prof. Dzubiella who are willing to be part of my PhD committee.
Finally, special thanks go to the members of the AG Klapp for making daily life a nice thing and for being supportive and for helping out, when work becomes difficult.

Zusammenfassung

Diese Arbeit beschäftigt sich mit dem Einfluss induzierter dipolarer Wechselwirkungen auf die nichtgleichgewichts Strukturbildung in quasi zweidimensionalen kolloidalen Systemen. Einerseits werden konkrete experimentell realisierte Systeme theoretisch modelliert und mit Hilfe von Computersimulationen der Brownschen Dynamik untersucht. Zur Abschätzung von Phasenübergängen werden weiterhin Methoden der Dichtefunktionaltheorie angewandt. Andererseits werden generische Modelle entwickelt um grundlegende Mechanismen der Strukturbildung zu indentifizieren. Die zugrundeliegenden experimentellen Systeme entsprechen dabei zwei prototypischen nichgleichgewichts Prozessen: einmal der Bahnenbildung (lane formation) und einmal der diffusionsbeschränkten Aggregation (diffusion limited aggregation).

Im Falle der Bahnenbildung werden Janustpartikel in einem elektrischen Wechselfeld betrachtet, die, je nach Feldfrequenz, entweder kettenartige Strukturen oder einen Schwimmmechanismus ausbilden. Die theoretische Untersuchung einer explizit dipolaren Modellierung zeigt sowohl die Kettenbildung als auch neuartige Bahnenbildung im Schwimmerregime. Zusätzlich wird ein abstrakteres Referenzsystem behandelt, welches es erstmalig erlaubt eine Verbindung zwischen spinodialer Entmischung und Bahnenbildung herzustellen. Weiterhin wird hier zum ersten mal Bahnenbildung in Systemen mit attraktiven Teilchenwechselwirkungen untersucht.

Der zweite Teil der Arbeit behandelt die feldgesteuerte Aggregation kolloidaler Teilchen im diffusionsbeschränkten Regime. Hier werden ebenfalls zwei Modellsysteme untersucht. Zunächst werden experimentell beobachtete Strukturen analysiert und mit Ergebnissen aufwendiger Computersimulationen verglichen. Zu diesem Zweck wird eine neue Methode der Strukturanalyse eingeführt und angewandt. Die Experimente wurden von Dr. Bhuvnesh Bharti an der North Carolina State University durchgeführt und von mir analysiert. Die theoretischen Betrachtungen erlauben hierbei, im Gegensatz zu den Experimenten, das Aggregationsverhalten in Abhängigkeit der Partikeldichte zu untersuchen. Ergänzend dazu wird ein zweites Modellsystem betrachtet, welches auf generische Eigenschaften der feldgesteuerten Aggregation ausgerichtet ist. Hier liegt besonderes Augenmerk auf dem Verhalten im diffusionsbeschränkten Aggregationsregime. Letzteres ist ein ausgiebig untersuchter nichtgleichgewichts Prozess, der hier um neue Facetten, also feldinduzierete dipolare Wechselwirkungen, ergänzt wird.

Abstract

This work investigates the influence of induced dipolar interactions on the non-equilibrium structure formation in quasi-two dimensional colloidal systems. On the one hand, theoretical models for certain experimentally realized systems are developed and investigated by means of Brownian Dynamics Simulations. To estimate phase transitions, basic density functional theory methods are applied. On the other hand, also generic models are developed with the aim to unveil the underlying mechanisms of structure formation and particle aggregation. The experimental systems motivating this work correspond to two prototype non-equilibrium processes, which are lane formation and diffusion limited aggregation.

In the case of lane formation it is Janus particles in AC electric fields which are considered. These particles form either chain-like aggregates or yield a self-propulsion mechanism, depending on the field frequency. The investigation of an explicitly dipolar model shows chain formation as well as lane formation in the self-propulsion regime. Additionally, a generic system is considered, which allows for the first time to make a connection between lane formation and spinodal decomposition. Furthermore, this is the first study on lane formation in systems with attractive particle interactions.

The second part of this work investigates the field directed assembly of colloidal particles in the diffusion limited aggregation regime. Again, two model systems are developed and investigated. First, experimentally observed structures are analyzed and compared to results from extensive computer simulations. To this end, a new method for structure analysis is introduced and applied. Experiments were performed by Dr. B. Bharti at North Carolina State University and analyzed by myself. The theoretical considerations allow, in contrast to experiments, to investigate the dependency of the aggregation behavior on the particle density. Additionally, a second model system, aiming on the generic features of particle aggregation is investigated. Here, special attention is paid on the diffusion limited aggregation. The latter is an extensively studied non-equilibrium process, which is extended by new features, namely the influence of field induced dipolar interactions.

Publications

Most of this work is based on the publications listed below. Texts are partially rewritten and some extensions are introduced. Contributions from Co-Authors presented in this work are indicated in the text.

Lane formation in a system of dipolar microswimmers Florian Kogler and Sabine H. L. Klapp, *Europhys. Lett.* **110**, 10004, (2015).

Using Brownian Dynamics (BD) simulations we investigate the non-equilibrium structure formation of a two-dimensional (2D) binary system of dipolar colloids propelling in opposite directions. Despite of a pronounced tendency for chain formation, the system displays a transition towards a laned state reminiscent of lane formation in systems with isotropic repulsive interactions. However, the anisotropic dipolar interactions induce novel features: First, the lanes have themselves a complex internal structure characterized by chains or clusters. Second, laning occurs only in a window of interaction strengths. We interprete our findings by a phase separation process and simple force balance arguments.

Generic model for tunable colloidal aggregation in multidirectional fields Florian Kogler, Orlin D. Velev, Carol K. Hall and Sabine H. L. Klapp, *Soft Matter*, **11**, 7356 - 7366, (2015)

Based on Brownian Dynamics computer simulations in two dimensions we investigate aggregation scenarios of colloidal particles with directional interactions induced by multiple external fields. To this end we propose a model which allows continuous change in the particle interactions from point-dipole-like to patchy-like (with four patches). We show that, as a result of this change, the non-equilibrium aggregation occurring at low densities and temperatures transforms from conventional diffusion-limited cluster aggregation (DLCA) to slippery DLCA involving rotating bonds; this is accompanied by a pronounced change of the underlying lattice structure of the aggregates from square-like to hexagonal ordering. Increasing the temperature we find a transformation to a fluid phase, consistent with results of a simple mean-field density functional theory.

Contents

List of Figures

1 Introduction

Controlling colloidal self-organization processes is nowadays a promising route towards the design of new functional materials and research aiming on unveiling the underlying mechanisms is a rapidly developing discipline. The scientific understanding of colloidal self-assembly processes is mostly based on statistical physics, thermodynamics and chemistry. Together, these fields of science provide great knowledge about the nature of particle interactions and fundamental theories for the equilibrium phase behavior of particle ensembles. However, the interplay between more complex particle interactions and the out-of-equilibrium collective behavior lacks a general understanding. In this introductory chapter, we review certain aspects of the present status of the scientific understanding of complex collective colloidal behavior.

1.1 Complex Colloids

Colloidal suspensions are soft matter systems, consisting of nano to micrometer sized solid particles, so called colloids, which are suspended in a carrier liquid. A single colloid in a fluid of temperature T is subject to thermal fluctuations and undergoes Brownian motion. Furthermore, the thermal energy ($\approx k_B T$ with k_B being Boltzmann's constant) also results in a threshold for the influence of interactions between colloids. It is only colloidal interactions associated with energies $\epsilon \gtrsim k_B T$ which are able to dominate over thermal fluctuations.

An important strategy in exploiting colloidal self-assembly is based on manipulating the way colloids interact and the variety of possible colloidal interactions is enormous. A simple categorization is given by their

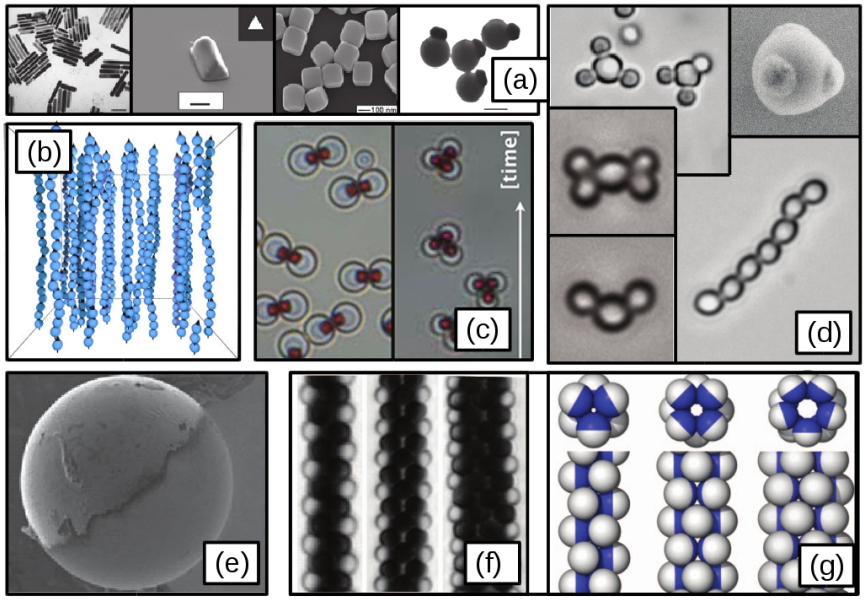

Figure 1.1: (a) Microscopic photographs of rod-, pyramid and cube-like colloids [1]. (b) Aggregation of permanent dipole particles in an external field [2]. (c) Particles with an off-centered magnetic inlay forming reversible doublet and triplet aggregates [3]. (d) Multivalent colloidal 'super-atoms' with various number of patches [4]. (e) Experimental image of a magnetic Janus-particles. Differences in the brightness of the hemispheres correspond to different surface materials [5]. (f) and (g) tube-like aggregates of magnetic Janus-particles in precessing fields field conditions [6].

origins. There exist forces exerted on the colloids by the solvent, e.g., depletion forces, by pair interactions between the colloids, e.g., electrostatic interactions, and by external fields e.g., gravitation or electromagnetic fields. An important example is the van der Waals interaction, which results from the instantaneous microscopic polarization of colloids. Importantly, van der Waals forces are present in every colloidal suspension and the presence of these short-ranged attractive forces can lead to particle aggregation. However, many colloidal particles are negatively charged, often by purpose, and repel each other due to electrostatic interactions. This counter acts the attraction due to the van der Waals interaction and can prevent aggregation. Thus, the stability of the homogeneous phase is governed by the interplay between attractive and repulsive forces. Control over this interplay can be achieved by screening the electrostatic interactions via the concentration of electrolytes in the liquid [7].

Anisotropic interactions

Of special interest however are particles with anisotropic interactions as they allow an even richer phase behavior [8]. These anisotropies can be introduced in different ways. One major example is changing particle shapes towards elongated, rod-like objects. At high packing fractions, ensembles of such particles are named liquid crystals and form the basis for many daily life technologies [9]. But also other shapes like stars [10], pyramids or cubes have gathered attention [11, 1, 12]. Microscopic images of such colloids are shown in Fig. 1.1(a).

Interaction anisotropies can also be achieved by functionalizing discrete parts of the particle surface. An important approach is here to build Janus-particles [13, 14], where a certain part of the particle surface is coated by a material different from the particle body. Partially metal-coated polystyrene spheres are one example [15] but also carbon-coated [16] or amphiphilic [17, 18] and hydrophobic [19] Janus-particles have been studied. In Fig. 1.1(e) a microscopic image of a cobalt coated magnetic Janus-particle is shown [5]. Also functionalizing the particle surface via polymers, i. e. via DNA, allows to introduce selective particle interactions [20, 21, 8].

Such efforts also follow the idea to mimic the valency of atoms by colloids [4]. In Fig. 1.1(d) we show microscopic images of complex colloids with DNA functionalized patches, which results in different interaction valencies. Additionally, images of 'colloidal molecules' assembled from these particles are shown. Such systems are still accessible by microscopes and easy to handle at room temperature but may be able to undergo aggregation in analogy to atoms.

Dipolar interactions

Directional or anisotropic interactions can also be realized by introducing magnetic and/or electric dipole and/or multipole moments which allow selective particle bonding [22, 11, 5, 23, 24, 13]. In Fig. 1.1(b), a computer simulation result showing chain formation in a system of permanent magnetic particles is presented [2]. Here, fine particle chains are oriented along an external magnetic field, which is an example for the general property of dipolar particles to orient along fields and to form chains [22]. Additionally, colloids with a dislocated permanent magnetic interaction site are shown in the microscopic image Fig. 1.1(c). These particles are able to form reversibly self-assembled non-linear aggregates, which additionally can be tuned by external fields [3].

Such complex dipole particles allow a variety of self-assembled structures [11], from field directed networks [25, 26], staggered chains and pseudo-crystalline states [15] to compact clusters with strange magnetization properties [5, 27], or magnetic tubes [6] as shown in Fig. 1.1 (f) and (g) for magnetic Janus particles in experiment and simulation, respectively.

Within this class, particles with field-induced dipolar interactions [10, 24, 28, 25, 15, 26] are especially interesting because switching the fields on and off can be equivalent to switching the particle interactions on and off. This means that aggregation mechanisms [29, 30] can be 'dialed in'. Furthermore, the orientation of inductive fields may be used to direct particle aggregation [31, 25, 28, 15, 26, 32, 33]. Exemplary, we show in Fig. 1.3 microscopic images of metallo dielectric Janus particles (a). Under the presence of an external electric field pointing vertically here the particles are (b) aggregated into staggered chains at low density [15] and (c) form percolated networks at higher density [26].

In general, recent experimental progress in the synthesis and directional binding of nanometer to micrometer sized patchy and anisotropic particles makes possible the assembly of colloidal structures with multiple directed bonds [14, 13, 4, 34]. In consequence, such directed self-assembly processes may be exploited for the formation of new functional materials with specific and/or adjustable properties. Hence, understanding the interplay between externally induced particle properties, external fields and thermodynamic conditions, e.g., temperature, is of fundamental interest in modern material science, but also from a statistical physics point of view.

1.2 Active Matter

In recent years the design of active self-propelling colloidal particles has attracted a lot of attention [35]. Literature partially uses the terms 'self-propelling' and 'active' as synonyms [36]. However, self-propelling particles are a subcategory of active particles. Generally speaking, active particles transform and dissipate energy to pertain *some sort of* (complex) non-equilibrium behavior, while self-propelling particles generate translational motion. The energy fueling the self-propulsion can be harvested from the environment or stored inside the particle. An example for harvesting active systems is protein machines [37, 38], which consume adenosine triphosphate (ATP) from the solvent and catalyze a chemical reaction. The energy associated with this reaction can then be used to perform controlled motion.
Of special interest here are self-propelling colloids which perform a run and tumbling motion [39], where the direction of motion is subject to (rotational) diffusion. This in contrast to the case of other motile non-equilibrium systems [40] e.g., field driven particles [29, 41], particles with enhanced diffusion in external fields [2, 42] or colloids under shear [43]. Here it is not the colloids which consume energy and transform it into motion by some internal mechanism; rather the colloids are passive subjects to external conditions.

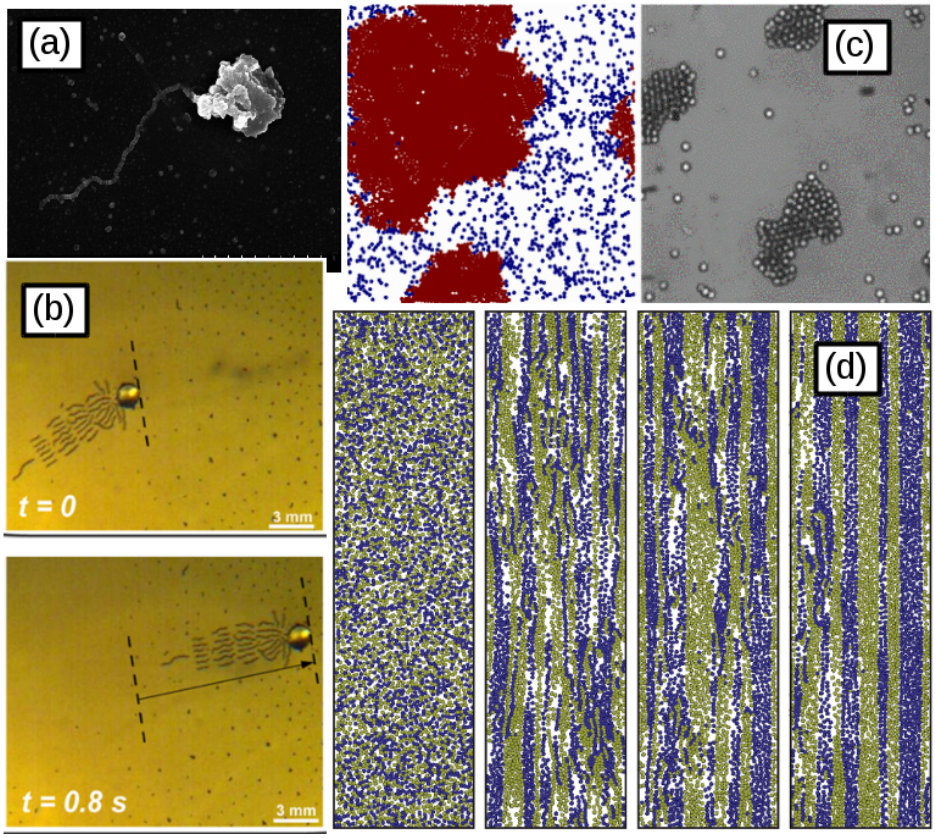

Figure 1.2: (a) Magnetically self-assembled single flagella swimmer [44]. (b) Complex 'snake-swimmer' composed of magnetic chains attached to a gold bead [45]. Both swimmers (a) and (b) require an external actuation of the flagella-like parts via alternating magnetic fields. (c) Phase separation into a clustered and a dilute phase in a system of self-propelling repulsive spheres in two-dimensions. Left computer simulation, right microscopic image from experiment [16]. (d) Simulated transition towards a laned state in two-dimensions [46]. Darker particles move downwards with increasing velocity from left to right.

1.2.1 Colloidal self-propulsion

Several colloidal self-propulsion mechanisms have been proposed and investigated in experiment [47]. Some of the presented micro swimming devices are larger aggregates of i.e., magnetic colloids (see Fig. 1.2(a) and (b)), which propel by means of a periodical mechanical deformation of flagella like sub structures [48, 44, 45]. The mechanical deformation is fueled by external fields and requires explicit control by humans. Also active liquid crystals have gather attention [49, 50].

Other swimmers are essentially Janus particles, where a certain part

of the colloid surface is influencing the solvent and generating some sort of gradient. This can be done by an asymmetric chemical reaction [51, 16, 47] of e.g., a metal coated surface part, which locally catalyzes the decomposition of a dissolved fuel. This chemical reaction and the energy associated with it pertains a chemical gradient at the particle surface and fuels the propulsion.

Also light induced chemical reactions [52] or localized heating (self-thermophoresis) [53, 16] of the coated hemisphere have been used to propel Janus-particles; In the latter setup, the temperature gradient induces complex asymmetric solvent flows around the particle which effectively exert a force on one of its hemispheres. Another microswimming Janus particle, which will be investigated in detail in Chapter 4, is fueled by an uni-axial electric field inducing dipole moments of different strength in its two hemispheres [15]. Again, this results in complex solvent flows effectively propelling the particle [54]. In the investigated two-dimensional set up, the external field orientates these particles, thereby restricting the propulsion to the directions perpendicular to the field vector [55].
Importantly, many of these experimental studies are concerned with the propulsion mechanism of a single particle rather than with the collective behavior of large numbers of these particles.

1.2.2 Collective behavior of active colloids

From a theoretical point of view, the collective behavior of active colloids has been studied extensively [56, 57, 35, 58]. Basic model systems of active particles [59, 57, 60, 61] have gathered a lot of attention. The famous Vicsek-model [59] and its derivatives [62], where the particles have a mechanism which tries to align their propulsion directions, lead to the idea of a motility induced non-equilibrium pseudo-phase transition [63] as an analogue to the ferromagnetic transition in the Ising model. Also motility induced crystallization phenomena [64, 65, 66], swarm formation [60], turbulence and vortex arrays [67] have been reported. Very recently, experimental and theoretical evidence of motility induced phase separation processes in systems of self-propelled rods, so called active nematics [49], and discs without an alignment mechanism [68, 16, 69, 70, 71, 72] and even without attractive forces has been found [73, 58]. Importantly, such phase separation is unknown in equilibrium systems of hard discs. In Fig. 1.2(c) experimental and simulated phase separated states of solely repulsive spheres in an quasi two-dimensional setup are shown [16].

Approaches to describe such phenomena often try to map the non-equilibrium behavior onto the equilibrium behavior of an effective reference system. This is done by incorporating the self-propulsion mechanism into effective potentials [69, 74] or by extensions of thermodynamic theories i.e., an effective Cahn-Hillard equation [75] or non-equilibrium equa-

tions of states [76]. Still, a well founded theory for the (pseudo) phase behavior of active particles has not been established by now [77] and the effective thermodynamic descriptions and/or mappings onto passive pair potentials have been challenged recently [78]. For particles with more complicated interactions i.e., dipole-dipole interactions [79], theoretical studies are rare. The above mentioned dipolar Janus swimmers [55] are therefore of special interest; as they are able to change their direction of motion, although only perpendicular to the external field, they can be seen as self-propelling particles with complex anisotropic dipolar interactions. In principle, they form a binary mixture of dipolar self-propelling particles, whereas particles of different species are moving in opposite directions. This general set up has previously been investigated for repulsive spheres and shows another motility induced non-equilibrium phase transition known as laning [80].

1.2.3 Lane formation

Lane formation is a prototype of a non-equilibrium self-organization process, where an originally homogenous mixture of particles (or other types of "agents") moving in opposite directions segregates into macroscopic lanes composed of different species. This ubiquitous phenomenon occurs, e.g., in driven binary mixtures of colloidal particles [81, 82, 80], migrating macro-ions [83] or in binary plasmas [84, 85, 86]. The latter have been investigated under microgravity conditions on board of the International Space Station [87, 88]. In addition, also self-propelling systems with aligned velocities such as bacteria in channels [89] and humans in pedestrian zones [66] or swarms of ants [90] undergo lane-formation. In Fig. 1.2 (d) the transition towards a laned state in large scale computer simulations of soft discs driven in opposite directions is shown. With increasing propulsion velocities, from left to right, lane formation becomes more and more pronounced.

In particular, studies of charged colloids have revealed many fundamental aspects of laning such as the impact of density [91], the occurrence of a freezing process [65], the role of hydrodynamics [92], the accompanying microscopic dynamics (particularly, the so-called dynamical locking) [82], and the impact of anisotropic friction [93].

All of these models involve *isotropic* and *repulsive* interactions between the colloidal particles. Then, the laning transition in two-dimensions is a smooth crossover and subject to finite-size effects [46].

Also lattice models have been investigated from a solely theoretical point of view [94]. Furthermore, the laning transition seems to bear some similarities to equilibrium decomposition processes in binary mixtures of (attractive) colloidal particles. In Chapter 3, results establishing a connection between lane formation of dipolar Janus swimmers and equilibrium phase separation processes are discussed.

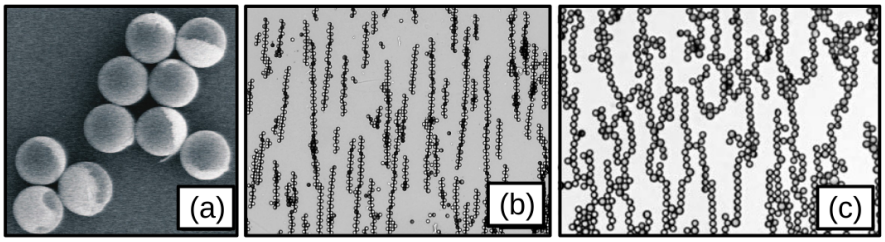

Figure 1.3: Experimental image of (a) metallo-dielectric Janus-particles. Differences in the brightness of the hemispheres correspond to different surface materials. (b) Microscopic photograph of staggered chains and (c) percolated networks. Images taken from [26].

In general, recent progress in colloidal chemistry has generated a variety of complex, anisotropic particles (see, e.g., [14, 13, 3]), which can perform *controlled* translational motion in an external field [55, 26], like simple charged colloids, but display complex self-assembly behavior already in equilibrium [26, 95]. In driven ensembles of such particles one may therefore expect a wealth of new phenomena induced by the interplay between self-assembly due to pair-interactions, on the one hand, and dynamical self-organization processes such as laning, on the other hand. The consequences are so far only poorly understood, contrary to the widely studied case of active (self-propelled) particles [40, 16, 70] with more simple isotropic interactions. Hence, dipolar microswimmers are important model systems for the interplay between laning and non-trivial self-assembly.

1.2.4 Self-propelling metallo-dielectric Janus particles

The experimental dipolar Janus swimmers considered here consist of a polystyrene sphere with radius $\approx 5\mu m$ and one hemisphere partially covered by a gold patch (see Fig. 1.3(a)). Dispersed in weakly ionized water and confined between two glass plates a quasi two-dimensional geometry is realized. Application of an in plane AC-electric field $\mathbf{E}_{ext}$ induces effectively multipolar moments in the metallo-dielectric colloids and aligns the plane between their hemispheres along the external field, which has been observed in experiment and shown theoretically by electrostatic calculations of a single particle in an electric field [15, 55]. Interestingly, under reasonable experimental field conditions, the energy difference between an field aligned orientation and an orientation rotated by 90°around the out-of-plane axis (perpendicular to $\mathbf{E}_{ext}$) is in the order of $\approx 100 k_B T$ [15]. This large energy difference effectively suppresses any rotations of the particles around the out-of-plane axis. In a truly two-dimensional setup this means that particles have a fixed orientation, with the gold patched part

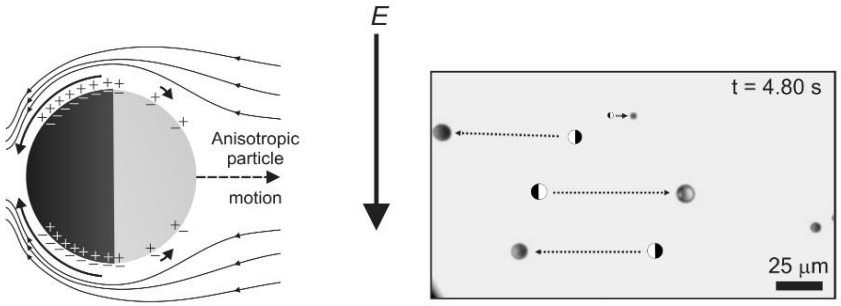

Figure 1.4: Self-propulsion of Metallo-dielectric Janus-particles: (Left) Sketch of a single particle and the distribution of charges on its surface. The solvent flows generated by these distributions and indicated by arrows result in a propulsion force perpendicular to the external field E. (Right) Photograph from experiment visualizing how particles with opposite orientation of the gold-patched hemisphere move under presence of the external electric AC-field E. Images taken from [55].

pointing either to the left or to the right, as depicted on the left side of Fig. 1.4. Depending on the frequency f and strength E_{ext} of the external field different structures and particle behaviors can be observed. At high frequencies ($f > 10kHz$) and low field strengths particles form staggered chains (see Fig. 1.3(b)). Also colloidal network formation has been reported for the high frequency regime in experiment [26] and theory [95] (see Fig. 1.3(c)). Here, particles arrange into chains along and perpendicular to the electric field. Most important to us, increasing the field strength and keeping $f < 50kHz$ leads to the appearance of a phenomenon called induced-charge electro-phoresis (ICEP) [55]. There particles become self-propelled by converting field transmitted energy into kinetic energy. An explanation for this mechanism is given in [54, 55] and assumes that $\mathbf{E}_{ext}$ induces electric dipole moments in the particles and polarizes the electrical double layer around them (see Fig. 1.4). The polarized charge distribution in the electrical double layer becomes inverted in each half cycle of the alternating external field and forms, for a homogeneous particle, a quadrupolar flow pattern [96]. This pattern pertains an inflow of fluid along the field orientation and an outflow perpendicular to the field. However, here it is Janus-particles which are considered, and as the induced charge in the gold covered hemisphere is stronger (due to the higher polarizability of the gold patch), a larger amount of fluid is flowing around the metallic hemisphere. Therefore a larger net ejection of fluid is present at the metallic side of the particle and in consequence, a net force is acting on the gold covered hemisphere. These complex solvent flows effectively generate a propulsion force orthogonal to the external field in the direction of the dielectric hemisphere. The theoretical derivation of the

velocity of such a dielectric Janus particle undergoing ICEP results in a velocity [55, 54]

$$v = \frac{9}{64} \frac{\epsilon \sigma E_{ext}^2}{\eta(1-\delta)} \tag{1.1}$$

whereas the parameter δ relates to the capacitance of the double layer, E_{ext} is the amplitude of the external field, σ is the particle diameter, and ϵ and η are the permittivity and the viscosity of the bulk fluid, respectively. Compared to other self-propelling particles these are high velocity particles moving with up to $30\mu m/s$ quadratically depending on the external field strength and linear on the particle size, as determined from experiments and in semi-quantitatively agreement with theory [55]. Interestingly, we can see that the dipolar coupling energy is proportional to E_{ext}^2 and thus also v.

Finally, these particles can be seen as active microswimmers because they transfer externally supplied energy into kinetic energy while being able to change their direction of motion by rotations around the field orientation $\mathbf{E}_{ext}$.

1.3 Non-Equilibrium Aggregation of Colloids

Besides the equilibrium aggregation of complex colloids and the collective behavior in active systems, also the non-equilibrium *aggregation* of colloidal particles is of major interest. In contrast to active systems, particles do not consume energy to pertain their motility, but rather undergo aggregation processes which prevent relaxation into the equilibrium state [97]. Several non-equilibrium situations are possible, for example uni-directional field controlled assembly [26, 95, 40, 98] or particle deposition of colloids [99] and/or macromolecules [100] on surfaces. Interestingly, permanent magnetic particles in rotating magnetic fields [6, 41] bear some similarities to active systems, as here the particles are able to synchronize their rotational motions to each other without following the rotation of the field directly. This synchronization then leads to aggregation of complex structures like layers [41] or tubes in case of Janus particles [6].

1.3.1 Disordered solids - glasses and gels

Of special importance to the understanding of non-equilibrium aggregates are disordered solids like glasses and gels. Glasses are high density arrested states, where an effect called caging traps the particles in, from equilibrium statistical physics point of view, unfavorable disordered configurations [97]. The arrested state is a result from a 'historical' process (quench), where a liquid is cooled fast enough to avoid crystallization and particles get stuck in liquid-like arrangements. The caging is reflected by tremendously slow relaxational dynamics. For example, the

time a particle needs to travel a distance equal to its diameter can be increased up to 15 orders of magnitude by only slightly decreasing temperature [97]. Glasses are realizable in systems of solely repulsively interacting discs. However, there exists also a re-entrance effect of the glass phase by increasing temperature [97] if short-ranged attractive interactions are present.

Another important subset of the many classes of self-assembled non-equilibrium structures are gels. Although there is an ongoing debate on how to define a gel properly [101], it is generally assumed that the formation of a gel requires some sort of attractive particle interactions. Here, the term gel is used for colloidal systems in a disordered state at *low* volume fractions, with very slow relaxational dynamics. Additionally, stable percolated colloidal networks are generally considered to be the underlying micro-structures of gels. Such system-spanning cross-linked particle clusters may already result from simple isotropic attractive interactions, like the well known Lennard-Jones interaction. However, many patchy particle models strongly favor chaining and branching [102, 103, 104, 105] of aggregates and therefore structures which are occupying larger parts of the accessible space. This increases the systems capability to form cross-linked particle networks already at low volume fractions and hence gelation. Importantly, in the basic model for a two-dimensional ferrofluid [22] (dipole-dipole interaction due to centered point dipole moments in hard-discs), particles favor chain and ring-like structures rather than branching. In consequence, it is unclear whether such ferrofluids undergo gelation [106, 107, 108, 109]. Nevertheless, more complex dipolar models [26, 95, 105, 108] form gels. Interestingly, many generic models for patchy particles have been proposed [110, 8, 105, 103, 111]. Such approaches often aim on a conceptional understanding of network formation and gelation of patchy particles and allow a theoretical understanding of the competition between condensation and chaining/branching e.g., via Wertheim theory [105, 101]. In fact, the formation of a (non-equilibrium) gel[1] is intimately related to the equilibrium phase behavior of the system and often seen as an arrested phase separation process created by a quench into the coexistence region. Instead of undergoing the full liquid-gas phase separation or a spinodal decomposition, initially formed (chain-like) condensates undergo a freezing process [112]. This is because interactions become much stronger than $k_B T$, preventing particles from dissociating due to thermal fluctuations. In Fig. 1.5 (b) and (c) experimental images of polyethylene (PMMA) polymer mixtures in a state of arrested phase separation are shown [112]. On the right (Fig. 1.5 (c)), discrete frozen clusters are not able to percolate, while on the left (Fig. 1.5 (b)) a single percolated cluster exists at slightly higher volume fraction and forms a gel. Still, single PMMA-particles are present, corresponding to the par-

[1] This holds only for non-equilibrium gels. For a discussion of 'equilibrium routes' towards gelation see [101].

ticle poor phase. The phase separation process is arrested and therefore irreversible. It leads to a pronounced hindrance of structural reconfiguration and, given the volume fraction of colloids is not too small, percolation becomes possible but is mediated by clusters rather than by single particles [101, 113]. Finally, such gels undergo aging processes and the micro-structures may collapse over long times [101, 114, 115].

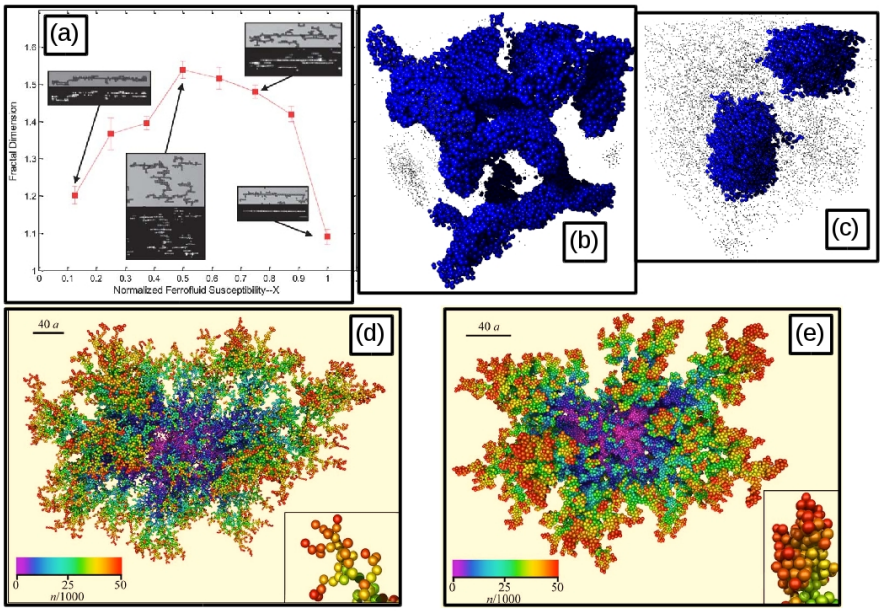

Figure 1.5: (a) Tunable field directed assembly of chain-like and network-like fractal aggregates in binary mixtures of magnetic colloids and the corresponding fractal Dimension D_f as function of an effective field-strength. [98] (b) Percolated cluster of a chemical gel at slightly higher volume fraction than (c) where discrete frozen clusters are not able to percolate [112]. Fractal Particle aggregates from computer simulations of (d) classical DLA and (e) slippery DLA [116].

1.3.2 Diffusion limited aggregation

An ideal route towards gelation is described by the concept of diffusion limited cluster aggregation (DLCA), where each particle or cluster collision leads to the formation of a rigid and essentially (on the timescale of the experiment) unbreakable bond with fixed spatial orientation. Classically, single particles undergoing Brownian motion (DLCA) are considered but also the aggregation of ballistically moving particles [117, 118] has gathered attention. Systems with DLCA undergo irreversible dynamics and form fractal aggregates with specific fractal dimension $D_f \approx 1.71$

in continuous two-dimensional space [119, 120]. Such colloidal systems are considered to be 'chemical gels', while at higher temperatures these systems become 'physical gels' where single particles and larger substructures start to connect and disconnect frequently. This strongly affects (increases) the fractal dimension [121, 122] and finally allows the system to achieve its equilibrium state. Interestingly, it turned out that the aging properties of a chemical gel, an ongoing compactifaction with time, can be mapped onto the temperature dependence of the compactness of a physical gel, at least for low valency patchy particles [121].

A recently introduced new type of DLCA, which accounts for local rearrangements via flexible bonds, is slippery diffusion limited cluster aggregation (sDLCA) [123, 116]. Slippery bonds allow particles to move or rotate around each other as long as they stay in contact, meaning that bonds are still unbreakable but can change their orientation. This additional degree of freedom generates, at least in three-dimensional simulations [123, 116], aggregates of the same fractal dimension as classical DLCA but with a larger coordination number. The latter means, that the local structure of aggregates is more compact while the global structure on large length scales remains in principle the same. In Fig. 1.5 (d) and (e), simulated slippery and classical DLA fractals are shown, together with images of their local structure in the insets.

DLCA processes have been studied extensively in systems with isotropically attractive particles [124, 119] but also in systems with patchy particles bearing permanent and/or locally restricted interaction sites on their surfaces [121, 125, 126, 127, 128, 129]. In the latter, the spatial orientations of interaction sites can either be free to rotate [127, 121, 129] or fixed in space [130, 131, 98, 95]. When the orientations of interaction sites are fixed in space, the associated 'chemical gels' undergo *anisotropic* diffusion limited aggregation which yields a fractal dimension of $D_f \approx 1.5$ [132, 130, 131, 98, 129], lower than for the isotropic case. This situation occurs, e.g., in lattice models [132, 130, 131], where motion is naturally restricted to certain directions. However, there is also the possibility to direct the DLA process by e.g., external fields [98, 33]. In Fig. 1.5 (a), microscopic images of fractal structures stemming from a field directed diffusion limited aggregation process are shown. In this system it is a mixture of para and diamagnetic colloids immersed in a ferrofluid and exposed to an uniform external magnetic field. The red curve gives the dependency of the fractal dimension on an effective field strength, which is controlled by the concentration of the ferrofluid. Here, the shape of the two-dimensional aggregates can be tuned, but only in one direction. A similar situation is given for the networks formed by the metallo-dielectric Janus-Particles presented in Fig. 1.3(c), where chaining along the field is tunable by the field strength, while chain formation and percolation perpendicular to the field is determined by the same field strength. Starting from these systems it is of great interest to design and investigate a system

allowing individual control over the chaining properties in several directions. In the following we will present an experimental setup allowing field controlled bi-directional chain and network formation.

1.3.3 Aggregated networks of superparamagnetic colloids

An experimental quasi two-dimensional system of suspended colloidal particles, each composed of super-paramagnetic iron-oxide aggregates embedded in a polymer matrix, was designed to undergo field directed colloidal aggregation and has been investigated experimentally by Dr. B. Bharti [25, 133] at North Carolina State University in the Group of Prof. Dr. O. D. Velev.

The experimental setup is shown in Fig. 1.6(d) and consists of two gold electrodes for the application of an AC-electric field (E) and a pair of electromagnets capable of generating an uniform magnetic field (H). The relative angle between the external electric and magnetic fields is kept at constant 90° such that the electric field is orthogonal to the magnetic field ($E \perp H$) and both lay in the assembly plane. The change in the spatial distribution of the particles upon the application of fields was monitored perpendicular to the assembly plane by a bright field microscope (Olympus BX-61). The directional assembly of colloids in external electric and magnetic field was performed using an aqueous dispersion of electromagnetoresponsive microparticles. The microspheres (COMPEL TM , Bangs Labs Ltd.) were composed of superparamagnetic nanoparticles embedded in a matrix of polystyrene with diameter $\sigma = 5.7 \pm 0.2 \mu m$. The particles were strongly negatively charged (pH < 2) because of surface functionalization with -COO - groups and hence stable in their aqueous dispersion. The superparamagnetic microparticle dispersion was transferred to the assembly chamber on the experimental set-up and different field configurations were applied.

The external field driven assembly of colloids is then governed by the field-induced dipolar interactions between the particles. Here, two non-interacting independent electric and magnetic dipoles are induced in each particle. This configuration of the particles can be termed as double-dipolar state, where each dipole selectively interacts with the dipoles of same kind belonging to different particles (electric with electric and magnetic with magnetic). The crossed external electric and magnetic fields, oriented in plane but perpendicular to each other, enforce a directed self-assembly process of two-dimensional single-particle chain networks along the field directions. Experimental photographs of the resulting network structures are shown in Fig. 1.6 (b) and (e). Additionally, chain like aggregates when only the electric (Fig. 1.6(a)) or magnetic (Fig. 1.6(c)) field is present are shown. Interestingly, chain formation due to the presence of only the magnetic field is different to the case when only an electric field is

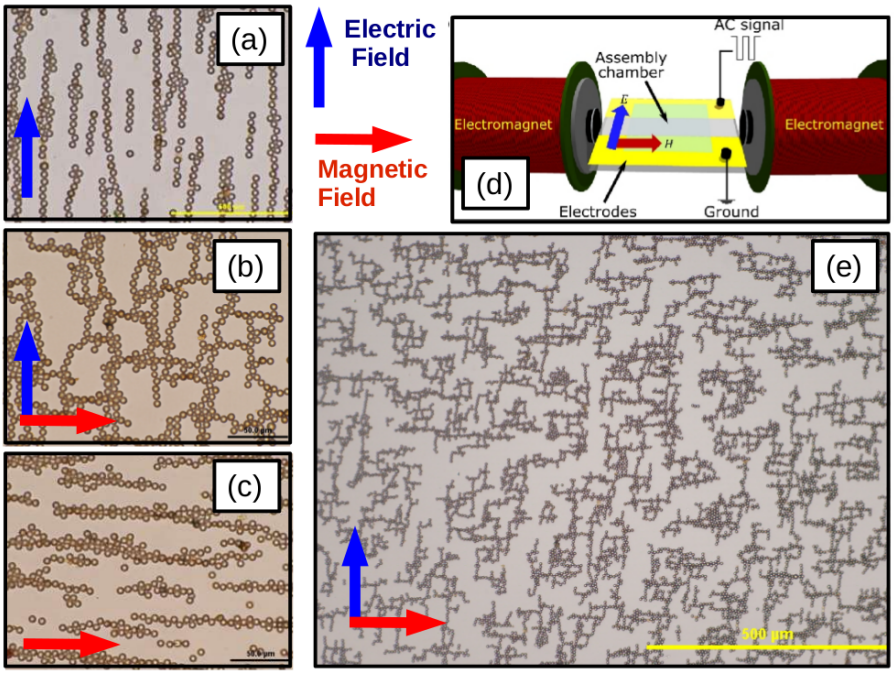

Figure 1.6: Field directed aggregation of superparamagnetic polymer particles under the presence of (a)/(c) electric/magnetic, (b) and (e) crossed electric (vertical direction) and magnetic fields (horizontal direction). Then, particles form rectangular network-like structures. (d) Sketch of the experimental setup used for assembling superparamagnetic microspheres by orthogonal AC-electric and constant magnetic field.

present. In general, magnetically assembled chains are more compact and partially staggered. This phenomenon will be discussed in more detail in Sec. 3.4 and Sec. 5.1.3.

1.4 Outline of this Thesis

The overall goal of this work is to enhance the understanding of how directional interactions in general, and induced dipolar interactions in particular, effect prototype non-equilibrium self-organization processes. In detail, the interplay between complex self-assembly due to anisotropic pair interactions and lane formation as well as diffusion limited aggregation is investigated. In both cases, extensive Brownian dynamics simulation studies are performed to understand the self-assembly processes. Using models of different complexity we are able to establish quantitative connections to experimental results as well as conceptional explanations of the observed assembly processes. Besides that, simple tools from density functional theory are applied to estimate the onset of spinodal decom-

position. This is of special interest as the non-equilibrium pseudo-phase behavior turns out to be tightly related to the equilibrium phase behavior of the systems.

The rest of this work is organized as follows.

First, basic concepts of the theory of simple fluids are briefly introduced in Chapter 2. In Chapter 3 we develop several different models to describe and investigate particular colloidal systems in experiment. We start with the dipolar microswimmers presented in Sec. 1.2.4 and introduce the double dipolar particle model (DDP-model), which is a complex model with anisotropic (dipole-dipole) interactions. Additionally, we introduce a model of reduced complexity for which the equilibrium phase behavior is well known. Then we turn towards models for superparamagnetic particles in crossed fields as described in in Sec. 1.3.3. Again, we first present a complex model treating the anisotropic dipole-dipole interactions in detail and then turn towards a complexity reduced generic model, which allows to tune the anisotropy in pair interactions. Additionally we introduce a new technique which allows structural analysis of colloidal network structures on a particle resolved level. In Chapter 4, lane formation of dipolar microswimmers is investigated. Special attention is given to the connection between lane formation under the presence of dipolar interactions and phase separation in the equilibrium system. Chapter 5 investigates the diffusion limited aggregation of superparamagnetic colloids in crossed magnetic and electric fields. The main question here is how the induced anisotropies change the structural properties of the networks. Besides, a close connection of the simulated data with experimental data is presented which allows to map out a state diagram for different field conditions. Finally, Chapter 6 is giving a summary and an outlook and in the appendix methodological details on the computer simulations are presented.

2

Theoretical Concepts and Methods

In this chapter we first start with a microscopic/particle based description of colloids dispersed in a liquid. This description results in a system of coupled differential equations, the so called Langevin equations. Due to the complexity of the considered many-particle systems, our investigations are based on computer simulations, which are a powerful tool to study colloidal systems on a single particle resolved level. To this end we introduce the methodology of so called Brownian Dynamics (BD) Computer simulations in the appendix.

A second approach towards a description of colloidal ensembles is given by Density Functional Theory (DFT). This method yields a way to find the equilibrium density distribution of a colloidal system, which allows analysis of its equilibrium phase behavior. In detail, we introduce some basic concepts and methods from DFT, which are necessary to understand the occurrence of phase transitions and phase coexistence. This chapter ends with an approximated expression for the isothermal compressibility, which later serves as a tool to estimate the occurrence of phase instability.

2.1 Langevin Equation

A material of micron-sized particles dispersed in a liquid is usually called a colloidal suspension. Each of the colloidal particles is subject to several forces which are imposed on it by the solvent and by other colloids. The forces emerging from the solvent are two-fold and result in dissipation due to frictional forces and in diffusion due to thermal fluctuations.

First, solvent molecules hitting a colloid transfer momentum on it. This happens according to their mean kinetic energy $d \times 1/2 k_B T$, where k_B is Boltzmann's constant, d the spatial dimension of the system and T its temperature. Usually it is not necessary to resolve the momentum transfer from each solvent particle onto each colloid explicitly. A statistical description turns out to be sufficient. The widely used approach is to describe the momentum transfer onto the colloid i by an *effective* random force $\mathbf{F}_i^D$ and an *effective* torque $\mathbf{T}_i^D$, which can be seen as vector sums over all forces and torques resulting from single hitting events. Secondly, the solvent leads to a frictional force $\mathbf{F}_i^F$ and a frictional torque $\mathbf{T}_i^F$ opposing translation and rotation of the colloid, respectively. Finally, the colloids also interact with each other according to some forces $\mathbf{F}_i$ and torques $\mathbf{T}_i$ stemming from pair interactions, e.g., magnetic interactions. Note that these forces can also incorporate external influences stemming from, e.g., an electric field. Adding all these forces to newton's equations of motion yields for a particle i of mass m the so called Langevin equations

$$m\ddot{\mathbf{r}}_i = \mathbf{F}_i - \gamma_T \dot{\mathbf{r}}_i + \mathbf{F}^D \tag{2.1}$$

$$I\dot{\boldsymbol{\omega}}_i = \mathbf{T}_i - \gamma_R \boldsymbol{\omega}_i + \mathbf{T}^D \tag{2.2}$$

whereas γ_T and γ_R are the translational and rotational friction coefficients, respectively. The stochastic contributions obey Gaussian distributions with mean

$$< \mathbf{F}^D(t) >= 0 \tag{2.3}$$

$$< \mathbf{T}^D(t) >= 0 \tag{2.4}$$

and with variance

$$< \mathbf{F}_i^D(t) \cdot \mathbf{F}_j^D(t') >= 2 k_B T \gamma_T \delta_{ij} \delta(t - t') \mathbb{1} \tag{2.5}$$

$$< \mathbf{T}_i^D(t) \cdot \mathbf{T}_j^D(t') >= 2 k_B T \gamma_R \delta_{ij} \delta(t - t') \mathbb{1}. \tag{2.6}$$

Usually Eqs. [2.1,2.2] are written in terms of translational and rotational *diffusion coefficients* D^T and D^R. These coefficients are defined by a *fluctuation dissipation theorem (FDT)* relating temperature and friction via

$$D^T = k_B T / \gamma_T \tag{2.7}$$

$$D^R = k_B T / \gamma_R. \tag{2.8}$$

and can easily be substituted in Eqs. [2.1,2.2,2.5,2.6]. Due to the coupling between random forces and torques to the friction coefficients in Eqs. [2.5,2.6], thermal fluctuations effectively compensate for energy losses due to dissipation in this framework. The natural timescale on which a single colloid diffuses a distance equal to its own diameter σ is then given by the so called Brownian time scale

$$\tau_b = \sigma^2/D^T. \tag{2.9}$$

2.1.1 Ovderdamped limit

The Langevin equations (Eqs. [2.1,2.2]) are second order differential equations accounting for inertial effects. In colloidal systems however, dissipation of kinetic energy due to friction is usually so strong that once a moving particle experiences no force its (translational) motion with respect to the solvent will stop on a very short time scale $\tau_m = m/\gamma_T$ [7]. Relating the time τ_m, during which momenta of particles relax, to the Brownian time τ_b allows to estimate the influence of inertia on the particle dynamics. To this end, the translational Langevin equation[1] can be rewritten

$$\frac{\tau_m}{\tau_b}\ddot{\mathbf{r}}_i = \frac{1}{\gamma_T \tau_b}\{\mathbf{F}_i - \gamma_T \dot{\mathbf{r}}_i + \mathbf{F}^D\} \tag{2.10}$$

As τ_m is proportional to the mass and hence to the particle volume $V \propto \sigma^3$ it decreases faster with smaller particle diameter than the Brownian time scale τ_b, which is proportional to the particle surface $S \propto \sigma^2$. It turns out, that for typical colloidal systems the coefficient on the left hand side of Eq. [2.10]

$$\frac{\tau_m}{\tau_b} \ll 1 \tag{2.11}$$

becomes very small[2]. This situation corresponds to the so called overdamped limit of the Langevin equation, where the inertial parts in Eqs. [2.1,2.2] become very small and can be neglected. Please note, that in this limit ($O([\frac{\tau_m}{\tau_b}]^0)$) the equations of motion are not able to describe the particle behavior on time scales smaller than the time τ_m. The *overdamped* equations then read

$$\gamma_T \dot{\mathbf{r}}_i = \mathbf{F}_i + \mathbf{F}^D \tag{2.12}$$

$$\gamma_R \boldsymbol{\omega}_i = \mathbf{T}_i + \mathbf{T}^D, \tag{2.13}$$

whereas γ_T and γ_R are again the translational and rotational friction coefficients and the stochastic contributions obey again Gaussian distributions according to Eqs. [2.3,2.4,2.5,2.6].

[1] For simplicity, this consideration is restricted to the translational part. A analogous argument holds however for the rotational dynamics.

[2] For example, for a SiO particle with $\sigma = 1\mu m$ at room temperature suspended in water is found $\tau_m \approx 10^{-7} s$ and $\tau_b \approx 2s$ [7].

The solutions of Eqs. [2.12,2.13] are the trajectories of the colloidal particles. However, an analytical solution for a many particle system is in general not possible. An alternative is to integrate Eqs. [2.12,2.13] numerically; a procedure which is usually called Brownian dynamics (BD) computer simulation [134, 135]. Large parts of this work are based on these computer simulations. In the appendix a detailed description of these methods is presented.

2.2 Phase Transitions

A phase transition is the transformation of one thermodynamic equilibrium state of matter towards another one because of a change in the thermodynamic conditions. Thereby certain macroscopic properties of the system, such as magnetization, change. From a theoretical point of view, phase transitions are categorized by the occurrence of a discontinuity in the first derivative of the thermodynamic free energy F with respect to some thermodynamic variable. For instance, when water is heated up to its boiling point its density decreases *instantly*. Hence, the vapor-liquid transition is an example for a (discontinuous) first-order phase transition. The set of all phase points which yield such a discontinuity separates different phases and is called the phase boundary. Phase transitions without a discontinuity in any *first* derivatives of the free energy are called (continuous) higher-order transitions. Importantly, there exists a critical point (with the critical temperature T_c) defining the end of the phase boundary. Consequently, a path leading from vapor to liquid at or above the critical temperature yields a continuous change in density. Furthermore, decreasing temperature leads towards the triple point representing the intersection of the phase boundaries between solid, liquid and vapor phases. At the triple point the vapor-liquid phase boundary and the liquid-solid phase boundary merge and form a lower temperature limit for the liquid phase.

2.3 Phase Coexistence

In general, a thermodynamic system is in its equilibrium phase if the Helmholtz free energy

$$F = U - TS \tag{2.14}$$

is minimized, whereas U is the internal energy due to pair interactions and/or external fields and S is the entropy. For a mono-disperse system of Hard-Spheres, meaning that all particles and interactions between them are equal and solely repulsive, holds $U > 0$ and it is only the entropy S by which F can be minimized[3]. Hence, the system seeks to achieve a homoge-

[3]The temperature T serves only as a scaling factor here

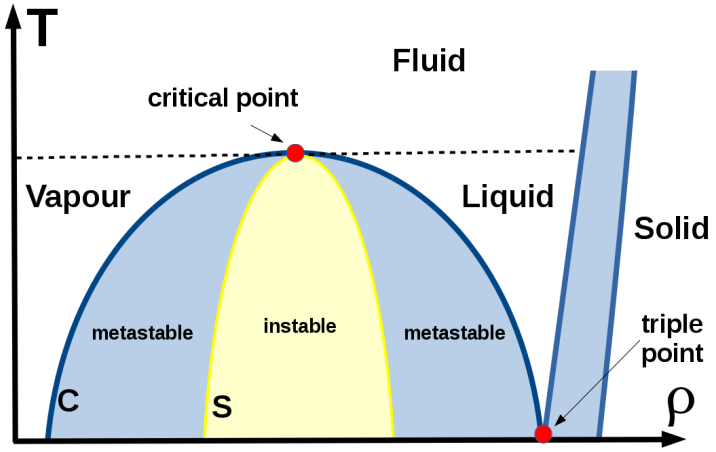

Figure 2.1: Prototype phase diagram of a simple fluid. Coexistence line C, and spinodal S indicating the occurrence of meta and instability of the homogenous phase. The critical temperature is the upper boundary of the coexistence region.

neous state, where the *mean* density is the same everywhere in the system. In addition to systems forming such homogeneous phases there exist thermodynamic systems where two phases, such as liquid *and* vapor coexist at the same time. Such a situation is the result of a phase separation process and characterized by spatial inhomogeneities, meaning that domains of different densities are present in the system. In a mono-disperse system, phase coexistence requires in any case attractive particle interactions such that the internal energy can become $U < 0$ and starts to compete with the entropy S and temperature T in minimizing F.
Interestingly, phase boundaries are the sets of phase points where the homogeneous phase is either metastable or unstable. Here, density fluctuations can cause the system to phase separate. In Fig. 2.1 a schematic temperature-density phase diagram for a one component fluid is shown. The homogeneous liquid and vapor phases are separated by the coexistence curve C enclosing the region of phase coexistence. Within the coexistence curve lies the spinodal line S, defining the region of instability; here, infinitesimal density fluctuations are sufficient to induce phase separation. Between the spinodal and the coexistence curve the system is metastable and finite fluctuations are needed to induce the phase separation process.
Finally, the simplest theoretical understanding of first-order phase transitions and phase separation processes is given by the van der Waals theory [136], which yields an equation of state for a simple fluid expressing the relation between pressure P, volume V, temperature T and particle number N. The solutions $P_T(V)$ of the van der Waals equation at fixed $T > T_c$ are monotonously decaying, while they oscillate for temperatures

$T < T_c$. These oscillations are usually called the van der Waals loops and result in positive slopes of the isotherms $P_T(V)$. Consequently, the isothermal compressibility, given by

$$\chi_T = -\frac{1}{V}(\frac{\partial V}{\partial P})_T, \tag{2.15}$$

becomes negative inside these loops. As this means that an increase in pressure results in an expansion of the fluid, this is an unphysical result and indicates the instability of the homogeneous phase. In this framework, the unstable region inside the coexistence region is characterized by $\chi_T < 0$. This provides a way to determine the spinodal line S by calculating the thermodynamic parameters at which χ_t changes its sign. In the following we will shortly present a way to determine χ_T via basic density functional theory methods. We start with an expression for the direct correlation function in the random phase approximation. Then we relate the direct correlation function to the isothermal compressibility via the Ornstein-Zernike Equation.

2.4 Pair Correlation Function

In a system of N particles, the one and two particle densities $\rho^{(1)}(\mathbf{r})$ and $\rho^{(2)}(\mathbf{r},\mathbf{r}')$ can be defined in terms of delta functions

$$\rho^{(1)}(\mathbf{r}) =< \sum_{i=1}^{N} \delta(\mathbf{r}-\mathbf{r_i}) > \tag{2.16}$$

$$\rho^{(2)}(\mathbf{r},\mathbf{r}') =< \sum_{i=1}^{N}\sum_{j=1}^{N} \delta(\mathbf{r}-\mathbf{r_i})\delta(\mathbf{r}'-\mathbf{r_j}) > \tag{2.17}$$

whereas the brackets indicate an ensemble average. These functions are normalized via

$$\int \rho^{(1)}(\mathbf{r})d\mathbf{r} =< N > \tag{2.18}$$

$$\int\int \rho^{(2)}(\mathbf{r},\mathbf{r}')d\mathbf{r}d\mathbf{r}' =< N^2 > - < N > \tag{2.19}$$

Eq. [2.18] gives in principle the mean number of particles $\bar{N}$ and (except of proper normalization) the quantities $\rho^{(n)}(\mathbf{r})d\mathbf{r}^n$ can be interpreted as the probability to find n particles in the volume element $d\mathbf{r}^n$, irrespective of all other particles. From this follows directly that the two-particle correlation function is given by

$$g^{(2)}(\mathbf{r},\mathbf{r}') = \frac{\rho^{(2)}(\mathbf{r},\mathbf{r}')}{\Pi_{i=1}^{N}\rho^{(1)}(\mathbf{r}_i)} \tag{2.20}$$

which reduces for an homogenous and isotropic fluid to the radial distribution function

$$g^{(2)}(r) =< \frac{1}{\rho N} \sum_{i=1}^{N} \sum_{j=1}^{N} \delta(\mathbf{r} + \mathbf{r_i} - \mathbf{r_j}) >, \tag{2.21}$$

here expressed in terms of δ-functions and with the overall number density ρ and a particle distance $r = |\mathbf{r} - \mathbf{r}'|$. The radial distribution function $g^{(2)}(r) = g(r)$ is of special importance for the understanding of fluids. First, $g(r)$ quantifies how much the structure of a fluid deviates from complete randomness at distance r. This can be seen by writing Eqs. 2.20 as $\rho^{(2)} = \rho^2 g(r)$ where $g(r)$ corrects the homogenous density of the ideal gas ρ for particle correlations. Secondly, it can be measured by scattering experiments, which allows direct insight into the real structure and gives straight forward possibilities for comparison with results from computer simulations. In the later, its representation via δ-functions is exploited to calculate a histogram $H(r)$ counting all pair distances r falling into certain bins of width Δr. The normalized ensemble average of $H(r)$ is then compared to the corresponding histogram of the ideal gas

$$H_{ideal}(r) = \frac{4}{3}\pi\rho[(r + \Delta r)^3 - r^3] \tag{2.22}$$

which yields

$$g(r) = \frac{< H(r) >}{N H_{ideal}(r)}. \tag{2.23}$$

Note that in a two-dimensional setup, the histogram $H_{ideal} = \pi\rho[(r+\Delta r)^2 - r^2]$ has to be used for comparison.

Finally, the knowledge of $g(r)$ allows to calculate many thermodynamic properties, e.g. the isothermal compressibility or the total correlation function introduced in the next section.

2.5 Direct Correlation Function

In Density Functional Theory (DFT), the Helmholtz free energy F is treated as a functional of the particle density $\rho^{(1)}(\mathbf{r})$ and can be separated into an ideal part and an excess part [136]

$$F[\rho^{(1)}(\mathbf{r})] = F^{id}[\rho^{(1)}(\mathbf{r})] + F^{ex}[\rho^{(1)}(\mathbf{r})] \tag{2.24}$$

accounting for contributions from configuration and interaction, respectively. The ideal part is given by

$$F^{id} = k_B T \int \rho^{(1)}(\mathbf{r})(\ln[\lambda_T^3 \rho^{(1)}(\mathbf{r})] - 1) d\mathbf{r} \tag{2.25}$$

with $\lambda_T = \sqrt{h^2/2\pi m k_B T}$ being the thermal wavelength and h the Planck constant.

The definition of the direct correlation function is related to the second functional derivative of the excess part of the free energy functional with respect to the single particle density

$$c^{(2)}(\mathbf{r},\mathbf{r}') = -\beta \frac{\delta^2 F^{ex}[\rho^{(1)}(\mathbf{r}]}{\delta\rho^{(1)}(\mathbf{r})\delta\rho^{(1)}(\mathbf{r}')}. \tag{2.26}$$

In general, the excess part of the free energy functional is unknown and has to be approximated, but there exist explicit expression for the direct correlation function $c^{(2)}_{HS}$ of the Hard-Sphere system in three dimensions [137]. However, for the two-dimensional Hard-Disc system exist only approximated expressions [138].

In this work the (quite accurate) expression of Guo and Riebel [139]

$$\begin{aligned} c^{(2)}_{HS,2D}(r,\eta) = \Theta(1-r)[&-\frac{1-q\eta^2}{(1-2\eta+q\eta^2)^2}] \\ &\{1-a^2\eta+\eta\frac{2}{\pi}[\arccos(r/a)-r/a(1-r^2/a^2)^{\frac{1}{2}}]\} \end{aligned} \tag{2.27}$$

with

$$\begin{aligned} \eta &= \rho\pi\sigma^2/4 \\ q &= (4\sqrt{3}\pi - 12)/\pi^2 \\ a &= 0.3699\eta^4 - 1.2511\eta^3 + 2.0199\eta^2 - 2.2373\eta + 2.1 \end{aligned} \tag{2.28}$$

will be used. More complicated pair interactions can be treated by certain approximations, like the random phase approximation.

2.5.1 Random phase approximation

The *random phase approximation* is based on the idea to separate the interaction potential $u(\mathbf{r},\mathbf{r}')$ into a reference part u_r (e.g., hard sphere interaction) and a perturbation part u_p (short ranged attraction)

$$u_\lambda(\mathbf{r},\mathbf{r}') = u_r(\mathbf{r},\mathbf{r}') + \lambda u_p(\mathbf{r},\mathbf{r}') \quad \lambda \in [0,1] \tag{2.29}$$

where λ controls the strength of the perturbation. Then, the pair density $\rho^{(2)}(\mathbf{r},\mathbf{r}')$ is related to the excess part of the free energy functional [136] via a functional derivative

$$\rho^{(2)}(\mathbf{r},\mathbf{r}') = 2\frac{\delta F^{ex}[\rho^{(1)}(\mathbf{r}]}{\delta u_\lambda(\mathbf{r},\mathbf{r}')} \tag{2.30}$$

with respect to the interaction potential $u(\mathbf{r},\mathbf{r}')$.

Integration of Eq. [2.30] allows to express the excess free energy functional as

$$\begin{aligned} F^{ex}[\rho^{(1)}(\mathbf{r})] = F^{ex}_r[\rho^{(1)}(\mathbf{r})] \\ +\frac{1}{2}\int\int \rho^{(1)}(\mathbf{r})\rho^{(1)}(\mathbf{r}')u_p(\mathbf{r},\mathbf{r}')d\mathbf{r}d\mathbf{r}' + F_{corr}[\rho^{(1)}(\mathbf{r})] \end{aligned} \tag{2.31}$$

with

$$F_{corr}[\rho^{(1)}(\mathbf{r})] = \frac{1}{2}\int_0^1 d\lambda \int\int \rho^{(1)}(\mathbf{r})\rho^{(1)}(\mathbf{r}')h^{(2)}((\mathbf{r},\mathbf{r}');\lambda)u_p(\mathbf{r},\mathbf{r}')d\mathbf{r}d\mathbf{r}' \quad (2.32)$$

being the contribution to F^{ex} from perturbations. In a mean field approximation this part can be neglected and forming the second functional derivative with respect to $\rho^{(1)}(\mathbf{r})$ defines the *direct correlation function in the random phase approximation*

$$\begin{aligned} c^{(2)}(\mathbf{r},\mathbf{r}') &= -\beta\frac{\delta^2 F^{ex}[\rho^{(1)}(\mathbf{r}]}{\delta\rho^{(1)}(\mathbf{r})\delta\rho^{(1)}(\mathbf{r}')} \\ &\approx c_r^{(2)}(\mathbf{r},\mathbf{r}') - \beta u_p(\mathbf{r},\mathbf{r}') \end{aligned} \quad (2.33)$$

where $c_r^{(2)}$ is the reference part for which we use $c_{HS,2D}^{(2)}(r,\eta)$ from Eq. [2.27]. It is well accepted that the expression $-\beta u_p(\mathbf{r},\mathbf{r}')$ is a good approximation of the direct correlation function $c^{(2)}(\mathbf{r},\mathbf{r}')$ for large distances. Hence, the perturbation contains the long-range part of the potential.

2.6 Ornstein-Zernike Equation

The Ornstein-Zernike equation

$$h^{(2)}(\mathbf{r},\mathbf{r}') = c^{(2)}(\mathbf{r},\mathbf{r}') + \int c^{(2)}(\mathbf{r},\mathbf{r}'')\rho^{(1)}(\mathbf{r}'')h^{(2)}(\mathbf{r}'',\mathbf{r}')d\mathbf{r}'' \quad (2.34)$$

relates the pair distribution function to the direct correlation function $c^{(2)}$ via the definition of the total correlation function

$$h^{(2)}(\mathbf{r},\mathbf{r}') = g^{(2)}(\mathbf{r},\mathbf{r}') - 1. \quad (2.35)$$

The idea behind the Ornstein-Zernike equation is that the total correlation between two particles can be split into a direct correlation between them and 'higher order contributions' mediated by a third, fourth and so on particle. Therefore, the Ornstein-Zernike equation has in principle to be solved recursively. For a uniform and isotropic fluid Eq. [2.34] simplifies to

$$h^{(2)}(r) = c^{(2)}(r) + \rho\int c^{(2)}(|\mathbf{r}-\mathbf{r}'|)h^{(2)}(r')d\mathbf{r}' \quad (2.36)$$

and the indirect correlations appear as a convolution integral. Finally, applying a Fourier transformation on Eq. [2.36] and using the convolution theorem yields the relation

$$H(\mathbf{k}) = C(\mathbf{k}) + \rho C(\mathbf{k})H(\mathbf{k}) \quad (2.37)$$

with $H(\mathbf{k})$ and $C(\mathbf{k})$ being the Fourier transforms of $h^{(2)}(r)$ and $c^{(2)}(r)$, respectively. In the long wavelength limit ($|\mathbf{k}| = 0$), the Fourier transformation reduces to

$$H(0) = \int [g(r) - 1]d\mathbf{r}. \quad (2.38)$$

2.7 Kirkwood-Buff Equation

The isothermal compressibility in a statistical ensemble is defined by [140] the change of volume V with pressure P at constant temperature T via

$$\chi_T = -\frac{1}{V}(\frac{\partial V}{\partial P})_T. \tag{2.39}$$

In the Grand canonical ensemble, fluctuations $< (\Delta N)^2 >$ in the mean particle number $\bar{N}$ can be related to the isothermal compressibility

$$\rho k_B T \chi_T = \frac{< (\Delta N)^2 >}{\bar{N}}. \tag{2.40}$$

using the thermodynamic relation $-\frac{1}{V}(\frac{\partial V}{\partial P}) = \frac{1}{\bar{N}\rho}(\frac{\partial \bar{N}}{\partial \mu})$ [140].

Again we see, that $\chi_T > 0$ has to be fulfilled, because $< (\Delta N)^2 > /\bar{N}$ is a positive quantity. Using Eqs. [2.16,2.17,2.18,2.19] allows to reformulate the mean square deviation of the mean particle number $< (\Delta N)^2 >$ in terms of the particle densities

$$\int\int \rho^{(2)}(\mathbf{r},\mathbf{r}') - \rho^{(1)}(\mathbf{r})\rho^{(1)}(\mathbf{r}')d\mathbf{r}d\mathbf{r}' =< N^2 > - < N > -\bar{N}^2 \tag{2.41}$$

and for a homogenous fluid then follows with Eqs. [2.40,2.20] that the isothermal compressibility can be expressed as an integral over the radial distribution function $g(r)$ yielding the *compressibility equation*

$$1 + \rho \int [g(r) - 1]d\mathbf{r} = \frac{< (\Delta N)^2 >}{< N >} = \rho k_B T \chi_T. \tag{2.42}$$

Together with Eqs. [2.37,2.38] a connection to the Fourier transform of the direct correlation function is given by

$$\rho k_B T \chi_T = [1 - \rho C(0)]^{-1}, \tag{2.43}$$

which is the *Kirkwood-Buff Equation* for an one-component system. For the isothermal compressibility calculated from the Kirkwood-Buff equation must hold $\chi_T > 0$ according to Eq. [2.40]. Note that this result was deduced from Eq. [2.36] which assumes a homogenous fluid. Hence negative compressibility indicate a thermodynamical instability of the homogeneous phase and using the direct correlation function in the random phase approximation allows to calculate χ_T.

The Kirkwood-Buff equation can be generalized towards multi-component systems with n different particle species. The equation then reads [136]

$$k_B T \chi_T = [\sum_{\alpha,\beta}^{n} \rho_\alpha \rho_\beta [\delta_{\alpha\beta}/\rho_\alpha - C_{\alpha\beta}(0)]^{-1}, \tag{2.44}$$

whereas α and β indicate the considered species, ρ_α is the number density of particles of species α and $C_{\alpha\beta}(0)$ is the Fourier transform in the long wave-length limit of the approximated direct correlation function

$$c^{(2)}_{\alpha\beta}(0) \approx c^{(2)}_{HS} - 1/k_B T u_{\alpha\beta}(\mathbf{r}, \mathbf{r}') \tag{2.45}$$

with the particle type specific interaction potential $u_{\alpha\beta}$ and the reference part $c^{(2)}_{HS}$, which is independent of the particle species in a mono-disperse system.

In case of a two-component system with particle species A and B and the corresponding densities ρ_A and ρ_B fulfilling $\rho/2 = \rho_A = \rho_B$, we find

$$\rho k_B T \chi_T = [1 - \rho/2(C_{AA}(0) + C_{AB}(0))]^{-1}, \tag{2.46}$$

because for pair interactions reasonably must hold $u_{\alpha\beta} = u_{\beta\alpha}$, which implies $C_{\alpha\beta}(0) = C_{\beta\alpha}(0)$ in the random phase approximation.

In contrast to an one component system, where the instability of the homogeneous phase results in phase separation of i.e., liquid and vapor, one can find demixing processes in thermodynamically unstable multi-component system. These different types of instabilities can not be distinguished by considering solely the isothermal compressibility according to Eq. [2.44]. However, there exist more general theoretical descriptions allowing such characterization of different instabilities [141].

3

Theoretical Models of Complex Dipolar Colloids

In this chapter we introduce common interaction potentials used for modeling colloidal particles. Based on these potentials we construct more complex models for dipolar particles under the presence of external inductive fields. In total, it is four different models. First the DDP model for dipolar microswimmers and a related model of reduced complexity. Secondly, we model superparamagnetic particles under the presence of crossed electric and magnetic fields (CDP model), but also introduce a generic model for colloids with mutidirectional induced interactions. Additionally, we discuss visualization and structure analysis techniques which we developed to understand structures formed by dipolar colloids.

In general, colloidal particles are subject to a large variety of forces and pair interactions e.g., Van der Waals forces, depletion forces or electrostatic forces. Throughout this work we will consider different particle models, most of them related to dipolar interactions. In all of these models, it is assumed that the particles interact sterically and bear some additional (dipolar) interaction properties. However, influences of van der Waals forces or electrostatic repulsion are not considered, unless stated otherwise. This is because we want to isolate and analyze the influence of the dipolar interactions. This approach is justified by the fact that we can always assume a stable homogeneous phase of solely repulsive non-dipolar particles as the initial state of our system. Exposing these particles to external fields and inducing relatively strong dipolar interactions then allows to investigate the influence of the dipolar interactions

without being superimposed by other forces e.g., van der Waals. However, hydrodynamic interactions are not considered here, although they might influence the systems behavior significantly [7].

3.1 Colloidal Interaction Potentials

In this section we shortly discuss basic models for pair-interactions between colloidal particles, which are frequently used in computer simulations. The introduced interactions will be used, extended and recombined in the following parts of this Chapter, where more complex particle models are constructed. The present section serves as a brief overview of the basic constituents of these more complex models.

The Lennard-Jones potential

The Lennard-Jones (LJ) potential is an isotropic pair potential with repulsive and attractive parts. It is given by

$$U_{LJ} = 4\epsilon[(\sigma/r)^{12} - (\sigma/r)^{6})], \tag{3.1}$$

whereas r is the particle center-to-center distance and σ the particle diameter. The potential depth, controlling the interaction strength, is given by ϵ. The r^{-6} dependence is used to model attractive van-der-Waals interactions between neutral atoms, while the r^{-12} dependence results in very rapid increase of repulsion for distances $r < \sigma$.

The soft-sphere potential

Based on the Lennard Jones potential $U_{LJ}(r)$ a so called Soft-Sphere $U_{SS}(r)$ (or Soft-Disk in two-dimensions) potential can be defined by truncating U_{LJ} at $r^c = 2^{1/6}\sigma$ and shifting it by ϵ. The resulting interaction

$$U_{SS}(r) = 4\epsilon[(\sigma/r)^{12} - (\sigma/r)^{6})] + \epsilon \quad \text{for} \quad r < 2^{1/6}\sigma \tag{3.2}$$

is then solely repulsive and can be used to mimic sterical interactions between colloidal particles (as done throughout this work). An important feature of this Soft-Sphere potential is that it decays continuously and vanishes at the truncation distance r^c. This is of special importance for its utilization in Brownian dynamics computer simulations where the force

$$\mathbf{F}_{ij}^{SS}(\mathbf{r}_{ij}) = -\boldsymbol{\nabla}_{\mathbf{r}_i} U_{SS}(r_{ij}) \quad \text{with} \quad \mathbf{r}_{ij} = \mathbf{r}_i - \mathbf{r}_j \tag{3.3}$$

imposed on particle i at position $\mathbf{r}_i$ by particle j at position $\mathbf{r}_j$ is then well defined and yields no 'jump' at the truncation distance $r_{ij}^c = 2^{1/6}\sigma$.

The Yukawa interaction potential

A point-charge Q or an uniformly charged spherical shell with diameter σ and total charge Q generates an electric field according to the coulomb potential

$$U_{cou}(r) = \frac{1}{4\pi\epsilon_0}\frac{Q}{r} \quad \text{for} \quad r > \sigma, \tag{3.4}$$

with ϵ_0 being the electric constant. Such an uniformly charged shell can be seen as a basic model for a colloidal particle in a fluid. The specific mechanisms by which the colloidal surface becomes charged are manifold, e.g. dissociation of surface molecules, and depend on the material and solvent properties [7].

Importantly, once the particle surface is charged, ionized solvent particles of opposite electrical charge are attracted towards it. They form a cloud of counter-ions, the so called the electrical double layer (EDL), around the colloid and partially screen the Coulomb potential $U_{cou}(r)$. The resulting effective potential is then given by the functional form of the Yukawa interaction [7]

$$U_{yu}(r_{ij}) = q^2 \frac{\exp(-\kappa r_{ij})}{r_{ij}/\sigma}, \tag{3.5}$$

with the inverse length κ^{-1} describing the strength of the screening and the interaction strength parameters $q_i = q_j = q \propto Q$. In experiment, strong screenings with $\kappa \approx 10\sigma^{-1}$ can be achieved via increasing counter-ion concentrations by externally introduced electrolytes [7].

The dipole-dipole interaction

The dipole-dipole interaction between two point dipoles $\boldsymbol{\mu}_i$ and $\boldsymbol{\mu}_j$ at positions $\mathbf{r}_i$ and $\mathbf{r}_j$ and distance $\mathbf{r}_{ij} = \mathbf{r}_i - \mathbf{r}_j$ is given by [142]

$$U_{dip}(\mathbf{r}_{ij}, \boldsymbol{\mu}_i, \boldsymbol{\mu}_j) = \frac{\boldsymbol{\mu}_i \cdot \boldsymbol{\mu}_j}{r_{ij}^3} - 3\frac{(\boldsymbol{\mu}_i \cdot \mathbf{r}_{ij})(\boldsymbol{\mu}_i \cdot \mathbf{r}_{ij})}{r_{ij}^5} \tag{3.6}$$

and is an example for an anisotropic long-ranged pair interaction. Due to its anisotropy, the dipole-dipole interaction results in torques between the two dipoles. It can be used to describe magnetic or electric dipoles and is a standard expression used in models of dipolar colloids.

In these models, the dipole moments $\boldsymbol{\mu}_i$ can either be seen as induced by external fields or as being permanent. Torques are usually neglected for induced dipole moments while the orientation of permanent dipole moments is fixed to the geometry of the particles carrying them. Then torques act on the particle itself. The later means that phenomena like the Neel relaxation are neglected, which is reasonable for not too small

particles [143]. Finally, in computer simulations one usually defines the so called dipolar coupling strength (here for a two-dimensional system)

$$\lambda = \mu^2 / k_B T \tag{3.7}$$

giving the ratio between the strength of dipolar interactions and thermal energy. Once this ratio becomes $\lambda \approx k_b T$, the dipole-dipole interactions start to influence the collective particle behavior significantly.

3.1.1 Representations of anisotropic pair interactions in two-dimensions

In the following, the dipole-dipole interaction, as presented in Eq. [3.6], will be used to model complex dipolar colloids. Before presenting more complex models, we want to introduce a simple visualization technique, which allows to understand intuitively the interaction patterns between dipolar particles. To this end, we start with a hard sphere of diameter σ in the center of a two-dimensional coordinate frame with position vector $\mathbf{r}_1 = (0, 0)$. We place a dipole moment of strength $\mu = \sqrt{\sigma^3 \epsilon}$ in the center of this sphere, whereas ϵ is an arbitrary unit of energy. The dipole moment has a fixed orientation and points along the y-direction. Hence, the dipole moment is given by $\boldsymbol{\mu} = \mu \mathbf{e}_y$.

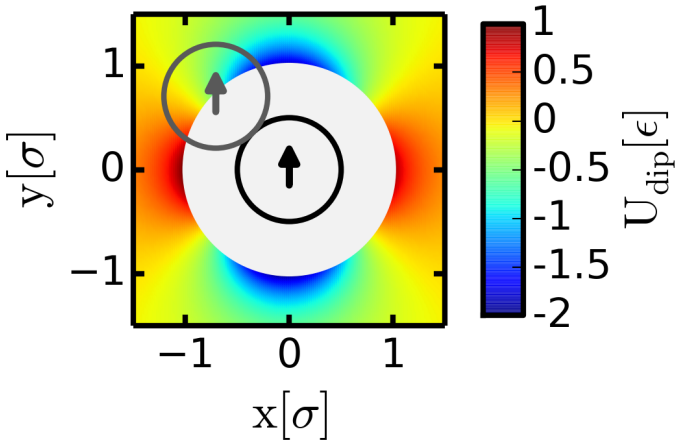

Figure 3.1: A dipolar disc of diameter σ (solid circles) in the center of the two-dimensional x-y plane. The particles dipole moment is indicated by an arrow in its center and points along the y-axis. The energy U_{dip} is calculated according to Eq. [3.6] for a fictitious second particle of equal kind at various positions $\mathbf{r}$ and given in units of ϵ. This probing particle is indicated by a gray circle and arrow at an arbitrary position. The color code gives the interaction energy 'landscape'. The white circle around the central particle indicates the excluded area.

The dipolar interaction energy between this particle and another particle of equal kind at arbitrary positions $\mathbf{r}_2$ can be calculated from Eq. [3.6]. The set of energies $U_{dip}(\mathbf{r}_{12})$ can be visualized as a color map in the x-y plane. This results in an energy 'landscape' as shown in Fig. 3.1. In this representation, it is easy to see the preference of dipolar particles to form head-tail arrangements by the low energy regions around the head and bottom of the central particle.

Such an energy 'landscape' might seem trivial when considering a dipolar particle with one central dipole moment, but may help a lot in understanding interaction patterns between particles carrying several dipole moments. Please note that such a representation becomes less powerful in case the orientations of dipole moments are free to rotate or three-dimensional quantities. However, in this work we are investigating systems effectively confined to two dimensions with induced, orientationally fixed, dipolar interactions.

3.2 The DDP Model for Dipolar Microswimmers in Experiment

In the present section we introduce the double dipole particle (DDP) model. The experimental particles motivating this work are gold-patched dielectric spheres confined between two glass plates, forming a quasi-2D geometry [55]. Application of an in-plane AC electric field induces dipole moments in both, the gold and the dielectric part of the particles, with the gold's dipole being significantly larger due to its larger polarizability. Additionally, the plane between gold patched and dielectric part become aligned along the field. At low frequencies these two induced dipoles have the same orientation (along the field). Placed into an aqueous solution, one observes [55] a spontaneous motion of each particle in the direction *orthogonal* to the field and away from the particle's gold patch. The underlying mechanism is an asymmetric flow of solvent charges, usually called induced-charge electrophoresis [55, 54]. To examine the collective behavior of these driven particles, we perform BD simulations in a 2D quadratic cell of size L^2 with periodic boundary conditions. The cell contains $N = 800$ spherical particles with equal diameter σ defining a unit length. Particle positions are denoted by $\mathbf{r}_i = x_i\mathbf{e}_x + y_i\mathbf{e}_y$ $(i = 1,..,N)$ with the unit vectors $\mathbf{e}_x$ and $\mathbf{e}_y$ defining a 2D coordinate frame. The external, electric field $\mathbf{E}_{ext}$ points along the y-axis. Sterical interactions are modeled by a soft-sphere (SS) potential

$$U_{SS}(\mathbf{r}_{ij}) = 4\epsilon_{SS}\left((\sigma/r_{ij})^{12} - (\sigma/r_{ij})^{6} + 1/4\right) \tag{3.8}$$

truncated at $r_{ij}^c = 2^{\frac{1}{6}}\sigma$, where $r_{ij} = |\mathbf{r}_j - \mathbf{r}_i|$ is the particle distance. The strength of repulsion is set to $\epsilon_{SS}^* = \epsilon_{SS}/k_BT = 10$ where k_B is Boltzmann's constant and T is the temperature. To mimic the impact of the propulsion force we randomly assign to each particle a fixed vector $\mathbf{s}_i = s_i\mathbf{e}_x$ which points either to the 'right' $(s = 1)$ or to the 'left' $(s = -1)$ with probability 0.5, respectively. Thereby a random fifty-fifty mixture of two different particle 'species' is created. Each particle is then subject to a constant but orientation-dependent driving force $\mathbf{f}_{d,i} = f_d\mathbf{s}_i$. Changes of particle orientation (s_i) are not considered here.

To incorporate the dipolar interactions we assume that each particle i bears two point dipole moments $\boldsymbol{\mu}_i^{(1)}$ and $\boldsymbol{\mu}_i^{(2)}$ whose orientation is fixed along the external field , i.e. $\boldsymbol{\mu}_i^{(\alpha)} = \mu_i^{(\alpha)}\mathbf{e}_y$, $\alpha = 1,2$. Moreover, the two dipole-moments are shifted out of the particle center by $\boldsymbol{\delta}_{s_i}^{(1)} = \delta\mathbf{s}_i$ and $\boldsymbol{\delta}_{s_i}^{(2)} = -\delta\mathbf{s}_i$ with $\delta = 0.25\sigma$. The values of $\mu_i^{(\alpha)}$ are hold constant (that is, we neglect variations of the local field) and set differently in order to mimic the strong asymmetry of the metallo-dielectric Janus-particles. Specifically, we choose $\mu_i^{(2)} = 2\mu_i^{(1)}$ and set the dimensionless dipole strength to $\mu^* \equiv \mu_i^{(2)^*} = \mu_i^{(2)}/\sqrt{\sigma^3 k_B T}$. Test simulations revealed that the system's be-

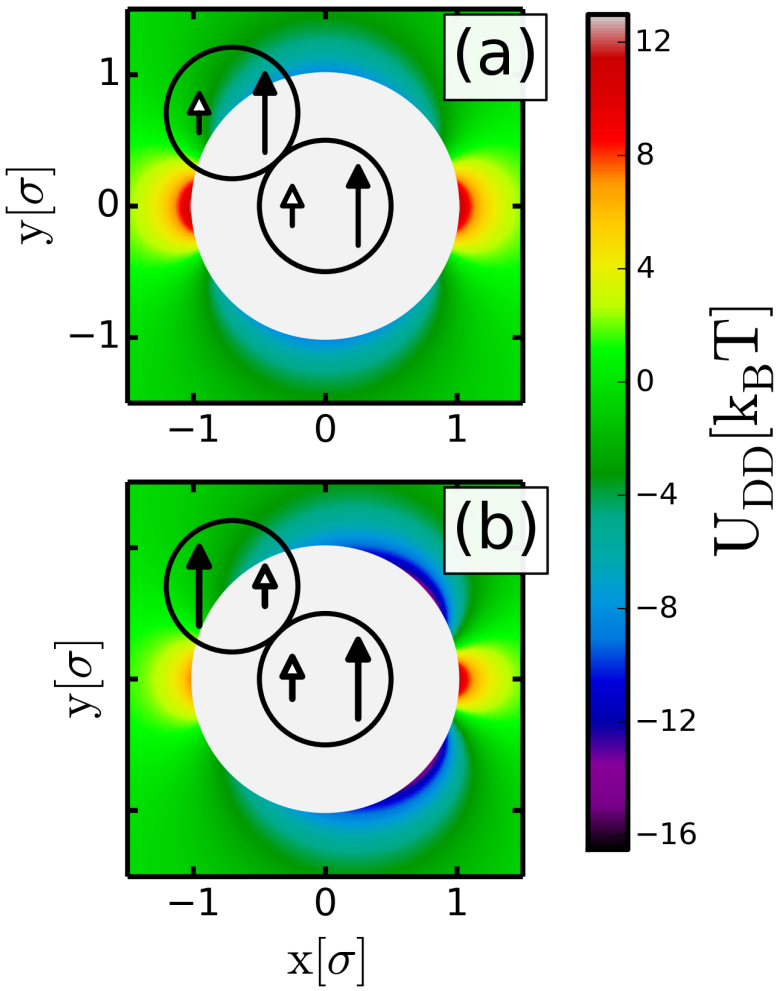

Figure 3.2: Potential energy 'landscape' due to the total dipolar interaction (see color code) for two DDPs of diameter σ (solid circles) with (a) $s_i = s_j = -1$ and (b) $s_i = 1, s_j = -1$ in a top-view perspective for $(\mu^1)^* = 1.58$. The particle dipole moments are indicated by arrows with a white [black] head for $\boldsymbol{\mu}^{(1)}$ [$\boldsymbol{\mu}^{(2)}$]. The white circle around the centered particle indicates the excluded area.

havior is only weakly sensitive to the ratio μ_2/μ_1, whereas changing the shift parameter δ has a strong effect. Here we stick to a value of δ already used in Ref. [95] for the case of oppositely oriented dipoles. The distance between two arbitrary dipole moments $\boldsymbol{\mu}_i^{(\alpha)}$ and $\boldsymbol{\mu}_j^{(\gamma)}$ of different particles is given by

$$\mathbf{r}_{s_i s_j}^{\alpha\gamma} = \mathbf{r}_j + \boldsymbol{\delta}_{s_j}^{\gamma} - (\mathbf{r}_i + \boldsymbol{\delta}_{s_i}^{\alpha}). \tag{3.9}$$

The dipolar interaction between the two of them is calculated via the 3D point dipole potential

$$\begin{aligned} U_{dip}(\mathbf{r}_{ij}, \boldsymbol{\mu}_i^{(\alpha)}, \boldsymbol{\mu}_j^{(\gamma)}, s_i, s_j) = \boldsymbol{\mu}_i^{(\alpha)} \cdot \boldsymbol{\mu}_j^{(\gamma)} (r_{s_i s_j}^{\alpha\gamma})^{-3} \\ - 3(\boldsymbol{\mu}_i^{(\alpha)} \cdot \mathbf{r}_{s_i s_j}^{\alpha\gamma})(\boldsymbol{\mu}_j^{(\gamma)} \cdot \mathbf{r}_{s_i s_j}^{\alpha\gamma})(r_{s_i s_j}^{\alpha\gamma})^{-5}, \end{aligned} \tag{3.10}$$

and the total dipolar interaction between two particles is given by the sum

$$U_{DD}(\mathbf{r}_{ij}, s_i, s_j) = \sum_{\alpha,\gamma=1}^{2} U_{dip}(\mathbf{r}_{ij}, \boldsymbol{\mu}_i^{(\alpha)}, \boldsymbol{\mu}_j^{(\gamma)}, s_i, s_j). \tag{3.11}$$

We use the standard 2D Ewald summation method to handle the long-range character of the dipole interactions [144]. Combining U_{DD} and the formerly introduced SS potential defines the 'double-dipole particle' (DDP) model

$$U_{DDP} = U_{DD} + U_{SS}. \tag{3.12}$$

The angle dependency for distances $r_{ij} > \sigma$ is illustrated in Fig. 3.2. It is seen that two identical DDPs ($s_i = s_j$) prefer a head-to-tail configuration similar to "single-dipole" particles with one dipole in their center. In contrast, for DDPs with $s_i \neq s_j$, the most attractive configurations are staggered in the sense that one DDP is shifted towards the gold-patched 'back' of the other particle. The corresponding minimum energy $U_{DD}^{min}(s_i \neq s_j)$ is roughly $4k_BT$ larger than in the head-to-tail configuration $U_{DD}^{min}(s_i = s_j)$. The overdamped BD equations of motion are given by

$$\gamma \dot{\mathbf{r}}_i = \sum_{j=1}^{N} \nabla U_X(ij) + \mathbf{f}_{d,i}^{s} + \zeta_i \tag{3.13}$$

where γ is the friction constant, $U_X(ij)$ is a specific pair potential (with $X = SS$, DDP, or LJ), and ζ_i is a Gaussian noise vector which acts on particle i and fulfills the relation $\langle \zeta_i \rangle = 0$ and $\langle \zeta_i(t) \zeta_j(t') \rangle = 2\gamma k_B T \delta_{ij} \delta(t - t')$. Hydrodynamic interactions (HI) are neglected, in accordance with earlier studies [92] revealing that HI do not alter lane formation qualitatively. The BD equations are solved via the Euler scheme [135] with an integration step width $\Delta t = 10^{-5} \tau_b$, where τ_b is a Brownian timescale defined by $\tau_b = \sigma^2 \gamma / k_B T$.

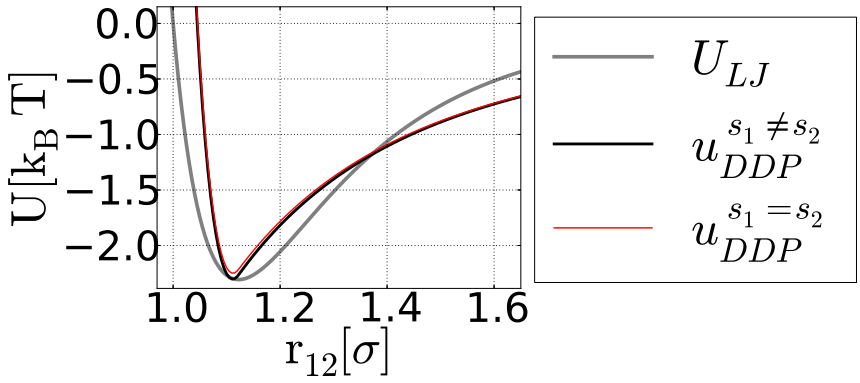

Figure 3.3: Angle-averaged DDP potential for $s_1 = s_2$ and $s_1 \neq s_2$ at $\mu^* = 1.58$. Included is the LJ potential at $\epsilon^* = 2.3$.

3.2.1 The driven Lennard Jones fluid - A generic model for attractive microswimmers

Besides the anisotropy, another main feature characterizing the DDP interactions is that they are *effectively attractive*. This is seen from the angle-averaged potential

$$u_{DD}(r_{12}) = \frac{1}{2\pi}\int_0^{2\pi} U_{DD}\left(\mathbf{r}_{12}, s_1, s_2\right) d\Omega_{12}, \tag{3.14}$$

with Ω_{12} being the angle of the connecting vector $\mathbf{r}_{12}$ relative to the x-axis. Numerical data for the cases $s_1 = s_2$ and $s_1 \neq s_2$ are shown in Fig. 3.3. Clearly both angle-averaged potentials display a pronounced, attractive potential well with nearly identical depths. In fact, the angle-averaged potential somewhat resembles that of an LJ fluid (also plotted in Fig. 3.3), disregarding differences in the width of the attractive well and the decay of the potentials with r_{12}. Hence, we also consider a driven LJ fluid characterized by the pair potential $U_{LJ} = 4\epsilon((\sigma/r_{ij})^{12} - (\sigma/r_{ij})^6)$ with cut-off at 2.5σ and dimensionless interaction strength $\epsilon^* = \epsilon/k_BT$. Except of the Interaction potential, the general set up is the same as in the DDP model. Specifically, the equations of motion (Eqs. [3.13]), the distribution of orientations s_i and the driving f_d acting on particle i. In the following the reduced units used in this chapter are summarized.

Tabular representation of reduced units.

reduced density	$\rho^* = \rho\sigma^2$
reduced driving force	$f_d^* = f_d\sigma/k_BT$
reduced dipole moment	$\mu^* \equiv \mu_i^{(2)^*} = \mu_i^{(2)}/\sqrt{\sigma^3 k_B T}$
reduced LJ coupling strength	$\epsilon^* = \epsilon/k_BT$

3.2.2 Target quantities

To quantify the degree of laning we introduce for every particle i a slice in x-direction with lateral width σ centered around y_i. We then assign a variable Φ_i which equals 1 if the slice contains no particle of opposite driving direction and 0 otherwise. The ensemble-averaged laning order parameter then follows as

$$\Phi = \langle \sum_{i=1}^{N} \Phi_i / N \rangle, \tag{3.15}$$

where the brackets denote a time average. Non-laned states are characterized by $\Phi \approx 0$ whereas perfectly laned states correspond to $\Phi = 1$. However, the system can visually appear as being laned already at much smaller values of Φ (e.g., $\Phi \approx 0.2$), especially at high densities.

To characterize the local structure in x-direction we calculate the radial distribution function between particles of the same type

$$g^s(x) = \frac{2}{\rho N} \langle \sum_{i=1}^{N} \sum_{j \neq i}^{N} \delta(x - |x_{ij}|) \Theta(\sigma - |y_{ij}|) \Theta(s_i s_j) \rangle \tag{3.16}$$

with x_{ij} (y_{ij}) being the x (y)-component of $\mathbf{r}_{ij}$, and δ and Θ are the delta- and the Heavyside step function, respectively. By normalization, $g^s(x)$ decays to 2 for $x \to \infty$ in a single-species fluid and to 1 in a completely mixed binary fluid. By interchanging x and y in Eq. [4.2] we additionally define the correlation function $g^s(y)$ in y-direction.

3.3 Colloids in Crossed Fields

In this section we are particularly interested in modeling the field-directed aggregation of colloids with field-induced dipolar interactions. A previously studied example for such systems is capped (metal-coated) dielectric particles under the presence of an uni-axial electric field inducing quadrupolar-like interactions [26, 95]. Also mixtures of para- and diamagnetic colloids under the presence of an uni-axial magnetic field suspended in a ferromagnetic carrier fluid [98] have been considered. In these studies, it is one external field which allows to tune the aggregated structures with respect to one direction. Here we consider even more complex interactions caused by *crossed* (orthogonal) fields, allowing bi-directional tuning of particle aggregation.

Before discussing the experimental system presented in see Sec. 1.3.3 we briefly mention another example of a possible experimental realization of tunable bi-directional aggregation. which is a quasi two-dimensional system of suspended dielectric colloidal particles under the influence of two in-plane orthogonal AC electric fields with a phase shift of π. The fields will polarize the particles' ionic layer and/or dielectric material periodically but at different times due to their phase shift. We assume that by adjusting the field frequencies and phases to the relevant timescales governing particle diffusion and the relaxational dynamics of the polarized ionic layer, two decoupled orthogonal dipole moments in each particle can be generated by this setup.

The actual experimental setup we are modeling is a quasi two dimensional system of suspended colloidal particles, each composed of super-paramagnetic iron-oxide aggregates embedded in a polymer matrix, which has been investigated experimentally by Dr. Bharti [25, 133]. In this case, crossed external electric and magnetic fields, oriented in plane but perpendicular to each other, can be used to induce independent electric and magnetic dipole moments in the colloids, which leads to a directed self-assembly process of two-dimensional single-particle chain networks. An experimental photograph of the resulting structures is shown in Fig. 1.6 (e) and experimental details are described in Sec. 1.3.3. Please note that the oscillation of the AC electric field does not induce a magnetic field in the assembly plane. Thus, magnetic and electric interactions are decoupled in this setup. This follows directly from the fourth Maxwell equation (Ampere's circuital law)

$$\int_{\partial\Sigma} \mathbf{H} \cdot d\mathbf{l} = \int_{\Sigma} (\mathbf{j} + \partial_t \mathbf{E}) \cdot d\mathbf{s} \tag{3.17}$$

where $\mathbf{E}$ is the oscillating electric field, $\mathbf{j}$ is the electric current density and $d\mathbf{s}$ denotes the differential vector element of the assembly plane (surface) Σ. As $d\mathbf{s}$ is normal to the surface and thus also to the electric field $\mathbf{E}$ and the current density $\mathbf{j}$, the right hand side of Eq. [3.17] vanishes *inside*

the plane. In fact, the experimental setup corresponds to a current sheet, and it can be shown that the strength of the induced magnetic field grows linear with increasing lateral distance from the plane [145]. Thus, for a quasi two-dimensional experimental assembly chamber of lateral size in the range of a few micrometers the magnetic field which is induced by the oscillation of the external electric field can be neglected.

In the following, two different models for field-directed aggregation are presented. But before, we shortly comment on general properties of the induced dipole moments.

Interaction potential of crossed point dipoles

The crossed orthogonal external fields induce orthogonal dipole moments $\boldsymbol{\mu}^m = \mu \mathbf{e}_m$ and $\boldsymbol{\mu}^e = \mu \mathbf{e}_e$, which we term for simplicity as 'magnetic (m)' and 'electric (e)' dipoles (although one might also think of two electric moments). The coordinate frame is adjusted to coincide with the directions of these moments so that $\mathbf{e}_m = \mathbf{e}_x$ and $\mathbf{e}_e = \mathbf{e}_y$. In general, these moments can have different absolute values, but for simplicity they are assumed to be equal in this preliminary consideration. The two types of dipole moments are also assumed to be independent from each other, meaning that they interact only with dipole moments of the same type on other particles.

Intuitively, one would model the interaction energy between dipoles of particles 1 and 2 by the point-dipole potential

$$U^{\alpha}_{dip}(\mathbf{r}_{12}) = \frac{\boldsymbol{\mu}^{\alpha}_1 \cdot \boldsymbol{\mu}^{\alpha}_2}{r^3_{12}} - 3\frac{(\boldsymbol{\mu}^{\alpha}_1 \cdot \mathbf{r}_{12})(\boldsymbol{\mu}^{\alpha}_2 \cdot \mathbf{r}_{12})}{r^5_{12}}, \tag{3.18}$$

where α indicates the dipole type as being either e or m. Due to the constraint $\boldsymbol{\mu}^{\alpha}_1 \parallel \boldsymbol{\mu}^{\alpha}_2$ it follows that

$$U^{\alpha}_{dip}(\mathbf{r}_{12}) = \frac{\mu^{\alpha}_1 \mu^{\alpha}_2}{r^3_{12}}(1 - 3\frac{(\mathbf{r}_{12} \cdot \mathbf{e}_{\alpha})^2}{r^2_{12}}). \tag{3.19}$$

The resulting total dipolar interaction between two particles is the sum of the dipolar potentials stemming from the magnetic and electric dipoles, respectively. Using $\mu = |\boldsymbol{\mu}^{\alpha}_i|$ and the relation $(\mathbf{r}_{12} \cdot \mathbf{e}_e)^2 + (\mathbf{r}_{12} \cdot \mathbf{e}_m)^2 = r^2_{12}$ (which holds since $\boldsymbol{\mu}^e$ and $\boldsymbol{\mu}^m$ are orthogonal) we obtain

$$U^{e}_{dip}(\mathbf{r}_{12}) + U^{m}_{dip}(\mathbf{r}_{12}) = -\frac{\mu^2}{r^3_{12}}. \tag{3.20}$$

The resulting interaction on the right side of Eq. [3.20] is an isotropic, purely attractive interaction that lacks any kind of directional character. Therefore, the potential defined in Eq. (3.20) can not generate any directed and/or rectangular structures as observed in experiments (see Fig. 1.6(a)-(d) and [25, 133]). Underlying reasons for the more complex character of the true interactions might be many-body effects like mutual depolarization [146, 147, 148], and/or nonuniform intra particle properties e.g.,

the distribution of magnetic material inside particles [149]. Hence, the following parts of this chapter are concerned with more complex models.

3.4 The CDP Model for Superparamagnetic Particles in Experiment

In the present section we introduce the crossed dipole particle (CDP) model, to describe the superparamagnetic particles of the experimental setup introduced in Sec. 1.3.3. There, superparamagnetic polymer particles in a quasi two-dimensional setup are exposed to crossed electric and magnetic fields. In Fig. 1.6(a) and (c) it can be seen that the influences of the magnetic and electric fields on the self-assembly processes differ strongly. While the presence of an electric field (Fig. 1.6(a)) results in straight single particle chains oriented along the electric field, the externally induced magnetic interactions result in more compact (staggered) chain-like aggregates pointing along the magnetic field (Fig. 1.6(c)) when no electric field is applied.

On the origin of induced magnetic interactions

The bidirectional assembly of particles in external fields is governed by induced dipolar interactions and results in the formation of a variety of particle structures. In the case of AC-electric field driven assembly of microparticles in aqueous dispersions, the dipoles are induced by partial polarization i.e redistribution of ions in the ionic double layer around the particles. Therefore the particles can be assumed to have a single dipole which overlaps with the center of mass of the particles. These dipole-dipole interactions lead to assembly of particles into linear chains. However, in an uniform magnetic field, dipoles are induced by polarization of local magnetic domains. In our case of composite microspheres, the magnetic domains are the superparamagnetic nanoaggregates embedded in the particles. Hence, the net magnetic dipole moment in a particle is the vector sum of all the individual dipoles induced in the embedded nanoparticles. Depending upon the spatial distribution of the individual magnetic domains, the geometric center of the sum over single magnetic moments may not overlap with the center of mass of the particles. This has been shown experimentally for similar superparamgentic beads [149]. The dislocation of the net magnetic interaction site from the center of the particle may result into partially staggered chain configurations instead of linear ones. We believe that this is the case with our superparamagnetic microparticles, where linear chains are formed in external AC-electric field and partially staggered chains are formed in an uniform magnetic field (see Fig. 1.6).

The theoretical model

To this end, the electric interactions are modeled by placing a point dipole moment $\boldsymbol{\mu}_i^{el}$ oriented along the electric field in the center of each particle

i, whereas a shifted and truncated (12,6) Lennard-Jones Potential is used to model sterical interactions between particles i and j

$$U_{SS}(\mathbf{r}_{ij}) = 4\epsilon\Big((\sigma/r_{ij})^{12} - (\sigma/r_{ij})^{6} + 1/4\Big). \tag{3.21}$$

Here, $\mathbf{r}_{ij} = \mathbf{r}_i - \mathbf{r}_j$ is the center to center distance, ϵ and σ set the units of energy and length, respectively and a spherical cut off $r_{ij}^{c,SS} = 2^{1/6}\sigma$ is applied. This setup corresponds to the well established dipolar soft sphere model [22]. To account for magnetic interactions, each particle bears additionally a magnetic dipole moment $\boldsymbol{\mu}_i^{mg}$ which is pointing along the magnetic field. In contrast to the electric case, the magnetic dipole moments are shifted out of the particle centers: For each particle this shift is given by a vector $\boldsymbol{\delta}_i$ with an orientation taken from an uniform random distribution and a constant absolute value $\delta = 0.2\sigma$. Furthermore, the absolute value of each magnetic moment is chosen from a Gaussian distribution with mean $\bar{\mu}^{mg}$ and variance $\sigma_{mg} = \bar{\mu}^{mg}/2$ under the condition that $\mu_i^{mg} \in [0, 2\bar{\mu}^{mg}]$. The latter interval is chosen to prevent unphysical negative moments and to avoid the occurrence of *very* strong moments, which is important for computational efficiency.
This model is motivated by the fact that experimental particles consist of polymer droplets incorporating numerous superparamagnetic iron-oxide aggregates. The underlying assumption is that different particles carry different amounts of magnetic material and that this magnetic material is inhomogeneously distributed throughout the particle[1] and forms localized magnetic interaction centers. The underlying reasons might be variations in the production process and polydispersity of the particles. Note that the increase of magnetic material goes cubic with the particle diameter σ, which makes larger differences in the particles magnetic response rather reasonable, even if the the distribution of particle sizes is relatively sharp. Also (localized) loss of magnetic material through the particle surface during the experiment or in storage could be considered; a process which was observed during Dr. Bharti's experiments. These assumptions are reflected in the distribution of the absolute magnetic moments μ^{mg} and in the random spatial shift $\boldsymbol{\delta}$ of the magnetic interaction site, respectively. However, the actual values for the particle parameters were not optimized or derived from experimental or theoretical insights. Instead, their choice was done by intuition. Please note that we are not aiming on the most accurate description of *single particles* but rather on an accurate description of the many particle system. Hence, we do not claim that the magnetic material is in reality distributed throughout the particles in exactly the way we model them. Furthermore, an accurate description of the magnetic properties of various interaction sites would in principle require

[1] Recently, an experimental study concluded that the magnetic properties of similar particles result from an inhomogeneous internal distribution of the magnetic material [149].

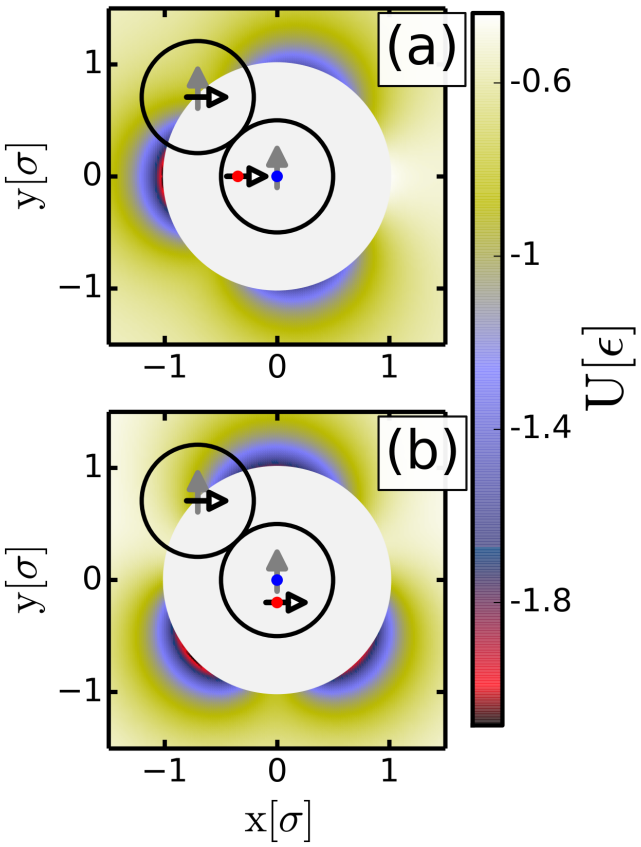

Figure 3.4: Direction-dependent pair interaction $U(\mathbf{r}_{ij})$ [see Eq. 3.24] between a particle with horizontal (a) and vertical (b) shift of magnetic interaction in the center of the coordinate frame and a second (reference) particle at various positions $\mathbf{r}_{ij}$ with no shift of the magnetic moment. Positions of the magnetic/electric dipole moments are indicated by red/blue dots and corresponding arrows. In both cases holds $\delta = 0.2\sigma$ and $\mu^{el} = \mu^{mg} = \sqrt{\epsilon\sigma^3}$. Sterically excluded areas are indicated by white circles while the color code gives the interaction energy $U(\mathbf{r}_{ij})$ in units of ϵ. These are two realizations for the random position of the magnetic moment yielding different anisotropic interaction patterns.

to calculate the magnetization self-consistently, which is again not feasible in the many particle systems we are interested in. Instead, we provide a physically motivated and reasonable model, which is reproducing the structures observed in experiment and allows to overcome the difficulties associated with the control of global and local particle density in the experiments.

Finally, both moments are induced and have therefore a fixed orien-

tation. For simplicity, we neglect torques due to off-centered magnetic interaction sites. With this particle setup, the distance between dipole moments $\boldsymbol{\mu}_i^\alpha$ and $\boldsymbol{\mu}_j^\alpha$ of species $\alpha = (el, mg)$ is given by

$$\mathbf{r}_{ij} = \mathbf{r}_j - \mathbf{r}_i + \boldsymbol{\delta}_j - \boldsymbol{\delta}_i \tag{3.22}$$

whereas $\alpha = el$ corresponds to the electric case with $\delta_{i,j} = 0$. The dipolar interaction between particles i and j is then calculated via the usual three-dimensional point dipole potential

$$U_{dip}^\alpha(\mathbf{r}_{ij}, \boldsymbol{\delta}_i, \boldsymbol{\delta}_j) = \boldsymbol{\mu}_i \boldsymbol{\mu}_j r_{ij}^{-3} - 3(\boldsymbol{\mu}_i \mathbf{r}_{ij})(\boldsymbol{\mu}_j \mathbf{r}_{ij}) r_{ij}^{-5} \tag{3.23}$$

and the total interaction potential is given by

$$U(\mathbf{r}_{ij}) = U_{SS}(\mathbf{r}_{ij}) + U_{dip}^{el}(\mathbf{r}_{ij}) + U_{dip}^{mg}(\mathbf{r}_{ij}, \boldsymbol{\delta}_i, \boldsymbol{\delta}_j). \tag{3.24}$$

Standard two-dimensional Ewald summation method is used to handle the long-range character of the dipole interactions [150, 144]. In Fig. 3.4, the interaction energy map for to random realizations of such particles is shown. Clearly, the model result in anisotropic interactions which are different for different particle pairings. In consequence, we consider a multi-component system of particles with anisotropic attractive interactions.

We perform overdamped Brownian dynamics simulations in a two-dimensional quadratic simulation box at reduced number density $\rho^* = \rho/\sigma^2$ with N particles of equal diameter σ. The equations of motion are given by

$$\gamma \dot{\mathbf{r}}_i = \sum_{j=1}^{N} \boldsymbol{\nabla}_{\mathbf{r}_{ij}} U(\mathbf{r}_{ij}) + \zeta_i \tag{3.25}$$

where γ is the friction constant and ζ_i is a Gaussian noise vector acting on particle i fulfilling $\langle \zeta_i \rangle = 0$ and $\langle \zeta_i(t) \zeta_j(t') \rangle = 2\gamma T^* \delta_{ij} \delta(t - t')$ with $T^* = k_B T/\epsilon$ being the temperature times Boltzmann's constant in units of ϵ. All simulations are performed at the same constant temperature $T^* = 0.01$. The Eqs. [3.25] are solved via the Euler scheme (see Sec. 6) with an integration step width $\Delta t = 10^{-5} \tau_b$, where τ_b is a Brownian timescale defined by $\tau_b = \sigma^2 \gamma / \epsilon T^*$. In the following the reduced units used in this chapter are summarized.

Tabular representation of reduced units.

reduced density	$\rho^* = \rho\sigma^2 = 0.35$
reduced temperature	$T^* = k_B T/\epsilon = 0.01$
reduced dipole moment	$\mu^* = \mu/\sqrt{\sigma^3 \epsilon}$

3.5 Characterization of Network Structures - Energy Histograms

Under the presence of both, magnetic and electric fields, the superparamagnetic particles described in the previous section form network-like structures as shown in Fig. 1.6. These structures can be thought of as aggregates of basic building blocks, each consisting of a central particle with a specific arrangement of nearest neighbors at distance $\approx \sigma$. In Fig. 3.5 all rectangular and linear configurations with field aligned connection vectors between nearest neighbors are shown. Note that this means that the number of neighbors is restricted, $N_b \leq 4$. These configurations correspond to basic building blocks for chains, end of chains/dimers and junctions (yellow, magenta light blue and black central particle). In the following, a method which allows to identify these building blocks in the experimentally observed colloidal networks is presented. To this end, each particle is associated with two *fictitious* dipole moments $\mathbf{m}^\alpha$ of absolute value $m^\alpha = \sqrt{\epsilon\sigma^3}$ placed in its center. Here ϵ is again an arbitrary unit of energy. One moment points along the electric field ($\alpha = el$), and one along the magnetic field ($\alpha = mg$). Note that these moments are not physical; Being fictitious quantities these moments serve in the following as

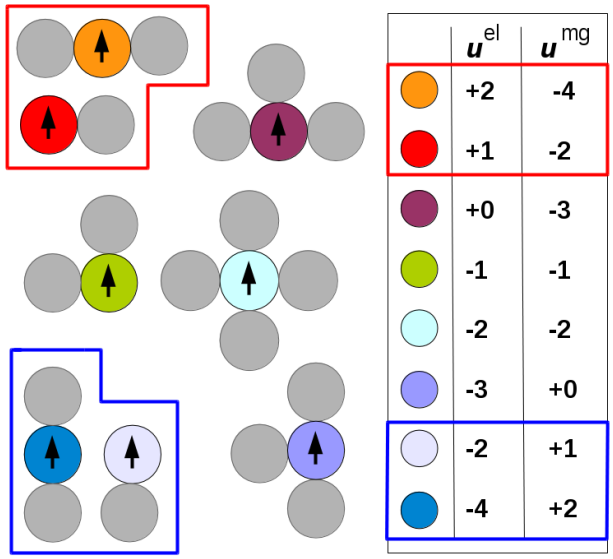

Figure 3.5: Different local arrangements of particles with nearest neighbor distances σ in rectangular network structures and in linear chains. The legend gives the fictitious energies u^{el} (u^{mg}) in units of an arbitrary energy ϵ for particles with dipole strengths $m^\alpha = \sqrt{\epsilon\sigma^3}$. Note that horizontal chains have positive electric energies u^{el} (red frame), while vertical chains have positive magnetic energies u^{mg} (blue frame).

'tools' for structure analysis only. Introducing these moments allows to calculate corresponding *fictitious* electric and magnetic energies between the central particle of a building block, denoted by i, and all its nearest neighbors j via the summed dipole-dipole potential

$$u_i^\alpha = \sum_{j=1}^{N_b} \mathbf{m}_i^\alpha \mathbf{m}_j^\alpha e_{ij}^{-3} - 3(\mathbf{m}_i^\alpha \mathbf{e}_{ij})(\mathbf{m}_j^\alpha \mathbf{e}_{ij}) e_{ij}^{-5} \tag{3.26}$$

with $\mathbf{e}_{ij} = \mathbf{r}_{ij}/r_{ij}$. Hence, each particle i can be associated with two fictitious energy values, the electric one u_i^{el} and the magnetic one u_i^{mg}. Certain energy pairs correspond to certain basic building blocks as it can be seen in in Fig. 3.5. In fact, knowledge of *both* values, u_i^{el} and u_i^{mg}, allows *unique* identification of the building block belonging to particle i: knowledge of one energy contribution is insufficient to distinguish between end of chains (dimers) and junctions (configurations with four neighbors).

Applying this identification scheme to network structures from simulation or experiment requires to define a cut off distance for nearest neighbors, which is chosen here to $r^c = 1.15\sigma$. Because $\sigma \lesssim r^c$ the energies u^α can reasonably be calculated by using the unit distance vector $\mathbf{e}_{ij}$ (see Eq. [3.26]) instead of the true distance. Here we assume that nearest neighbors are (almost) in contact. A certain rectangular network structure is properly characterized by the distributions of the energies u_i^{el} and u_i^{mg}, which means by the distribution of the basic building blocks. In Fig. 3.6(d), the distributions of u_i^{el} and u_i^{mg} are shown for the experimental network given in Fig. 3.6(a) as well as for a network resulting from simulation, which is shown in Fig. 3.6(e). The histograms are normalized by the number of particles in aggregates A. Certain (integer valued) peaks of these distributions correspond to the populations of certain building blocks, which are placed as cartoons beneath these peaks. Closer inspection of Fig. 3.5 shows that both energies are negative or equal zero($u^\alpha \leq 0$ and $u^{\gamma\neq\alpha} \leq 0$) for particles in junctions or more compact structures. In contrast to that, chain-like configurations generally yield positive values of one energy type and negative energies of the other type ($u^\alpha > 0$ and $u^{\gamma\neq\alpha} \leq 0$). In fact, particles in horizontal chains have positive electric interaction energies $u^{el} > 0$, while particles in vertical chains have positive magnetic energies $u^{mg} > 0$. This can also be seen in Fig. 3.6(b), where each particle i is color-coded according to its electric energy u_i^{el}.

Hence it is straight forward to determine the 'role a particle plays'. In the following, particles in horizontal chains ($u^{el} > 0$) are colored in red, particles in vertical chains are colored in blue ($u^{mg} > 0$) and node particles are colored in black ($u^{el} < 0$ and $u^{el} < 0$). Particles without nearest neighbors are indicated by black circles. Applying this identification scheme to the network structure from experiment (Fig. 3.6(a)) results in a re-color coded representation given in Fig. 3.6(c). This scheme works surprisingly well and allows proper identification of horizontal and vertical chains as

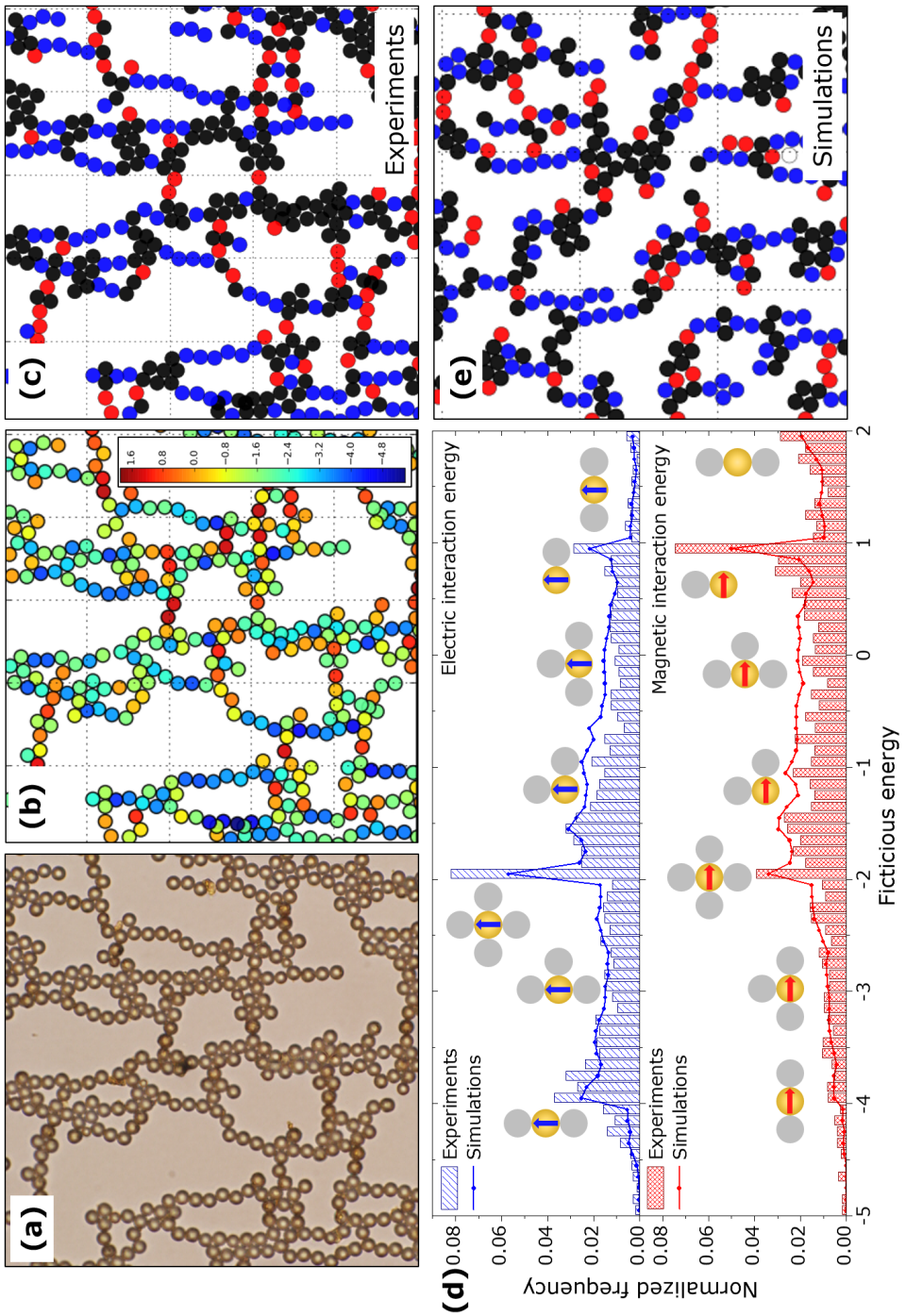

Figure 3.6: Colloidal network in experiment at $E = 37V$ and $H = 3.5V$ and simulation at $\mu^{el} = 0.4$, $\bar{\mu}^{mg} = 0.4$ and density $\rho^* = 0.35$. Experimental microscopic image (a) in natural colors, (b) with particles colored according to the distribution u^{el} and (c) colored according to the 'role' a particle plays in the network. (d) Distributions of u^{el} (blue) and u^{mg} (red) for the experimental structures in (a) and for a simulated network colored according the 'role a particle plays' in (e).

well as nodes or clustered aggregates.

In addition, once the role a particle pays in the aggregate is found, statistics of populations of node or chain particles can be collected. In the following, the number of particles in vertical chains is denoted by v, in horizontal chains by h and in nodes by n. By A we denote the number of particles with at least one neighbor and it holds

$$v + h + n = A. \tag{3.27}$$

3.6 The EDP Model - A Generic Approach towards Mutidirectional Field Induced Dipolar Interactions

In the present section we introduce the extended dipole particle (EDP) model. Our aim is to construct a model which captures essential features of the interactions between colloids in crossed fields. However, we do not claim to model one specific (electric and/or magnetic) system in its details, but rather provide a generic and computationally convenient model. To this end, we consider a two-dimensional system of N soft spheres of equal diameter σ. The soft sphere interactions are repulsive and are modeled by a shifted and truncated (12,6) Lennard-Jones Potential

$$U_{SS}(\mathbf{r}_{ij}) = 4\epsilon\left((\sigma/r_{ij})^{12} - (\sigma/r_{ij})^{6} + 1/4\right) \tag{3.28}$$

which is cut off at $r_{ij}^{c,SS} = 2^{1/6}\sigma$. Here, $r_{ij} = |\mathbf{r}_j - \mathbf{r}_i|$ is the particle center-to-center distance and ϵ sets the unit of energy.

The crossed orthogonal external fields induce orthogonal dipole moments $\boldsymbol{\mu}^m = \mu\mathbf{e}_m$ and $\boldsymbol{\mu}^e = \mu\mathbf{e}_e$, which we term for simplicity as 'magnetic (m)' and 'electric (e)' dipoles (although the model is also appropriate for two electric moments). The coordinate frame is adjusted to coincide with the directions of these moments so that $\mathbf{e}_m = \mathbf{e}_x$ and $\mathbf{e}_e = \mathbf{e}_y$. In general, these moments can have different absolute values, but for simplicity they are assumed to be equal in this preliminarily consideration. The two types of dipole moments are also assumed to be independent from each other, meaning that they interact only with dipole moments of the same type on other particles. The occurrence of rectangular particle arrangements in experiments [25] suggests an effective 'four-fold valency' of pair interactions, irrespective of other details.

Here we want to take into account the four-fold valency but also the overall attractiveness (no repulsion) of the crossed point-dipole setup [see Eq. (3.20)]. We thus introduce, as detailed below, artificial 'dipole moments' composed of charges with short-ranged interactions. Note that the fixed orientation of dipole moments and the overall attractiveness contrasts the 'classical' theoretical concepts of patchy particles [4, 103, 102, 105, 151], which are able to rotate and are characterized by localized attractive and repulsive interactions.

To be specific, each dipole moment $\boldsymbol{\mu}^\alpha$ (with $\alpha = e, m$) is replaced by two opposite charges $-q^{\alpha_1} = q^{\alpha_2}$ which are shifted out of the particle center by a vector $\boldsymbol{\delta}^{\alpha_k} = (-1)^k\delta\boldsymbol{e}_{\boldsymbol{\alpha}}$, with $k = 1, 2$. The vector $\boldsymbol{\delta}^{\alpha_k}$ points either parallel ($k = 2$) or anti-parallel ($k = 1$) along the corresponding point dipole moment $\boldsymbol{\mu}^\alpha$. Independent of their type, all charges have the same absolute value $q = |q^{\alpha_k}| = 2.5(\epsilon/\sigma)^{-1/2}$ and shift $|\boldsymbol{\delta}|$ for the sake of simplicity. In principle though, this 'extended' dipole model allows also to vary the values of q and δ for different interaction types. Also, the choice of the value

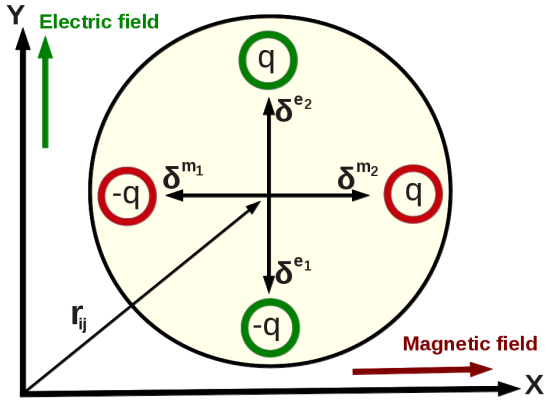

Figure 3.7: Distribution of externally induced fictitious "charges" q inside a particle. Positions of charges are determined by the vectors $\boldsymbol{\delta}^{\alpha_k} \in [-\delta\mathbf{e}_x, \delta\mathbf{e}_x, -\delta\mathbf{e}_y, \delta\mathbf{e}_y]$) pointing either parallel or anti-parallel to the corresponding fields.

$q = 2.5$ is essentially arbitrary, as we will later normalize the interaction energy to eliminate the dependence of its magnitude on the charge separation δ [see Eq. (3.32) below]. A schematic representation of the model with its internal arrangement of 'charges' is shown in Fig. 3.7. Mimicking magnetic dipoles via spatially separated 'charges' is clearly artificial from a physical point of view, but in the spirit of the generic character of our model. Charges k and l on different particles i and j interact via a Yukawa potential

$$U_{ij}^{\alpha_k\alpha_l}(r_{ij}) = -q^2 \frac{exp(-\kappa r_{ij}^{\alpha_k\alpha_l})}{r_{ij}^{\alpha_k\alpha_l}} \tag{3.29}$$

with $r_{ij}^{\alpha_k\alpha_l} = |\mathbf{r}_j - \mathbf{r}_i + \boldsymbol{\delta}^{\alpha_l} - \boldsymbol{\delta}^{\alpha_k}|$. The inverse screening length is chosen to $\kappa = 4.0\sigma^{-1}$ and a radial cutoff $r_c = 4.0\sigma$ is applied, which ensures interaction energies smaller than 10^{-6} at cut-off distance. Using a screened potential between the charges has mostly computational reasons; correct treatment of the true, long-ranged coulomb potential requires specific simulation methods [144]. In the present model the effort is enhanced by the fact that each particle has four charges. Still, the directional dependence of the interactions does not change due to the screening. We also note that previously similar models with comparable interaction ranges have been used to describe dipolar colloids in the framework of discontinuous molecular dynamics simulations [108, 152]. The arrangement of charges inside particles then results in a pair-interaction $U_{DIP}(\mathbf{r}_{ij})$ given

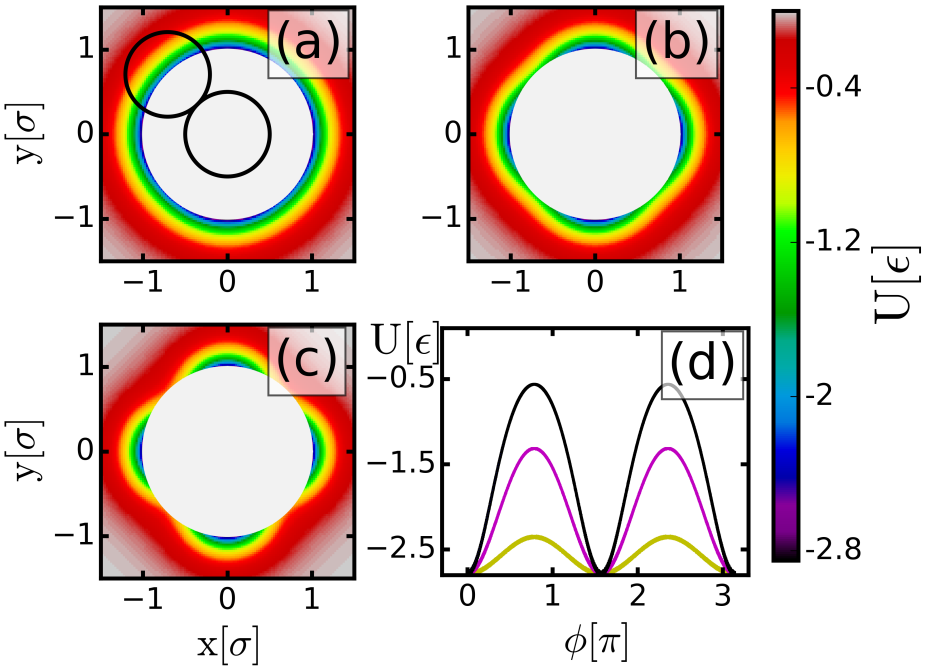

Figure 3.8: Normalized direction-dependent pair interaction $U(\mathbf{r}_{ij})$ [see Eq. (3.34)] between a particle in the center of the coordinate frame and a second particle (indicated as black circle in (a)) at various positions $\mathbf{r}_{ij}$ for three different charge separations $\delta = 0.1, 0.21, 0.3\sigma$ corresponding to (a), (b), (c). Sterically excluded areas are indicated by white circles. (d) Interaction energy at distance $r_{ij} = \sigma$ as function of ϕ, the angle measured in multiples of π against the x-axis, for $\delta = 0.1\sigma$ (yellow), $\delta = 0.21\sigma$ (purple) and $\delta = 0.3\sigma$ (black).

by

$$U_{DIP}(\mathbf{r}_{ij}) = \sum_{k,l=1}^{2} [U_{ij}^{e_k e_l}(\mathbf{r}_{ij}) + U_{ij}^{m_k m_l}(\mathbf{r}_{ij})]. \tag{3.30}$$

In principle, $U_{DIP}(\mathbf{r}_{ij})$ is a function of q and δ. To facilitate the comparison between the interactions at different δ (q is chosen to be constant), we normalize $U_{DIP}(\mathbf{r}_{ij})$ according to

$$\tilde{U}_{DIP}(\mathbf{r}_{ij}) = U_{DIP}(\mathbf{r}_{ij}) \times u / U_{DIP}(\sigma \mathbf{e}_\alpha) \tag{3.31}$$

where the constant $u = -2.804\epsilon$ is calculated from the non-normalized energy $U_{DIP}(\sigma \mathbf{e}_\alpha)$ with model parameters $\delta = 0.3\sigma$ and $q = 2.5(\epsilon/\sigma)^{-1/2}$. This procedure ensures that the normalized energy between two particles at contact ($r_{ij} = \sigma$) and direction $\mathbf{r}_{ij} = \sigma \mathbf{e}_\alpha$ (pointing along one of the fields) has the constant value u for all δ, that is

$$\tilde{U}_{DIP}(\sigma \mathbf{e}_\alpha) = u. \tag{3.32}$$

Therefore we can reformulate the dipolar coupling strength in Eq. [3.7] for this model towards

$$\lambda = u/k_B T. \tag{3.33}$$

The full pair interaction of our model is then given by

$$U(\mathbf{r}_{ij}) = U_{SS}(\mathbf{r}_{ij}) + \tilde{U}_{DIP}(\mathbf{r}_{ij}). \tag{3.34}$$

The resulting potential is illustrated in Fig. 3.8(a)-(c) for a particle in the center of the coordinate frame and a second particle at various distances r_{ij} and angles $\phi = \arccos(\mathbf{r}_{12} \cdot \mathbf{e}_x / r_{12})$ with 'charge' separations $\delta = 0.1, 0.21, 0.3\sigma$. The value $\delta = 0.21\sigma$ is motivated by our simulation results presented in Sec. 5.2.2. Sterically-excluded areas are shown in white and energy values are color coded in units of ϵ. The weak anisotropy of the resulting particle interactions at small δ (where one essentially adds two dipolar potentials, (see Eq. [3.20]) transforms to a patchy-like pattern [103, 102] by increasing δ. Energy minima become more and more locally restricted and interactions reveal an increasing four-fold (i.e., 'patchy') character, although remaining their attractiveness in general. This is also seen in Fig. 3.8(d) which gives the energy between two particles in contact as function of ϕ for different δ. From Fig. 3.8(d) we also see that, independent of the 'charge' separation δ, the minima of the full interaction potential (see Eq. [3.34]) occur for connection vectors $\mathbf{r}_{ij} = \sigma \mathbf{e}_e$ and $\mathbf{r}_{ij} = \sigma \mathbf{e}_m$ (i.e., pointing along the fields). Note that this already holds for the non-normalized energy given in Eq. [3.30].

Tabular representation of reduced units.

reduced density	$\rho^* = \rho\sigma^2$
reduced temperature	$T^* = k_B T/\epsilon$
reduced interaction strength	$u^* = u/\epsilon = -2.804$
Brownian time scale	$\tau_b = \sigma^2 \gamma / k_B T$

Simulations are performed with $N = 1800$ to 3200 particles at a range of reduced number densities $\rho^* = \rho\sigma^2$ and temperatures $T^* = k_B T/\epsilon$, in a square-shaped simulation cell with periodic boundary conditions. The equations of motion

$$\gamma \dot{\mathbf{r}}_i = -\sum_{j=1}^{N} \nabla U(\mathbf{r}_{ij}) + \zeta_i(t) \tag{3.35}$$

are solved via the Euler scheme with an integration step width $\Delta t = 10^{-4}\tau_b$, where $\tau_b = \sigma^2\gamma/k_B T$ is the Brownian timescale, γ is the friction constant and $\zeta_i(t)$ is a Gaussian noise vector which acts on particle i and fulfills the relations $\langle \zeta_i \rangle = 0$ and $\langle \zeta_i(t)\zeta_j(t') \rangle = 2\gamma k_B T \delta_{ij}\delta(t-t')$ [135]. We perform simulations for up to $10^3 \tau_b$.

4

Lane Formation of Dipolar Microswimmers

Using Brownian Dynamics (BD) simulations we investigate the non-equilibrium structure formation of a two-dimensional (2D) binary system of dipolar colloids propelling in opposite directions. Despite of a pronounced tendency for chain formation, the system displays a transition towards a laned state reminiscent of lane formation in systems with isotropic repulsive interactions. However, the anisotropic dipolar interactions induce novel features: First, the lanes have themselves a complex internal structure characterized by chains or clusters. Second, laning occurs only in a window of interaction strengths. We interpret our findings by a phase separation process and simple force balance arguments.

4.1 Background

In the present chapter we present results previously published in [153]. Based on particle-based Brownian Dynamics (BD) simulations, we investigate a prototype of field-propelled complex colloids, that is, spheres with dipolar interactions. Our model is inspired by real systems of metallodielectric "Janus" spheres with two dielectric parts acquiring different (induced) dipole moments in an external electric field [15]. Previous experimental studies in a quasi-two dimensional (2D) setup with an in-plane field have shown that these particles perform straight motion *perpendicular* to the field [55], with two possible directions depending on the orientation of the hemispheres. Ensembles of such particles therefore should

exhibit lane formation, with the additional feature of strongly anisotropic interactions favoring the formation of staggered chains. Based on a suitable model system, we find indeed several new phenomena: First, despite a pronounced tendency to aggregate into chains perpendicular to the driving force, the dipolar interactions can induce laning at densities where purely repulsive systems are mixed. At larger interaction strengths, however, we observe a breakdown of lane formation. Moreover, by comparing the lane formation with that in a much simpler system governed by isotropic, attractive Lennard-Jones (LJ) interactions, we show that the main laning mechanism is, in fact, the effective (angle-averaged) *attraction* between the dipoles. Indeed, for both systems the onset of laning roughly occurs at coupling strengths related to *equilibrium phase separation*. Finally, lanes disappear when the maximum pair attraction corrected by the thermal energy exceeds the work done by the driving force.

Tabular representation of reduced units.

reduced density	$\rho^* = \rho\sigma^2$
reduced driving force	$f_d^* = f_d\sigma/k_BT$
reduced dipole moment	$\mu^* \equiv \mu_i^{(2)^*} = \mu_i^{(2)}/\sqrt{\sigma^3 k_B T}$
reduced LJ coupling strength	$\epsilon^* = \epsilon/k_BT$

Target quantities To quantify the degree of laning along the driving force $\mathbf{f}_{d,i}^s = s_i f_d \mathbf{e}_x$, we introduce for every particle i a slice in x-direction with lateral width σ centered around y_i. We then assign a variable Φ_i which equals 1 if the slice contains no particle of opposite driving direction and 0 otherwise. The ensemble-averaged laning order parameter then follows as

$$\Phi = \langle \sum_{i=1}^{N} \Phi_i/N \rangle, \tag{4.1}$$

where the brackets denote a time average. Non-laned states are characterized by $\Phi \approx 0$ whereas perfectly laned states correspond to $\Phi = 1$. However, the system can visually appear as being laned already at much smaller values of Φ (e.g., $\Phi \approx 0.2$), especially at high densities. To characterize the local structure in x-direction we calculate the radial distribution function between particles of the same type

$$g^s(x) = \frac{2}{\rho N} \langle \sum_{i=1}^{N} \sum_{j \neq i}^{N} \delta(x - |x_{ij}|)\Theta(\sigma - |y_{ij}|)\Theta(s_i s_j) \rangle \tag{4.2}$$

with x_{ij} (y_{ij}) being the x (y)-component of $\mathbf{r}_{ij}$, and δ and Θ are the delta- and the Heavyside step function, respectively. By normalization, $g^s(x)$ decays to 2 for $x \to \infty$ in a single-species fluid and to 1 in a completely mixed binary fluid. By interchanging x and y in Eq. (4.2) we additionally define the correlation function $g^s(y)$ in y-direction.

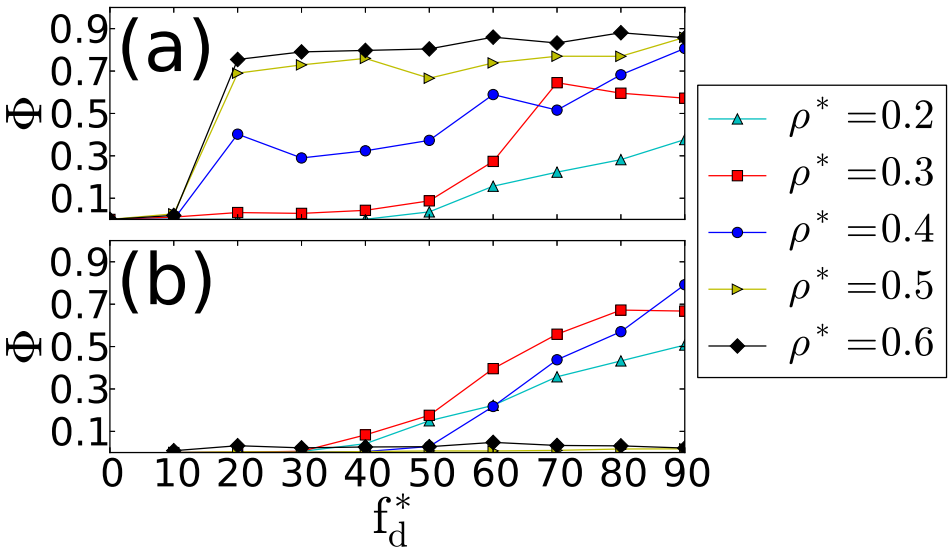

Figure 4.1: Laning order parameter as function of driving force for (a) the DDP system ($\mu^* = 1.58$) and (b) the SS system ($\epsilon^*_{SS} = 10 k_B T$) at different densities.

4.2 Lane Formation of Dipolar Microswimmers

In Fig. 4.1(a) we plot the laning order parameter Φ of DDP systems for different densities $\rho^* = \rho\sigma^2$ as functions of the dimensionless driving force $f_d^* = f_d \sigma / k_B T$. At low driving forces ($f_d^* \leq 10$) the order parameter is essentially zero for all densities considered, reflecting the absence of lanes. The corresponding local structure at $f_d^* = 0$ and $\rho^* = 0.2$ is illustrated by the simulation snapshot shown in Fig. 4.2(a). One observes the formation of 'staggered' chains, consistent with the most attractive pair configurations illustrated in Fig. 3.2(b), and in qualitative agreement with experiments of metallo-dielectric particles under field conditions where self-propulsion is absent [15]. At very small driving forces ($f_d^* < 10$) staggered chains are driven against each other and form one large aggregate consisting of both species. This corresponds to a jammed state.

Increasing f_d^* to larger values, all of the systems considered in Fig. 4.1(a) display laned 'states' characterized by non-negligible values of Φ. For small densities ($\rho^* < 0.4$) this lane formation occurs gradually and significant values of Φ are reached only at high driving forces $f_d^* > 50$. In contrast, dense systems display a rather steep laning "transition" at a driving force $f_d^* \approx 15$. A visualization of exemplary laned states at $f_d^* = 80$ and two densities is given in fig. 4.2(b) and (c). Here, the driving force $\mathbf{f}^s_{d,i} = s_i f_d \mathbf{e}_x$ points horizontally either to the left, for 'yellow' particles ($s_i = -1$) or to the right for 'purple' particles ($s_i = 1$). To elucidate the impact of dipolar forces on the functions $\Phi(f_d^*)$ we plot in Fig. 4.1(b) corresponding data for the driven SS system. At low densities $\rho^* \leq 0.4$ the systems behave similar

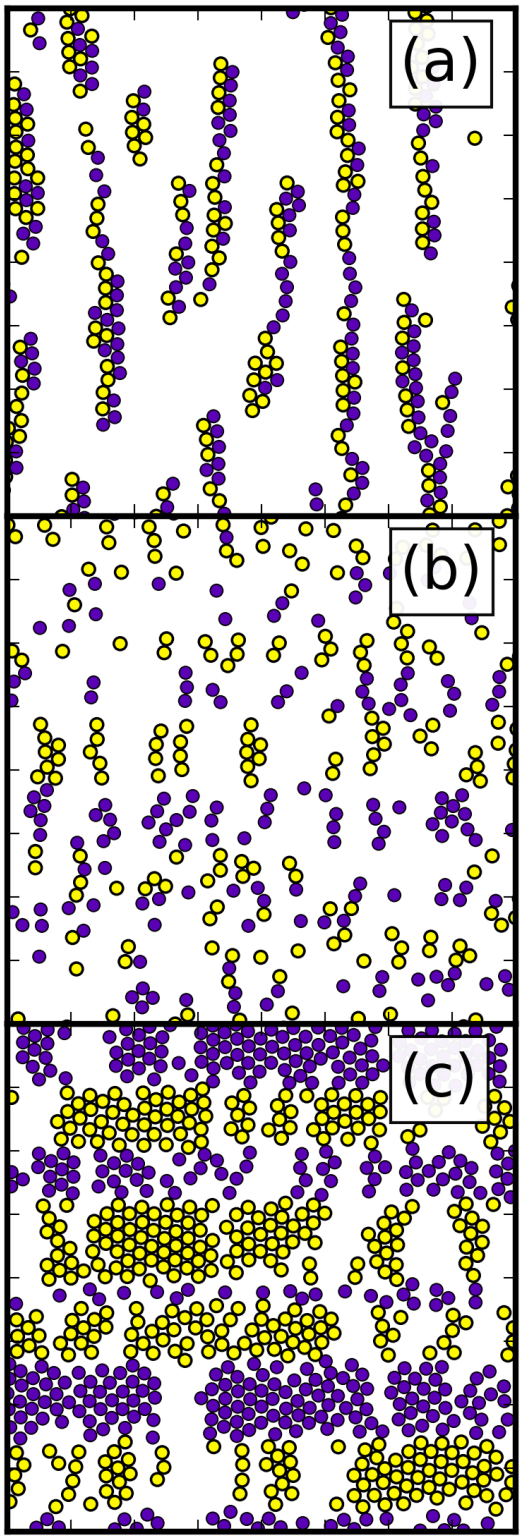

Figure 4.2: Snapshots of the DDP system in the x-y plane at (a) $f_d^* = 0$, $\rho^* = 0.2$, (b) $f_d^* = 80$, $\rho^* = 0.2$ ($\Phi \approx 0.2$) and (c) $f_d^* = 80$, $\rho^* = 0.5$ ($\Phi \approx 0.75$). The driving force acts horizontally to the right (left) on dark (bright) particles: $s = 1$ (-1), $\mu^* = 1.58$.

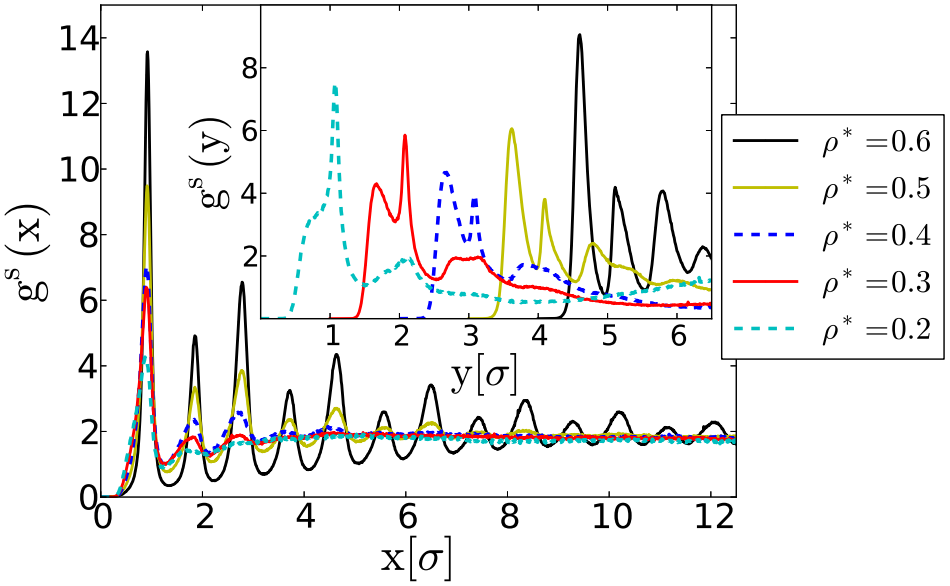

Figure 4.3: Pair correlation functions between double dipolar particles of the same species along the x-direction (main plot) and the y-direction (inset). The data pertain to $f_d^* = 80$ and different densities. In the inset, curves for different densities have been shifted by one σ to enhance visibility.

to their DDP counterparts. However, at high densities ($\rho^* > 0.4$) there is *no* lane formation in the (purely repulsive) SS system, in striking contrast to the behavior of the DDP systems. We will come back to this point below. Here we first consider the internal structure of the lanes in the DDP systems.

4.2.1 Complex lanes - Internal structure

Visual inspection of Figs. 4.2(b) and (c) suggests that lanes consist of clusters of particles of the same type.

At low densities (see Fig. 4.2(b)) we find mostly short chains oriented in y-direction, which reminds of the equilibrium structure of single dipole particles in external fields [22]. Clearly, such chains are absent in simpler (isotropic) lane-forming systems. At higher densities (see Fig. 4.2(c)) the particles tend to form clusters along the driving force but the local arrangement is not crystalline in the sense of i.e., a hexagonal Bravais lattice. However, the corresponding (hexagonal) translational order parameter [65] (see Eq [5.5]) is larger than that observed at low f_d^*.

For a more quantitative characterization we consider the correlation functions $g^s(y)$ and $g^s(x)$ plotted in Fig. 4.3 at a high driving force $f_d^* = 80$ and at different densities $\rho^* \in [0.2, 0.6]$. For the lowest density considered ($\rho^* = 0.2$) $g^s(y)$ reveals a pronounced peak at $y = 1\sigma$ and a second, smaller

one at $y = 2\sigma$, indicating chains of up to three particles along the field direction. Furthermore, we observe a 'hump' appearing directly before the first peak. This 'hump' results from bended and perturbed chains as well as from a few clusters elongated in x-direction (see Fig. 4.2(b)). Increasing the density the hump transforms into a pronounced peak, which finally overtakes the peak at $y = 1\sigma$ at $\rho^* = 0.4$. At this density, linear chains in y-direction have lost their dominance as structural elements. Instead, clusters spread out in x-direction.

This interpretation is supported by the behavior of the function $g^s(x)$ which displays a similar qualitative change at $\rho^* = 0.4$. At densities $\rho^* \leq 0.3$, $g^s(x)$ reveals only one relatively small peak at a distance of $x = 1\sigma$ showing that a minor fraction of chains is bended, staggered or has additional particles attached in x-direction. Increasing ρ^* results in an increase of this first peak and the emergence of a second peak at $x \approx 2\sigma$. Again this peak reaches relevant values (> 2) for $\rho^* = 0.4$ and indicates thereby cluster growth in x-direction and finally a change from linear chains in y-direction to horizontally elongated clusters. At even higher density $\rho^* = 0.5, 0.6$ elongation of clusters in x-direction becomes comparable to the system size.

We conclude that there are two qualitatively different regimes for lane formation in the DDP-system. The first one (chain regime) is characterized by short chain-like aggregates inside lanes and occurs for relatively high driving forces $f_d^* > 50$ and low densities $\rho^* \leq 0.3$. These parameters are comparable to the parameters under which lane formation is observable in the HS-model and SS-model (see Fig. 4.1(b) and [91, 80]). The second one (cluster regime) is characterized by in x-direction elongated clusters arranged in lanes and is restricted to larger densities $\rho^* > 0.4$. A similar intra lane structure has been reported by Menzel in [89] for a confined two-dimensional setup of active particles with an alignment mechanism. However, once the density is larger than 0.4 and $f_d^* > 20$, the degree of lane formation is more or less independent of ρ^* and f_d^*. The fact that at very small driving forces the system undergoes a transition towards a laned state for all densities $\rho^* > 0.3$ at the same driving force is qualitatively different to the reentrant behavior of the HS-model [91].

We note that these structural details are quite sensitive to the shift parameter δ characterizing the position of the dipole moments inside the particles: Indeed, as revealed by test simulations, smaller values of δ tend to suppress the lane formation in the "chaining regime" and enhance the occurrence of chains in the "cluster regime".

4.2.2 Complex lanes - Characteristic lane widths

The fact that lanes in the DDP-system reveal certain internal structures, raises the question whether these internal structures translate into *characteristic* lane widths.

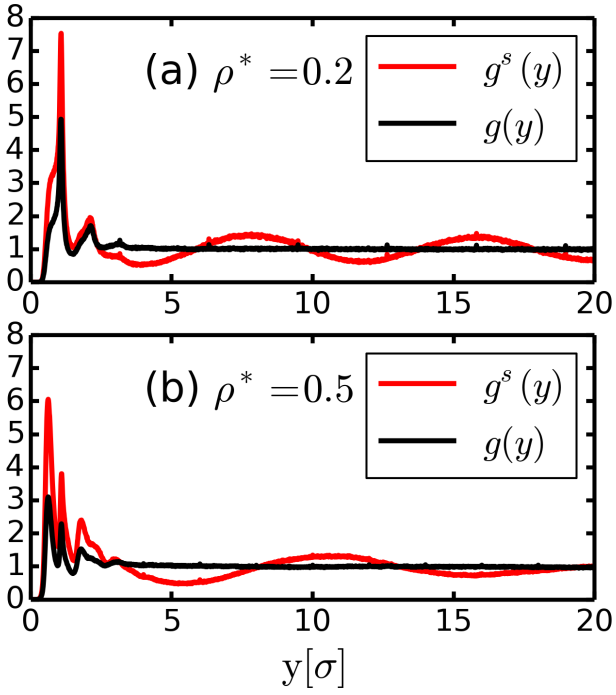

Figure 4.4: Pair-correlation functions , $g(y)$ (black) and $g^s(y)$ (red), of the double dipolar system in y-direction for laned states at densities $\rho^* = 0.2$ (a) and $\rho^* = 0.5$ (b) and common driving force $f_d^* = 80$.

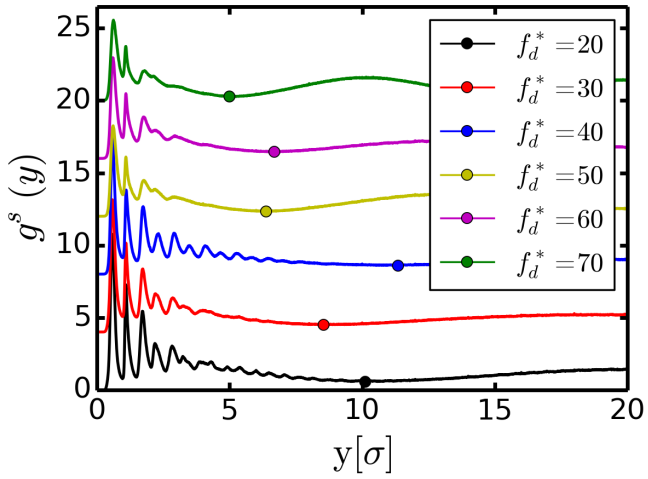

Figure 4.5: Pair-correlation functions $g^s(y)$ in y-direction for laned states of the DDP-Model at density $\rho^* = 0.5$ and various driving forces $f_d^* \in [10, 70]$. First 'long-ranged' minima of $g^s(y)$ are indicated by dots. The different functions $g^s(y)$ are subsequently shifted by 4σ in vertical direction for better illustration.

To answer this question we show in Fig. 4.4 (a) and (b) the particle type specific pair distribution functions in y-direction $g^s(y)$ as well as the usual pair distribution function in y-direction $g(y)$ at $f_d^* = 80$ for the two densities $\rho^* = 0.2, 0.5$, corresponding to the snapshots in Fig.4.2 (b) and (c). The presence of particle type specific lanes is reflected in the long-range oscillation of $g^s(y \geq 5\sigma)$ whereas the periodicity corresponds roughly to the widths of lanes. In contrast to that, the pair distribution function in y-direction $g(y)$ yields no long-ranged oscillations because it can not distinguish between particle species and particle type specific lanes. In consequence, the position of the first minimum of $g^s(y \geq 5\sigma)$ can be used to estimate an averaged lane width.

In Fig. 4.5 we show $g^s(y)$ for the intermediate density $\rho^* = 0.5$ at different driving forces whereas all of these cases represent laned states. The first long-ranged minima of $g^s(y)$ is indicated by a dot. The different functions $g^s(y)$ are subsequently shifted by 4σ in vertical direction for better illustration. Clearly, a tendency to form thinner lanes at higher driving forces can be observed ranging from 10σ at the lowest driving force to 5σ at the highest driving force (see also Fig. 4.4(b) for the first minima of $g^*s(y)$ at $f_d^* = 80$.). Only, the minima for $f_d^* = 40$ does not fit properly to this trend which might be the case because of too short simulation times.

Interestingly, also the local structure varies with the strength of the driving force. While at low driving forces there exist up to five peaks in $g^*s(y)$ this reduces to two or three peaks at the higher driving forces. This means, that aggregates forming the 'backbone' of the lane become smaller (in y-direction) in the same way as lanes themselves become thinner. Also the absolute peak heights decrease with f_d^*. In analogy to the how melting process of a solid by increasing temperature it appears here that the internal structure of lanes 'melt' by increasing the drive.

However, results are subject to large statistical variations and the functional form of the dependency of the lane width on the driving force remains unclear. Importantly, test simulations with a fully phase separated initial state consisting of two homogenous lanes revealed that these states are stable, at least for $f_d^* > 20$. Therefore, the lane width depends not only on the driving force but also on the initial conditions. As we are considering a non-equilibrium system here it is not surprising that the system can be trapped in several meta-stable states depending on the initial conditions. Also the exceptional behavior of $g^*s(y)$ at $f_d^* = 40$ in Fig. 4.5 might result from such meta-stable initial conditions.

Therefore it remains an open question whether there exist characteristic lane widths (in the DDP-system). Previous work on lane-formation in solely repulsive systems did also not report on characteristic lane widths. To our best knowledge there is only Liu et. al.[93] who briefly states that at very high densities $\rho^* \approx 1$ of repulsive spheres there occurs a full separation of particle species into two lanes, which corresponds to a lane width of half the system size. Therefore we shortly want to comment on these

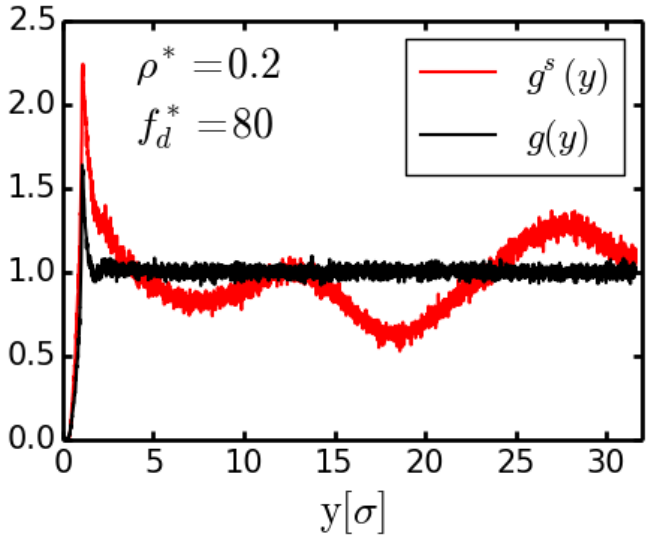

Figure 4.6: Pair-correlation functions in y-direction, $g(y)$ (black) and $g^s(y)$ (red), for a laned state of the SS-Model at density $\rho^* = 0.2$ and driving force $f_d^* = 80$.

solely repulsive HS- and SS-models.

The particle type specific pair correlation function in y-direction $g^s(y)$ for a laned state of the SS-model at $\rho^* = 0.2$ and $f_d^* = 80$ is shown in Fig. 4.6. In the SS-system particles are organized in lanes, but not in clusters. This can be seen by the fact that there is no local structure inside lanes but only one peak ($y \approx 1\sigma$) of $g^s(y)$ for distances smaller than the *actual* lane width ($\approx 6\sigma$ in Fig. 4.6). Furthermore, $g^s(y)$ shows a less regular long-range order than in the DDP system (see Fig. 4.4(a)). Importantly, this lack of clear periodicity of $g^s(y)$ contrasts the idea of a characteristic lane width in SS-systems. At low densities ($\rho^* \in [0.2, 0.4]$), we find that states with a clear periodicity of $g^s(y)$ do not occur systematically. This means that, under fixed conditions (f_d^*, T^*, ρ^*), lanes have significantly different widths inside and between different simulation runs.

In the DDP-system, aggregates are assumed to form (due to their own rigidity) supportive intra lane structures, similar to a backbone. In contrast to that, the SS-system reveals no aggregation, which might reduce its capability to pertain certain lane widths. At least, the presence of such structures is a major difference between lanes in the SS-model and in the DDP-model.

4.3 Mechanisms of Lane Formation

In the following we concentrate on the question *why* the dipolar interactions strongly enhance lane formation compared to the purely repulsive

SS model, as revealed by the order parameter plots in Fig. 4.1. We concentrate on the density $\rho^* = 0.5$, where the differences are particularly pronounced.

4.3.1 Lane formation in the isotropic model

To understand the role of the *effective* attraction in our DDP system on the lane formation we therefore consider, as a first step, the corresponding behavior of a LJ fluid. For simplicity, we choose the same attraction strength ϵ^* for both, different and same species. Results for the order parameter Φ of a driven LJ system as function of ϵ^* at fixed f_d^* are shown in Fig. 4.7(a). For very small values of ϵ^* the order parameter is negligible, consistent with the behavior of the pure SS system in Fig. 4.1(b). Upon increase of ϵ^*, lanes first appear at a certain value and then *disappear* again at a substantially larger coupling. A similar *reentrance* of the non-laned (mixed) state occurs at other driving forces, as seen from the laning "state diagram" (for $\rho^* = 0.5$) presented in Fig. 4.7(b). The state diagram moreover reveals that the *onset* of lane formation occurs at a coupling strength of $\epsilon^* \approx 2.5$ (see dotted green lines in figs. 4.7(a)-(b)) quite independent of f_d^* (taking the value $\Phi = 0.02$ as a lower limit for laning), while the coupling related to the disappearance of lanes appears to be a *linear* function of f_d^*. Given the lower boundary $\epsilon^* \approx 2.5$, it is interesting to make a connection to the *equilibrium* phase diagram of the 2D LJ fluid: This system has a critical point (gas-liquid condensation) at $\rho_c^* = 0.35$ and $T_c^* \approx 0.46$, corresponding to a critical coupling strength $\epsilon_c^* \approx 2.17$ [154, 155]. The triple point (gas-liquid-solid) coupling strength is given as $\epsilon_t^* \approx 2.5$ (with corresponding liquid density $\rho_t^{liquid} \gtrsim 0.6$ [154]). From this we can conclude that the non-driven LJ system at $\rho^* = 0.5$ and $\epsilon^* = 2.5$ is in a strongly correlated state which is, in fact, thermodynamically unstable, i.e., it lies *within* the coexistence curve of the gas-liquid transition. Moreover, revisiting again Fig. 4.7(a)-(b) we see that ϵ_c provides a lower limit of laning. These observations suggest that the equilibrium phase separation is a *prerequisite* for lane formation in the driven LJ system.

We now turn to the breakdown of laning at large coupling strengths. Here, the external force driving two unlike particles ($s_i \neq s_j$) away from one another competes with the attractive LJ forces.

To quantify this competition we construct an *effective* pair interaction $U_{eff}^{LJ}(x_{ij})$ between unlike particles, which are initially in contact and then driven apart in x-direction. A schematic sketch of this setup is shown in Fig. 4.8. In this configuration particles are initially in contact ($|\mathbf{r}_{12}| = \sigma$) but displaced in y-direction. To account for different vertical positions y_{ij}, we first average the x-component of the LJ force

$$F_{LJ,x} = -\partial_{x_i} U_{LJ} \tag{4.3}$$

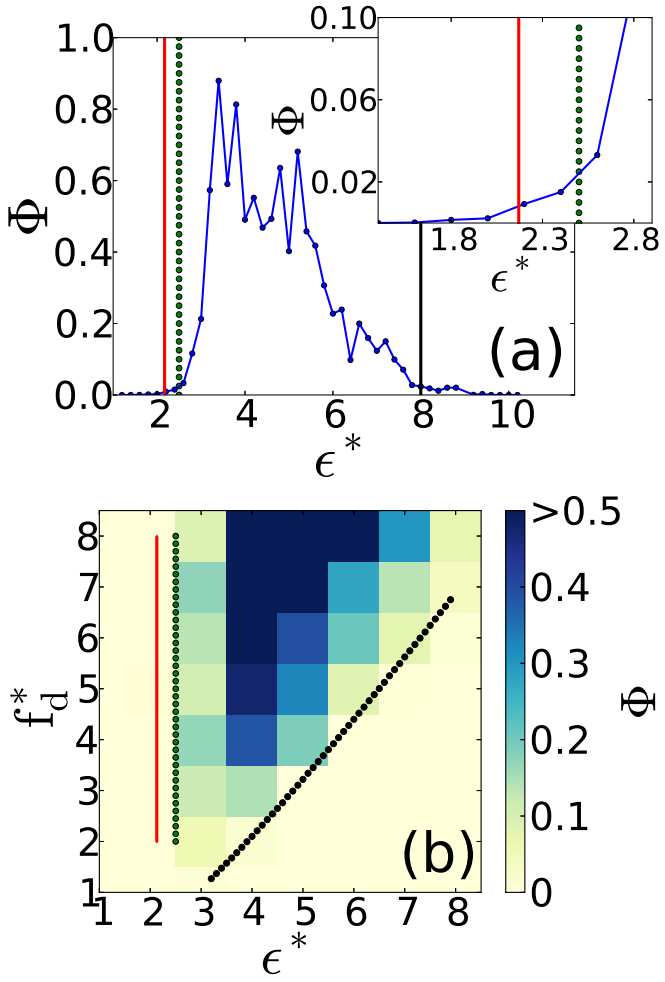

Figure 4.7: (a) Laning parameter versus coupling strength for the LJ system at $f_d^* = 7$, $\rho^* = 0.5$. Inset: Enlarged view for small ϵ^*. (b) Laning "state diagram" of the LJ system. In (a) and (b), red, dotted green and black lines correspond to ϵ_c^*, ϵ_t^*, and ϵ_{max}^*, respectively.

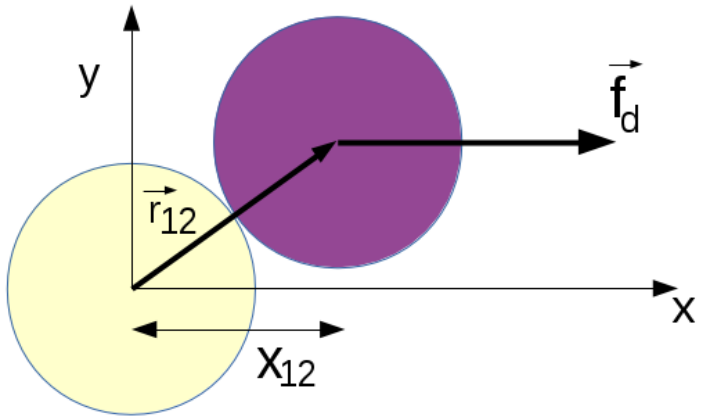

Figure 4.8: Schematic sketch for a yellow particle moving to the left and a purple particle moving to the right. In this configuration particles are initially in contact ($|\mathbf{r}_{12}| = \sigma$) but displaced in y-direction.

, over the angle ϕ between $\mathbf{r}_{ij}$ and $\mathbf{e}_y$ (at fixed distance) yielding

$$\bar{F}_{LJ,x} = \pi^{-1} \int_0^{\pi} \sin\phi F_{LJ} d\phi = 2F_{LJ}/\pi \tag{4.4}$$

with $F_{LJ} = -\partial_r U^{LJ}$. Integration (setting now $y_{ij} = 0$) yields the potential

$$\bar{U}_{LJ}(x_{ij}) = 2/\pi U_{LJ}(x_{ij}) \tag{4.5}$$

. Adding the linear potential associated to the external force yields

$$U^{LJ}_{eff}(x_{ij}) = \bar{U}_{LJ}(x_{ij}) - f_d x_{ij} \tag{4.6}$$

. For small driving forces, U^{LJ}_{eff} displays a local minimum U_{min} and maximum U_{max}, and thus a potential barrier $\Delta U = |U_{max} - U_{min}|$ as shown in Fig. 4.9. Unlike particles tend to stick together (against the drive) if the mean kinetic energy per particle $2 \times k_B T/2$ is smaller than $\Delta U(f_d, \epsilon)$. Solving numerically the equation $\Delta U = k_B T$ for various f_d^* we obtain values $\epsilon^*_{max}(f_d^*)$ indicated by the dotted black line in Fig. 4.7(b). Clearly, our simplified model describes the breakdown of lane formation very well. Moreover, having introduced U^{LJ}_{eff}, we can also understand the fact that the onset of laning occurs at coupling strength slightly larger than the critical coupling in equilibrium, ϵ_c. The driving force effectively reduces the attraction between unlike particles, yielding a shift of phase separation. A similar effect of a shifted onset of phase separation induced by activity has recently been described by Schwarz-Linek et. al. [69] for swimming bacteria in polymer suspensions.

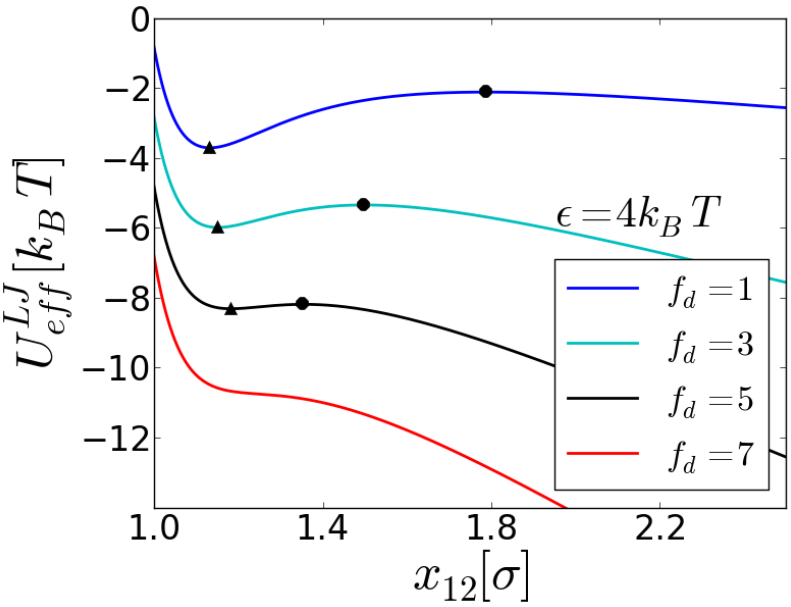

Figure 4.9: Effective interaction at different driving forces f_d^* for the LJ-system. The LJ-interaction strength is chosen to $\epsilon = 4k_BT$ and minima and maxima of the potential barrier opposing lane formation are indicated by triangles and dots.

4.3.2 The laning state diagram for dipolar swimmers

Given this background, we now consider in Fig. 4.7(c) the state diagram of the full, anisotropic DDP fluid ($\rho^* = 0.5$) in the parameter plane spanned by driving force and coupling strength. The latter is now given by μ^* (the soft-sphere repulsion is fixed). Clearly, the structure of the state diagram resembles that of the LJ system. In particular, the onset of laning depends only weakly on f_d^*, and there is an upper boundary for μ^* beyond which laning disappears.

This prompts the question whether the onset of laning in the driven DDP system can be related to an equilibrium fluid-fluid phase separation, as in the LJ system. We note that already the equilibrium DDP system is a true binary mixture, since the full pair interactions depend on s_i, see Fig. 3.2. Therefore the possible fluid-fluid transitions (if existent at all) are, in general, combinations of condensation and demixing. In the present study we did not carry out simulations to explore these questions properly. Still, one can perform some estimates based on mean-field density functional theory (DFT). We focus on the occurrence of condensation (rather than demixing), because the angle-averaged (i.e. mean-field) interaction between unlike DDPs is nearly the same as that between like particles (see Fig. 3.3). The corresponding stability condition of the homogeneous, mixed phase is that the isothermal compressibility, χ_T, has

to be positive. According to Kirkwood-Buff theory [156] one has (for a symmetric binary mixture composed of species A and B)

$$\chi_T^{-1} \propto 1 - (\rho/2)(\tilde{c}_{AA}(0) + \tilde{c}_{AB}(0)) \tag{4.7}$$

, where $\tilde{c}_{AA(AB)}(0)$ are the Fourier transforms of the direct correlation functions (DCFs) $c_{AA(AB)}(\mathbf{r}_{12})$ in the limit of long-wavelengths ($k \to 0$). In our case, AA (AB) corresponds to $s_1 = s_2$ ($s_1 = -s_2$). Furthermore, we approximate the DCFs according to a random phase approximation, that is,

$$c_{s_1 s_2}(\mathbf{r}_{12}) = c_{HS}(r_{12})\theta(\sigma - r_{12}) - (k_B T)^{-1} U_{DD}(\mathbf{r}_{12}, s_1, s_2)\theta(r_{12} - \sigma) \tag{4.8}$$

, where c_{HS} is the Percus-Yevick DCF of a pure hard-sphere fluid [139]. The Fourier transforms of the second, mean-field like contribution to the DCFs yield essentially the spatial integral over the effective potentials defined in Eq. (3.14). Numerical investigation of the resulting expression for χ_T at $\rho^* = 0.5$ reveals that, upon increasing μ^* from zero (where χ_T reduces to the hard-sphere compressibility), χ_T becomes indeed negative at $\mu_s^* = 1.31$, indicating an instability ("spinodal point") related to condensation. Thus, simple mean-field DFT predicts the existence of a condensation transition in the equilibrium DDP fluid. Further, for $\rho^* = 0.5$, the transition should occur at a coexistence value $\mu_{coex}^* \lesssim \mu_s^*$; its actual value is, however, more elaborate to determine. BD test simulations of the non-driven system at $\rho^* = 0.5$ and dipole moments larger than μ_s^* reveal indeed a phase separated structure consisting of thick columns (involving both particle species) and large voids in between. The question now is, does μ_s^* play a decisive role for the *driven* DDP system? Considering Fig. 4.10 we find that μ_s^* (indicated by a white line) yields indeed a good estimate for the onset of laning at low values of the driving force ($f_d^* \lesssim 30$). This suggests that, similar to the LJ system, equilibrium phase separation is a prerequisite of laning at the density considered. Only for larger driving forces ($f_d^* \gtrsim 30$) the estimate worsens (this effect was not observed in the LJ system where, however, calculations where restricted to small f_d^*).

The breakdown of laning at large μ^* can be estimated, similar to the LJ system, by constructing an one-dimensional (x-dependent) potential, in which the DDP interaction between unlike particles competes with the driving force. We consider exemplary configurations $y_{ij} = y_0$ (a simple force average over different configurations y_{ij} is not appropriate due to the interaction anisotropy) and obtain the potential

$$U_{eff}^{DDP}(x_{ij}) = U_{DDP}(x; y_0) - f_d x_{ij} \tag{4.9}$$

which displays a barrier $\Delta U(y_0, f_d, \mu)$. Figure 4.10 includes the numerical solution $\mu_{max}^*(f_d^*)$ (dotted red line) of the equation $\Delta U = k_B T$ at $y_0 = 0.645\sigma$, corresponding to the most attractive, "staggered" configuration at contact (see Fig. 3.2(b)). Clearly, this line describes the breakdown qualitatively, but overestimates the influence of attraction. Quantitatively better

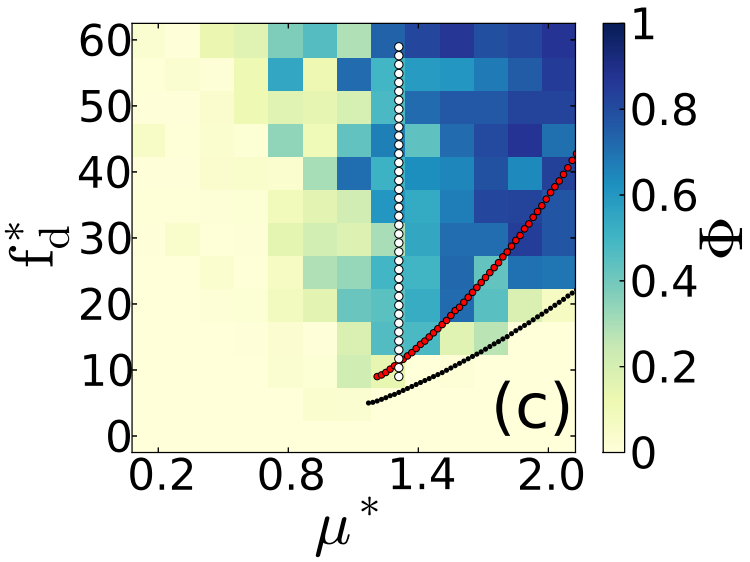

Figure 4.10: State diagram for lane formation in the DDP system. The dotted white line indicates the spinodal 'dipole strength' μ_s^*. Red and black lines indicate the breakdown condition for lane formation with $\mu_{max}^*(f_d^*)$ at $y_0 = 0.645(0.9)\sigma$, framing the true breakdown of lane formation.

results are obtained with $y_0 = 0.9\sigma$ (dotted black line in Fig. 4.10, corresponding to a less attractive initial configuration. The "true" potential should be seen as a (weighted) average over different y_0. Interestingly, the reduction of attraction expressed in the effective potential also explains the shift of the onset of laning with larger f_d^*.

Finally, we briefly want to comment on how the parameter combinations (f_d^*, μ^*) and the associated complex phase behavior (onset and breakdown of lane formation) discussed here relate to experimentally accessible combinations of swimming speed v and external field strength E_{ext}. This is important because the swimming speed v of the particles is proportional to E_{ext}^2 and therefore it is also proportional to the strength of the dipolar interactions (see Eq. [1.1] and the discussion below in Sec. 1.2.4). Hence, the quantities f_d^* and μ^* are not independent for a given particle type. In fact, it holds $f_d \propto \mu^2$. Thus, the accessible state points and the corresponding laning behavior are in principle given by a parabola in the state diagram shown in Fig. 4.10. Hence, it remains an open question whether the onset and/or breakdown of lane formation can be observed in experiment, as this parabola may remain inside or outside the region of lane formation. The answer to this latter question will of course strongly depend on the different parameters, e.g., permittivity and viscosity of the fluid, or particle diameter, relating the strength of the external field with the strength of the dipole moment and the swimming velocity.

4.4 Summary

In the present section we investigated a system of colloidal microswimmers under the presence of an external electric field. The experimental setup motivating this work has been introduced in Sec. 1.2.4. The complex model used for this study is a double dipolar Janus particle with two induced dipole moments of different strengths and an orientationally fixed propulsion direction (see Sec. 3.2). In a two-dimensional setup this means that the system is effectively binary; there exist two particle species with opposite orientations and propulsion directions. Such configurations are generally assumed to undergo lane formation if the propulsion force is strong enough. We have shown that this is indeed the case for our dipolar model and that the induced dipolar interactions stabilize the formation of lanes over a wide range of interaction strengths. This is surprising, as the anisotropic interactions show a strong tendency of the particles to self-assemble into chains which, in the present model, are oriented *perpendicular* to the force. These self-assembly processes result in complex staggered chains, when no driving force is present and the observed structures are in qualitative agreement with experimental observations. The underlying mechanisms for lane formation were then identified by investigating a simple binary Lennard-Jones fluid with oppositely driven particle species. Here, the onset of lane formation is closely related to the phase separation of the corresponding , well known, equilibrium system. By simple theoretical considerations we could also estimate the spinodal point in the double dipole model and show that the same connection is present there. Importantly, the (effective) attractiveness of the particle interactions in both models enables the system to undergo lane formation at propulsion speeds approximately one order of magnitude smaller than in previously known systems. In addition, the presence of attractive interactions can also suppress lane formation. Using force balance arguments, the breakdown of lane formation due to 'freezing' was estimated in very good agreement with the simulation results.

5

Mutidirectional Colloidal Assembly

In this chapter, we are particularly interested in the field directed aggregation of complex dipolar colloids into chain and network structures. To this end we consider particles with two different kinds of dipolar interactions caused by *crossed* (orthogonal) fields. Based on a complex double dipolar model we establish a quantitative comparison between simulation and experiment and a theoretical state diagram for different field conditions.
Furthermore, a detailed analysis of a generic model with a tunable anisotropy of the pair interactions reveals a transition in the systems aggregation behavior from an *anisotropic* DLA regime towards a *slippery* DLA regime by decreasing the anisotropy. The latter transition is accompanied by a strange compactifaction phenomena, which we also find for the more complex model. Hence, it is the non-equilibrium assembly of *transient* aggregates which is investigated here.

Outline

A previously studied example for network forming systems is the metallo-dielectric Janus particles under the presence of an uni-axial electric field inducing dipolar interactions [26, 95]. These structures are shown and discussed in Fig. 1.3(c) and Sec. 1.2.4. In Chapter 4 we investigated the collective behavior of these particles in the swimmer regime.

In this Chapter we are also interested in field directed network formation but investigate a different setup of superparamagnetic particles in

crossed magnetic and electric fields (see Sec. 1.3.3). The results presented in the first Section (Sec. 5.1) of this Chapter are part of a dominantly experimental study and are based on the model presented in Sec. 3.4. Hence, this section has a strong emphasis on the comparison between simulated structures and experimental ones. To this end, a simple method which allows to determine the 'role' a particle plays in the observed networks (see Sec. 3.5) is applied. This method can be used for experimental as well as simulation data and is based on the fundamental symmetries of the point-dipole potential. The overall aim is to provide a theoretical non-equilibrium state diagram for different field configurations at constant density, because this is not achievable from the experimental side.

The second section (Sec. 5.2) of this Chapter is a purely theoretical study of the generic model introduced in Sec. 3.6. In principle, this section allows a connection to network formation of the metallo dielectric Janus particles, but here we focus on conceptional aspects of the aggregation process for the crossed dipole setup. We identify different diffusion limited aggregation regimes and connect them to the anisotropy of the interactions. Finally we discuss connections in the aggregation and compactifaction behavior between the generic and the complex model (see Sec. 5.3).

5.1 Field Controlled Assembly of Colloidal Networks - Experiment and Simulation

Using Brownian dynamics simulation we investigate the aggregation behavior of superparamagnetic polymer particle under the presence of crossed magnetic and electric fields. The concurrent application of electric and magnetic fields is an unusual method to organize colloids into bidirectional chains and clusters. We find that the morphology of the assembled structures in bi-axial fields is highly depend on the number density of particles and their initial spatial distribution. However, in experiments, the number density of the assembling particles is subject to stochastic variations between different samples. In the present study, computer simulations allow us to overcome this difficulty and investigate the state of assembly at a given time with a precise control over the particle density. Hence, we are able to construct a theoretical non-equilibrium state diagram of the assembled morphologies under various field configurations.

5.1.1 Background

The experimental data and photographs presented in this section have been produced by Dr. Bhuvnesh Bharti in the group of Prof. Dr. Orlin D. Velev at the North Carolina state university. Theoretical calculations and evaluation of simulated and experimental data were done by my self. This Section is based on the double dipolar model for superparamagnetic particles in crossed external fields (CDP model) introduced in Sec. 3.4. Externally induced dipolar interactions are model by two decoupled point dipoles, whereas the magnetic dipole moment is shifted out of the particle center in a random direction. The overall aim is to establish a close connection between the experimental observations and simulation results and to provide a theoretical non-equilibrium state diagram for different field configurations. The latter is done by means of extensive Brownian dynamics simulations at constant temperature $T^* = 0.01$ and density $\rho^* = 0.35$ but at various dipole strengths corresponding to dipolar coupling strengths $\lambda \in [0, 50]$. The rest of this section is organized as follows: First, experimental observations are described. Then, a detailed comparison of quantitatively comparable structures in simulation and experiment is performed. Finally, the full field controlled state diagram is presented, and analyzed. The section ends with concluding remarks.

Tabular representation of reduced units.

reduced dipole moment	$\mu^* \equiv \mu_i^{(2)^*} = \mu_i^{(2)}/\sqrt{\sigma^3\epsilon}$
reduced density	$\rho^* = \rho\sigma^2$
reduced temperature	$T^* = k_B T/\epsilon = 0.01$

5.1.2 Structure formation in experiment

In experiments we find that at very low electric and/or magnetic field strengths, the thermal energy in the system overcomes the dipolar interaction energy and restricts the formation of colloidal assemblies. Upon increasing the strength of one of the fields, the formation of predominantly linear chains aligned in the direction of the respective field takes place. These states can be regarded as linear string fluids, where the assembly is solely dominated by the single type dipole-dipole interaction (either electric or magnetic). At intermediate field strength of both fields, a bidirectional chain formation is observed, which results into the formation of fine networks or cross-linked particle chains. Upon increasing the absolute magnitude of both field strengths further, these fine networks transform into coarser networks with partially crystallized colloidal domains. This formation of particle networks in bi-axial electric and magnetic fields is a non-equilibrium process and the initially formed metastable structures dynamically reconfigure with prolonged exposure to the fields. Thereby they undergo an aging process characterized by ongoing compactifaction.

The analysis of experiments is accompanied by complications. First, extraction of particle positions from microscopic images was automatized. To this end we used the functionalities of Origin (TM), which requires images of high contrast. Large-scale images as shown in Fig. 1.6(e) turned out to be of insufficient quality for this procedure. Our analysis of the structure formation processes is based on single particle positions and therefore only small scale images will be considered as they yield higher contrasts. Secondly, controlling the area fraction or number density in experiment was difficult. Even for a given sample of constant global area fraction (usually $\phi \approx 0.23$), we found that the particle density was significantly higher or lower in its different regions. Besides the fact that the system is subject to density variations between different samples, this also means that it is characterized by quite large internal density variations. The latter is a consequence of the size of the considered particles. They are relatively large ($\approx 6\mu m$ in diameter) and at the given room temperature, they are not homogeneously distributed throughout the samples. Finally, this means that the observed experimental structure formation depends on the initial local density of the investigated region. As we are interested in the formation and structure of particle aggregates, we focus on regions where particles assemble. Hence, the local density presented in the microscopic photographs is usually higher than the mean density in the sample.

5.1.3 Comparing simulation and experiment

In simulations we therefore restrict our considerations to an intermediate density $\rho^* = 0.35$, which is slightly higher than the mean number density in experiment ($\rho^*_{exp} \equiv 4/\pi\phi \approx 0.3$). Occasionally we consider systems

of number density $\rho^* = 0.3$ when comparing with microscopic images of obviously low particle density.

Importantly, an one-to-one comparison between simulation and experiment could not be established. Although a 'master curve' mapping the experimental parameters (e.g., current in the coils) onto dipole strengths in simulations would be of great help in understanding the systems dynamics, the uncertainties associated with the internal structure (distribution of dipole moments) of the particles and the imperfect control of density in the experimental setup made this unfeasible. Instead, we show in Fig. 5.1 the 'extreme cases' of states corresponding to vertical chaining (a), horizontal chaining (b) and coarse network formation (c) in order to investigate the validity of our simulations. These results are compared between simulation and experiment by microscopic images, snapshots from simulation and the previously (see Sec. 3.5) introduced distributions of fictitious energies u^{el} and u^{mg}. The results from simulation are temporal averages in the range of $8\tau_B$ to $12\tau_B$, while experiments are evaluated between $8s$ and $15s$ after applying the fields.

In the presence of solely the electric field the dominant structural elements are fine linear particle chains oriented along the electric field as can be seen in Fig. 5.1(a). The distributions of u^{el} and u^{mg} show two distinct peaks, corresponding to particles within vertical chains ($u^{el} = -4$ and $u^{mg} = 2$) and corresponding to particles forming ends of vertical chains ($u^{el} = -2$ and $u^{mg} = 1$). Here, the agreement between simulation and experiment is very good, although the theoretical peak at $u^{el} = -4$ is higher and hence indicates a tendency to overestimate the amount of particles within chains at the given simulation parameters. In principle, a systematic search for values of the dipole strength μ^{el} and density ρ^* would allow to optimize the mapping between experiment and simulation. However, as stated previously, this procedure would have to be performed separately for each experimental image (due to the lack of a 'master curve') and would yield no further insights.

In contrast to the electric case we show in Fig. 5.1(b) particle chains formed under the presence of solely the magnetic field. These aggregates are in general more compact and partially staggered, which we assume to be the consequence of dislocations of dipole moments from the particles centers of mass. Here, the distributions of u^{el} and u^{mg} yield only one distinct peak at $u^{el} = 1$ and $u^{mg} = -2$, respectively. These peaks are associated with particles forming the end of chains and appear pronounced and sharp. In contrast to the electric case, simulations underestimate the frequency of 'chain ends'. However, the distributions are in general significantly broader than in the electric case and yield significant contributions for *perturbed* configurations, which is the frequency of states around the major peaks. Interestingly, there is an surprisingly accurate agreement between simulation and experiment with respect to these perturbed particle configurations. This indicates that the deviations from linear chaining are

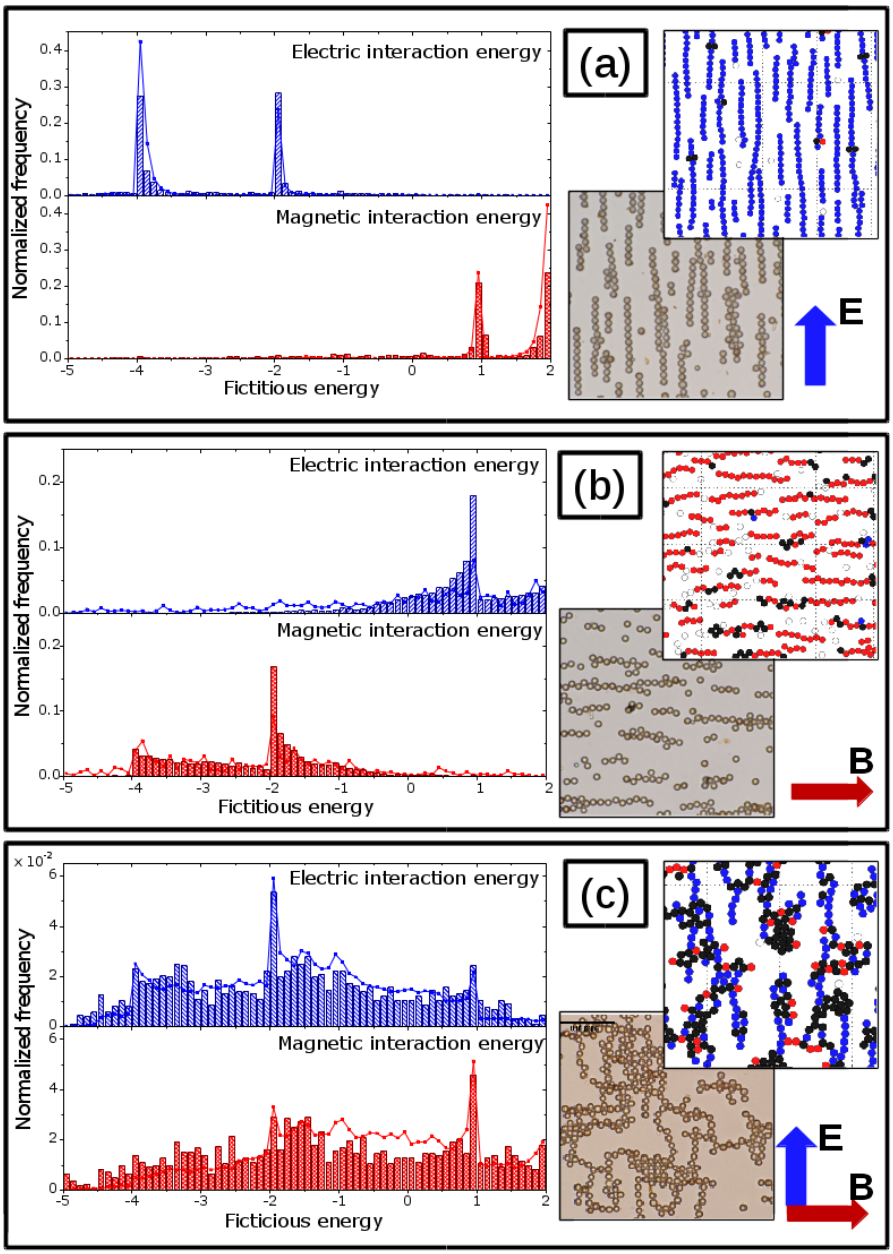

Figure 5.1: Comparison of structures in experiment and simulation under different field conditions. (a) experimental system at $E = 20V/mm, H = 0A/m$ and simulation at $\mu^{el} = 0.3, \mu^{mg} = 0$ and corresponding distributions of u^{el}, u^{mg}, (b) experimental system at $E = 0V/mm, H = 90A/m$ and simulation at $\mu^{el} = 0, \mu^{mg} = 0.35$ and corresponding distributions of u^{el}, u^{mg}, (c) experimental system at $20V/mm, H = 90A/m$ and simulation at $\mu^{el} = 0.45, \mu^{mg} = 0.45$ and corresponding distributions of u^{el}, u^{mg}. Bars in the histograms are experimental data and curves are simulation results.

captured properly by our model. Furthermore we want to note that the model parameter ($\delta = 0.2\sigma$) defining the dislocation of the magnetic interaction center and the simulation parameters ρ^* and $\bar{\mu}^{mg}$ have not been optimized systematically. This is important, because it means that the novel feature of our model, namely the unusual treatment of magnetic interactions, describes the general properties of the real particles, irrespective of the actual values. Besides being a justification for the idea of analyzing the real systems behavior via the theoretical model, these results also support our assumptions about the nature of the real particles (see Sec. 3.4).

The third case of *strong* electric and magnetic field presented in Fig. 5.1 (c), shows the formation of coarse particle networks. Here the distributions of the fictitious energies u^{el} and u^{mg} become very broad and flat and yield only minor peaks at $u^{el} = -2$ and $u^{mg} = 1$ indicating chaining along the electric field. In addition, an even less pronounced peak at $u^{el} = 1$ and an associated region of relatively high frequency at $u^{mg} = -2$ indicate *perturbed* chaining along the magnetic field. Note that the peak heights are two orders of magnitude smaller here than in the previous examples. Again, a quite accurate agreement between simulation and experiment is given by these distributions, although the theoretical curve overestimates magnetic energies u^{mg} in $[-1.5, 0.5]$. This means that the real system has less staggered or perturbed magnetic (horizontal) aggregates than structures from simulation.

Finally, Fig. 3.6 gives the same information for network formation at smaller strengths of both fields. Here, the microscopic image of the colloidal network formed in experiment (see Fig. 3.6) is re-color coded on the basis of particle roles and is compared to the particle assembly formed in the simulations. The distributions of the fictitious energies u^{el} and u^{mg} appear similar to the ones of the coarser network in Fig. 5.1(c), although the minor peak at $u^{mg} = -2$, which is associated with chaining along the magnetic field, is slightly more pronounced and higher in its absolute value. Hence, this network structure is less compact than the one at higher field strengths, although the difference may appear small. In the next section, the difference between these two network types will be discussed in more detail.

In general we can state that the novel way of modeling magnetic interactions presented here results in simulated colloidal structures which are visually indistinguishable and quantitatively comparable to the experimental observations. Furthermore, the characteristics of all qualitatively different states in experiment are also found in simulations. In the next section we will present a state diagram generated from simulations which yields the dependency of the assembly process on the field configuration at constant density and temperature.

(I)	$h > A - n - v$	horizontal chain regime
(II)	$v > A - n - h$	vertical chain regime
(III)	$h + v > A - n$	fine network regime if neither (1) nor (2)
(IV)	$n > A - h - v$	compact network regime

Table 5.1: Definitions of the criteria for states presented in Fig. 5.2. The number of aggregated particles (having at least neighbor) is denoted by A.

5.1.4 State diagram

The limitations in control over local and global density make it impossible to extract the influence of the field strengths on the self-assembly of the colloidal aggregates from experimental side. The surprisingly realistic behavior of our model allows to overcome these difficulties by means of BD-simulations. According to the identification scheme introduced in Sec. 3.5 each particle can be associated with a 'role' and sorted into the populations of node particles n, vertical chain particles v or horizontal chain particles h, which are properly defined in the text above Eq. 3.27. These populations sum up to the total amount of aggregated particles A

$$A = h + v + n. \tag{5.1}$$

Based on this equation, four categories for different types of networks and chain-like structures can be defined. These states correspond to (I) vertical (electric) string fluid , (II) horizontal (magnetic) string fluid, (III) networks of fine single particle chains and (IV) networks of more compact clusters interconnected by chains. The idea is that if either h or v dominate the system we consider it to be string fluid. This is the case when the population h or the population v correspond to more than 50% of all aggregated particles. The actual threshold of 50% is arbitrary, but chosen for simplicity here. Accordingly, Eq. [5.1] can be reformulated and yields the definitions $h > A - v - n$ and $v > A - h - n$ for the magnetic and electric string fluid respectively. A compact network or isolated cluster phase corresponds to a dominant population of node particles ($n > A - v - h$). The finer network structures require the string fluid structures to dominate ($h + v > A - n$). But they are also combinations of different string fluids and hence the cases when either horizontal $h > A - v - n$ or vertical chaining $v > A - h - n$ dominates have to be excluded. The precise definitions of these states are summarized in Table. 5.1

According to these criteria, Fig. 5.2 shows four sketches of particle aggregates whereas particles belonging to different populations (h, v, n) are occasionally indicated. In addition, the non-equilibrium state diagram

for chain and network aggregation at $\rho^* = 0.35$ is shown for various electric and magnetic field strengths. Only states with more than 70% of the particles being aggregated ($A > 0.7N$) are presented. Different colors correspond to the four different states. The presence of these four types of

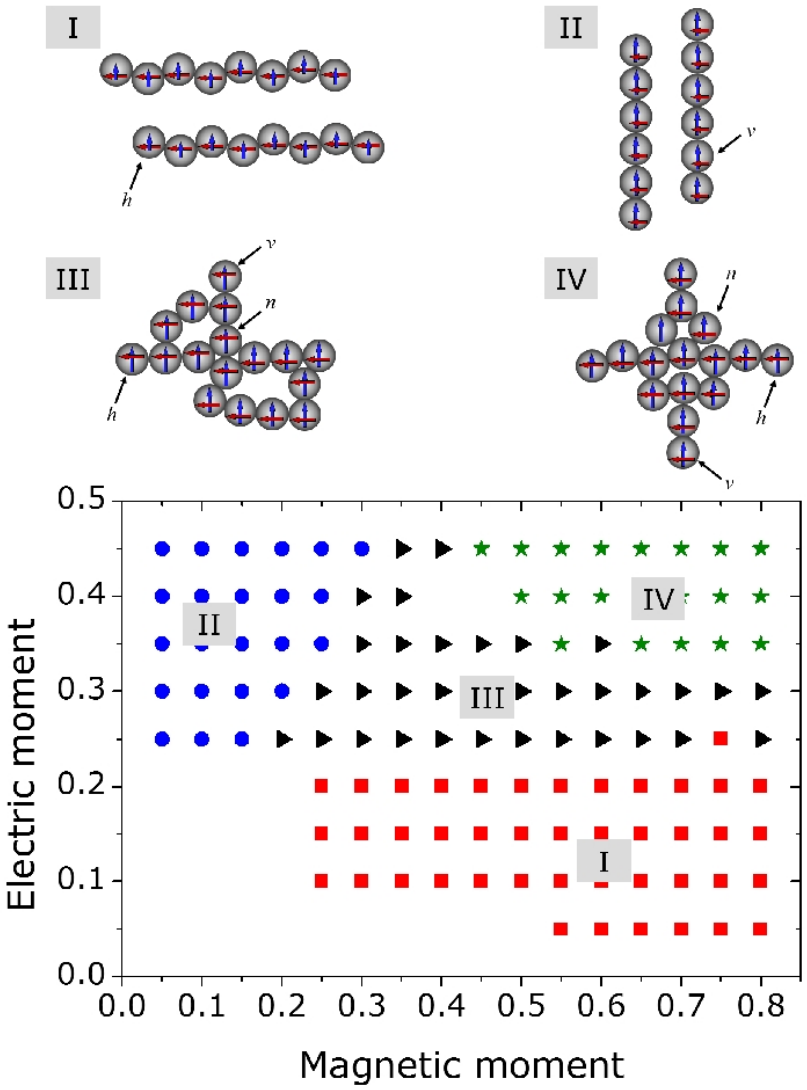

Figure 5.2: Non-equilibrium state diagram for the aggregation of superparamagnetic particles in crossed fields at density $\rho^* = 0.35$. Only states in which more than 70% of particles are members of dimers or larger aggregates are considered.

particle states is governed by the relative and absolute electric and magnetic field strengths. At small dipole moments $\mu^\alpha \leq 0.25$ (or very low field

strengths), no significant assembly was observed. In the borderline case, where one of the fields is much stronger than the other one, the assembled configuration is a string fluid phase (States I or II) oriented in direction of the dominating field. However, as discussed previously the local particle assembly in these states is not the same in external electric and magnetic fields. In the former, aggregates are rather linear and in the latter partially staggered.

A more versatile behavior is observed when the two moments are similar in magnitude ($\mu_{el} \approx \mu_{mag}$). When the absolute values of both moments are comparable but obey $\mu^{\alpha} < 0.4$, a fine bidirectional low-density network or gel-like structure is obtained (state III). Interestingly, the region of fine network states in the state diagram is not symmetric. If the electric moment remains sufficiently small, fine networks can be realized even at relatively strong magnetic interactions. We assume this is the case because the magnetic interaction prefer staggered arrangements and prevent particles from strong compactifaction.

However, if both moments are increased in their absolute magnitudes $\mu^{\alpha} > 0.4$, a more coarse structure with compact particle packing is observed (state IV). In this state, small domains of colloidal clusters are interconnected via (short) particle chains.

Here it should be mentioned that the distinction between the fine and compact network structures is given by a gradual change in the populations of particles with different roles. The actual position of this transition depends on the arbitrary definitions of populations given in Table 5.1. Nevertheless, our characterization is sufficient to show the existence of different states. Moreover, the state boundaries shown in Fig. 5.2 are not very distinct and interchange between the states is gradual. Hence, detection of this smooth crossover in experiment is not possible, especially as it is very sensitive to (local) density variations.

The network states might be regarded as gel-like structures. However, the percolation transition, which is in principle a prerequisite for gelation [101], was not systematically evaluated. Nevertheless, many of the simulated networks turned out to be percolated. Also, the relaxational dynamics, which are needed to identify gelation [101], have not been investigated; still, the presented network structures are transient in character and undergo subsequent compactifaction in time. In Fig. 5.3 the temporal evolution/collapse of the coarse network from Fig. 5.1 (c) is shown. The number of particles in nodes n (black curve) continuously increases with time. At these strong interaction strengths, nearly all particles are aggregated $A \approx 1$ (yellow curve). Interestingly we see that the number of particles in vertical chains dominates the one in horizontal chains. In fact, this is the case in most of the network structures observed, also in the fine networks from experiment and simulation (see Fig. 3.6 (c) and (e)). The population of particles in horizontal chains becomes dominant, only for significantly stronger magnetic fields. Importantly, the categorization of

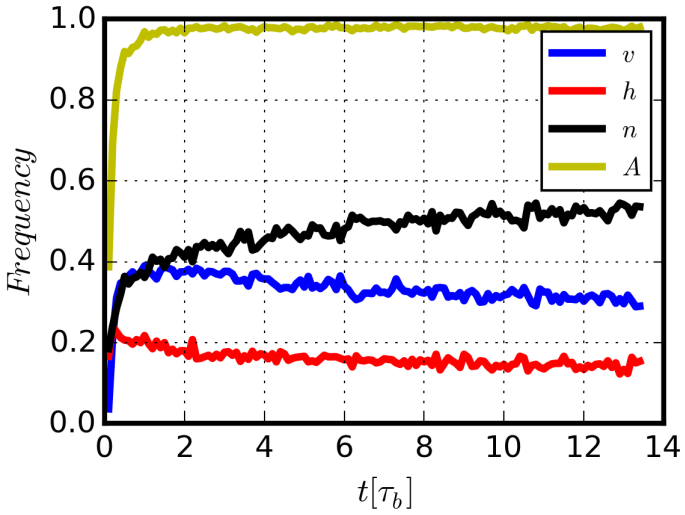

Figure 5.3: Collapse of a network structures in simulation at $\rho^* = 0.35$ and $\mu^{el} = 0.45, \mu^{mg} = 0.45$. Shown is the time evolution of the number of particles in nodes n (black), the number of particles in horizontal/vertical chains h (red/blue) and the number of particles in aggregates A (yellow). This state point corresponds to a coarse network.

certain state points is therefore time dependent.

Such aging processes are known in systems undergoing diffusion limited aggregation, which makes an interpretation as a (chemical) gel reasonable. A final conclusion on whether this system undergoes gelation can not be given here. It is mostly computational reasons why the question on gelation can not be addressed. Calculating percolation transitions as well as temporal correlation functions requires large particle numbers and very long simulation times, which are not accessible with this model.

Importantly, the compactifaction of network structures with increasing field strength is counter intuitive from a conceptional point view. In general, increasing the interaction strength is equal to decreasing the temperature. This relation is usually expressed in the definition of the dipolar coupling strength

$$\lambda = \mu^2 / k_B T. \tag{5.2}$$

In this study, the compactifaction is observed at $\lambda \approx 20\text{-}50$. At such strong couplings, the system should turn towards some sort of diffusion limited aggregation and form *less compact* fractal structures. And indeed, visual inspection of the *large scale* assembly in experiment (Fig. 1.6(e)) makes it reasonable to interpret the structures as fractals. However, locally we find compactifaction by increasing the coupling strength.

In Sec 5.2.4- 5.2.5 and in Sec. 5.3 the relaxational behavior and compactifaction processes will be discussed with respect to results of a com-

putationally more convenient generic model allowing deeper insights into the underlying mechanisms of these assembly processes.

5.2 Diffusion Limited Aggregation in Mutidirectional Fields

Based on Brownian Dynamics computer simulations in two dimensions we investigate aggregation scenarios of colloidal particles with directional interactions induced by multiple external fields. To this end we propose a model which allows continuous change in the particle interactions from point-dipole-like to patchy-like (with four patches). We show that, as a result of this change, the non-equilibrium aggregation occurring at low densities and temperatures transforms from conventional diffusion-limited cluster aggregation (DLCA) to slippery DLCA involving rotating bonds; this is accompanied by a pronounced change of the underlying lattice structure of the aggregates from square-like to hexagonal ordering. Increasing the temperature we find a transformation to a fluid phase, consistent with results of a simple mean-field density functional theory.

5.2.1 Background

In this Section we present results previously published in [111]. Here, we turn towards general properties of the structure formation in colloidal systems with externally induced mutidirectional interaction anisotropies. This is done in a conceptional fashion by means of two-dimensional Brownian dynamics (BD) simulations of a generic particle model, the extended dipole particle model (EDP model), which is inspired by the general setup of the previously presented system and presented in Sec. 3.6. However, the model does not aim on a specific system e.g., magnetic and electric interactions or two temporarily present electric interactions as described in Sec. 3.3, but rather on unveiling the underlying mechanisms of directed aggregation in colloidal systems. Furthermore, the model is designed to be rather simple. The aim is to be able to perform large-scale computer simulations with reasonable effort while still capturing certain characteristic features of the real system. The EDP model does not aim on being a replacement for the crossed dipole particle (CDP) model discussed in the previous section. Rather it is an additional approach

- to investigate large-scale structures (fractal dimension of aggregates),
- to investigate long-time behavior (stability of bonds over long times)
- to analyze the influence of the anisotropy of pair interactions.
- and to identify conceptional aggregation regimes (slippery and anisotropic DLCA)

Indeed, of special interest to us is the interplay between diffusion limited aggregation and interaction anisotropies.

To this end, externally-induced dipole moments are mimicked via pairs of screened Coulomb potentials. The two charges associated with each dipole are shifted outward from the particle center, one parallel to its corresponding field and the other one anti-parallel. A sketch of the internal arrangement of interaction sites in such a particle is shown in Fig. 3.7 for the case of two orthogonal (decoupled) fields. In general, this model allows to investigate also the influence of a third or fourth field. For simplicity, we restrict our considerations here to the case of two decoupled fields. By changing the charge separation, we systematically investigate the (transient) structural ordering and aggregation behavior predicted by this model. Our large-scale Brownian dynamics simulations show that the system is very sensitive to changes in temperature T^*, number density ρ^*, and charge separation δ. In this large parameter space we find a variety of different states ranging from small fractal aggregates and single-chain structures at low temperatures to coarser, isolated or interconnected clusters at higher temperatures.

Highlights of our results are the following: At very high interaction energies and large charge separations we find that the particles undergo anisotropic diffusion limited cluster aggregation with rectangular local particle arrangements. Lowering the charge separation shifts the model behavior to a slippery diffusion limited aggregation (sDLCA) regime accompanied by a sharp transition of the lattice structure from rectangular to hexagonal. In the proximity of this transition we observe long-lived or arrested frustrated structures consisting of strongly interconnected hexagonal and rectangular lattice domains connected with each other. We also show that, upon increase of the temperature, the systems enter a fluid state. The corresponding 'fluidization' temperature turns out to be very close to the spinodal temperatures obtained from a mean-field density functional theory.

The rest of this section is organized as follows. First we present our model and explain different target quantities which will be calculated from the simulations. Secondly, the numerical results are described. In the sections 5.2.2 - 5.2.4 we first discuss the local and global structures and the temporal stability of aggregates at a low temperature and an intermediate density, focusing on the impact of the model parameter δ. In section 5.2.5 and 5.2.6 we then turn to the impact of temperature and density. Finally, the conclusions summarize the results.

Target quantities To characterize the structure of the systems we consider several quantities. The first one is the mean coordination number

$$\bar{z} = \frac{1}{N}\sum_{i=1}^{N} z_i, \tag{5.3}$$

where z_i is the number of neighbors of particle i and the sum is over all particles. In the following, two particles are considered to be nearest neighbors if their center-to-center distance is smaller than $r_b = 1.15\sigma$.

To identify local particle arrangements, the orientational bond order parameter is of special importance. For particle k it is given by

$$\phi_k^n = \frac{1}{z_k}\sum_{l=1}^{z_k} |\exp(in\theta_\lambda^{kl})| \tag{5.4}$$

with z_k being the number of neighbors and $\theta_\lambda^{kl} = \arccos(\mathbf{r}_{kl}\cdot\mathbf{r}_{k\lambda}/(r_{kl}r_{k\lambda}))$ being the angle between the bond of particle k and its neighbor l measured against a randomly chosen bond of particle k to one of its neighboring particles λ. Hence, $\phi_k^n = 0$ for $z_k < 2$. The integer value n determines the type of order which is detected by this parameter. We concentrate on ϕ_4 and ϕ_6 to identify square (rectangular) and hexagonal lattice types. Its ensemble average is calculated via

$$\Phi_n = \frac{1}{N}\sum_{i=1}^{N} \phi_i^n. \tag{5.5}$$

The reversibility of 'bond' formation and slipperiness of existing bonds can be characterized by the bond and the bond-angle auto-correlation functions $c_b(t)$ and $c_a(t)$. To evaluate $c_b(t)$ we assign a variable $b_{ij}(t)$ to each pair of particles at each time step which is 1 if the particles i and j are nearest neighbors or zero otherwise. The bond auto-correlation function is then defined as

$$c_b(t, t_0) = \langle b_{ij}(t_0) b_{ij}(t)\rangle, \tag{5.6}$$

where the brackets indicate an average over all pairs that are bonded at time t_0. The bond-angle auto-correlation function $c_a(t, t_0)$ is defined similarly by defining the unit vector

$$\mathbf{a}_{ij}(t) = \mathbf{r}_{ij}(t)/r_{ij}(t), \tag{5.7}$$

such that

$$c_a(t, t_0) = \langle 1 - \arccos(\mathbf{a}_{ij}(t)\cdot\mathbf{a}_{ij}(t_0))/\pi\rangle \tag{5.8}$$

where we average again over all pairs. While c_b gives the information on how stable bonds are over time, c_a tells how stable their direction

is over time. Note that in contrast to the typical definition of correlation functions for stationary systems [134, 136], here the functions $c_b(t)$ and $c_a(t)$ are not independent of the time origin t_o, although this dependency will not be denoted in the following.

Finally, we consider the fractal dimension D_f of particle clusters, which is particularly important in the context of DLCA. Clusters are defined as a set of particles with common next neighbors. The size of a cluster is then quantified by its radius of gyration

$$R_g^2 = \frac{1}{N_{cl}} \sum_{i=1}^{N_{cl}} (\mathbf{r}_i - \bar{\mathbf{r}})^2, \tag{5.9}$$

where N_{cl} is the number of particles in the cluster, and $\bar{\mathbf{r}}$ is the potion of its center-of-mass. By plotting $\ln R_g$ against $\ln N_{cl}$ for different clusters, we extract the fractal dimension D_f via the relationship $R_g \sim N_{cl}^{1/D_f}$ (see Ref. [124, 98]).

Tabular representation of reduced units.

reduced density	$\rho^* = \rho\sigma^2$
reduced temperature	$T^* = k_B T/\epsilon$
reduced interaction strength	$u^* = u/\epsilon = -2.804$
Brownian time scale	$\tau_b = \sigma^2\gamma/k_B T$

5.2.2 The interaction anisotropy - Effect on local order

At first we study the system at low temperature $T^* = 0.05$ and intermediate density $\rho^* = 0.3$ for different charge separations δ. In Fig. 5.4 simulation snapshots for $\delta = 0.1\sigma, 0.21\sigma, 0.3\sigma$ at $t = 300\tau_b$ [see. Eq. (3.35) below] are shown, where τ_b is the Brownian timescale. The color-code reflects the orientational bond order parameter ϕ_i^4 of each particle i. All three cases are characterized by clusters with irregular shapes. However, local particle arrangements differ strongly. While for $\delta = 0.1\sigma$ the particles aggregate in a hexagonal fashion, at $\delta = 0.3\sigma$ they aggregate into rectangular structures. At the intermediate charge separation $\delta = 0.21\sigma$, hexagonal order dominates the system; however, some clusters also reveal subsets of particles in rectangular arrangements. A more quantitative description is given by the orientational bond order parameters $\Phi_{4(6)}$ shown in Fig. 5.5(a) as functions of δ. By increasing δ, one observes a sharp transition at $\delta \approx 0.21\sigma$ from hexagonal towards rectangular (square) order.

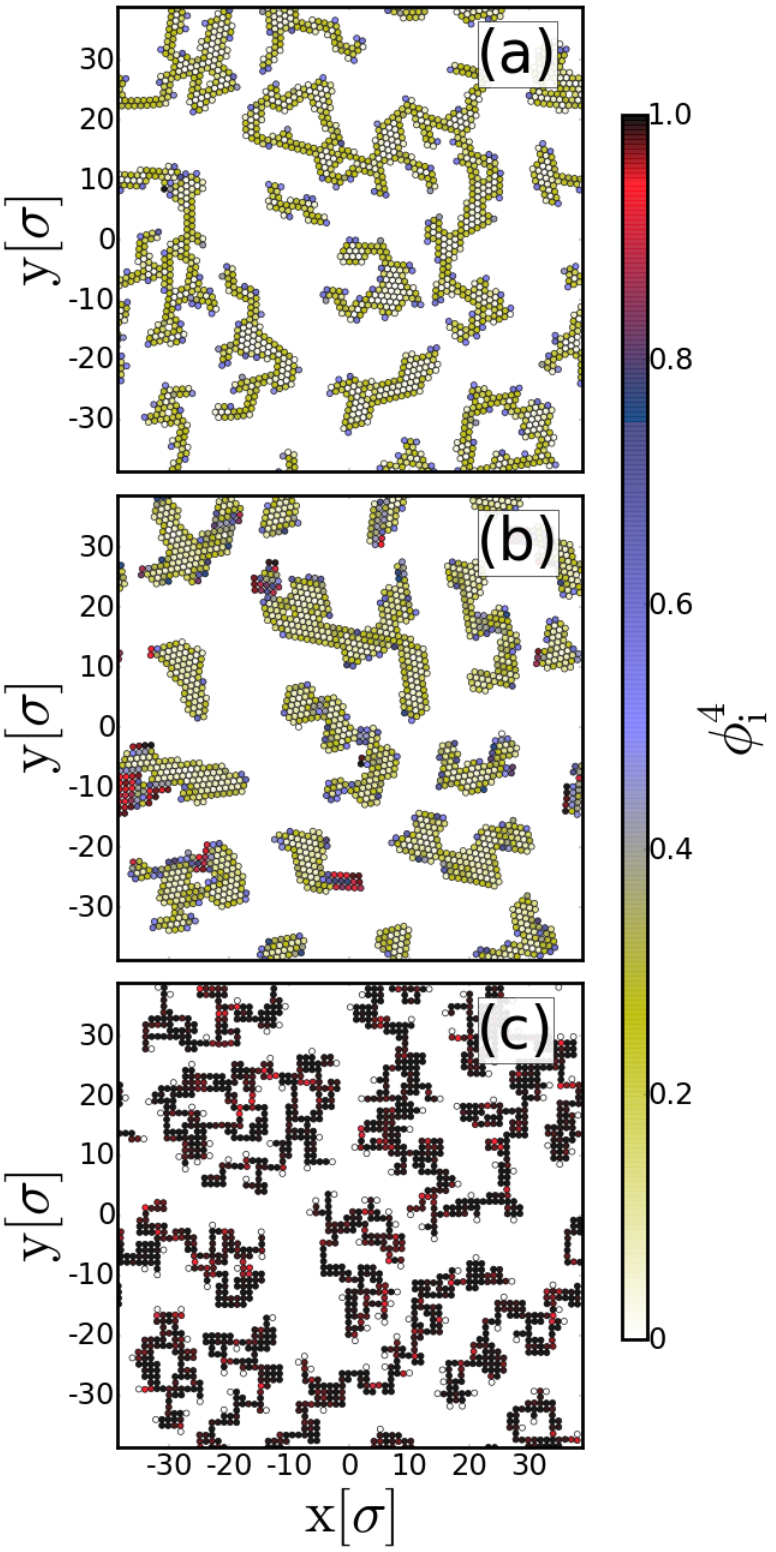

Figure 5.4: Simulation snapshots at $\rho^* = 0.3$ and $T^* = 0.05$ for (a) $\delta = 0.1\sigma$, (b) $\delta = 0.21\sigma$ and (c) $\delta = 0.3\sigma$. Particles are colored according to their value of ϕ_i^4.

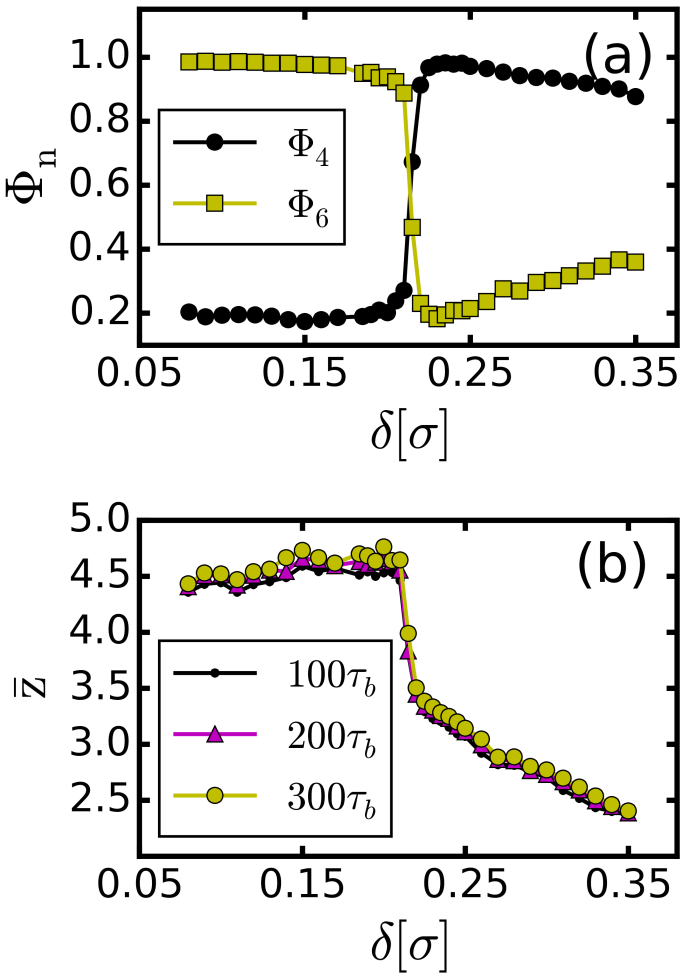

Figure 5.5: Results for simulations with $N = 1800$ at temperature $T^* = 0.05$ and density $\rho^* = 0.3$. (a) Orientational bond order parameters Φ_4 for square (black) and Φ_6 (yellow) for hexagonal particle arrangements. (b) Mean coordination number $\bar{z}$ as function of charge separation δ at times $t = 100, 200, 300\tau_b$.

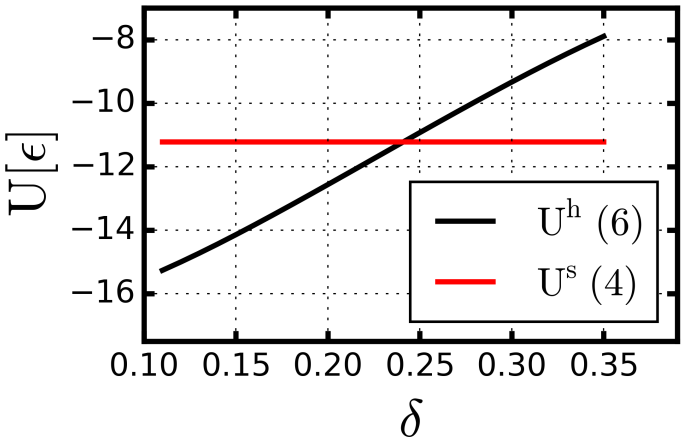

Figure 5.6: Minimum energy of a particle with six neighbors in hexagonal arrangement as function of δ (black) and energy for a particle in rectangular arrangement with 4 neighbors (red).

This transition turned out to be independent of the considered particle numbers as test simulations revealed. Physically, it can be interpreted as a reduction in valency of a 'patchy' particle from six-fold (isotropic interaction) to four-fold.

The very presence of such a sharp transition can be explained via energy arguments based on the δ-dependent pair potential plotted in Figs. 3.8(a)-(d). To this end, we calculate the energy $U_i^{hex}(\delta) = \sum_{j=1}^{6} U(\mathbf{r}_{ij})$ of a particle i with six neighbors j, which are located in a hexagonal arrangement at 'contact' distance σ around i. Note that not all hexagonal configurations do have the same contact energy. This is due to the anisotropy of interactions, see Fig. 3.8(d). Therefore we consider a hexagonal configuration in which the contact energy is as low as possible (this configuration was found numerically). The dependence of this lowest contact energy $U_i^{hex}(\delta)$ on the charge separation parameter is plotted in Fig. 5.6. Also shown is the corresponding energy $U_i^{sq}(\delta) = \sum_{j=1}^{4} U(\mathbf{r}_{ij}) = 4 \times u$ of a particle with four neighbors j located at distance σ in a rectangular arrangement, i.e., in the energy minima around i (the quantity u was defined below Eq. (3.31)). Note that the energy $U_i^{sq}(\delta)$ does not depend on δ according to Eq. (3.32). As shown in Fig. 5.6, the two curves intersect at a "critical" value of $\delta = 0.24\sigma$. Thus, the simple energy arguments already suggest a transition between states with local hexagonal and square order, even though the predicted critical value is somewhat larger than the value of $\delta = 0.21\sigma$ seen in the actual simulations at finite temperature and density [see Fig. 5.5(a)].

Further information is gained from the behavior of the mean coor-

dination number as a function of δ plotted in Fig. 5.5(b) for three different times $t = 100\tau_b$, $200\tau_b$ and $300\tau_b$. At all times considered, $\bar{z}$ undergoes a steep decrease at $\delta \approx 0.21\sigma$ from a nearly constant value, $\bar{z}_{hex} \approx 4.5$, to a value $\bar{z}_{sq} \approx 3.5$. This behavior reflects, on the one hand, again the presence of a sharp transition; on the other hand, the actual values of $\bar{z}_{hex}(\bar{z}_{sq})$ reveal the "non-ideal" character of the aggregates in terms of coordination numbers. For example, for $\delta > 0.21\sigma$ we find that $\bar{z}$ and Φ_4 decrease with δ, while Φ_6 increases. However, this does not indicate a decline of the rectangular order; it rather results from an increasing amount of particles residing in chains oriented either in x- or y-direction. The coordination number z_i of a particle i in such a chain is ≤ 2, leading to a mean coordination number $\bar{z} < 4$. Furthermore, the parameters ϕ_i^4 and ϕ_i^6 [see Eq. (5.4)] become unity for a particle forming exactly two bonds under an angle of π (straight chain). This does not affect Φ_4, which is already large at $\delta > 0.21\sigma$, but significantly increases Φ_6. Finally, the counter-intuitive decrease of Φ_4 with δ results from the increasing amount of particles with only one neighbor (e.g., ends of chains appearing white in Fig. 5.4(c)). These particles yield no contribution to Φ_4 [see Eq. (5.4)].

The "non-ideal" values of $\bar{z}_{hex}$ and $\bar{z}_{sq}$ also explain why our energy argument for the location of the hexagonal-to-square transition, which was based on ideal arrangements with six and four neighbors, respectively, does yield the transition value $\delta = 0.24\sigma$ rather than $\delta = 0.21\sigma$ obtained from simulation. We can now reformulate the argument by using the actual mean coordination numbers extracted from our simulations, $\bar{z}_{sq} = 3.5$ (instead of 4) and $\bar{z}_{hex} = 4.5$ (instead of 6). Following the calculations for the ideal arrangements described before, the energy of the square-like arrangement is $U^{sq} = 3.5 \times u$. For the hexagonal arrangement, we use the average minimum energy with either $z_i = 4$ or $z_i = 5$ neighbors, yielding $\bar{U}^h(\bar{z}_{hex}, \delta) = (U^{hex}(4, \delta) + U^{hex}(5, \delta))/2$. The resulting critical value of the charge separation is $\delta \approx 0.21\sigma$, which coincides nicely with the transition value observed in our simulations.

5.2.3 Transient character of aggregates

Although the local structures characterized by $\bar{z}$ and $\Phi_{4(6)}$ persist, in general, over the simulation times considered, we are still facing a *transient* (out-of-equilibrium) structure formation as seen, e.g., from the slight increase of $\bar{z}$ with time in Fig. 5.5(b). This raises a question about the typical "lifetime" of the aggregates.

To this end we now consider dynamical properties, namely the bond and bond-angle auto-correlation functions, $c_b(t)$ and $c_a(t)$. It is not

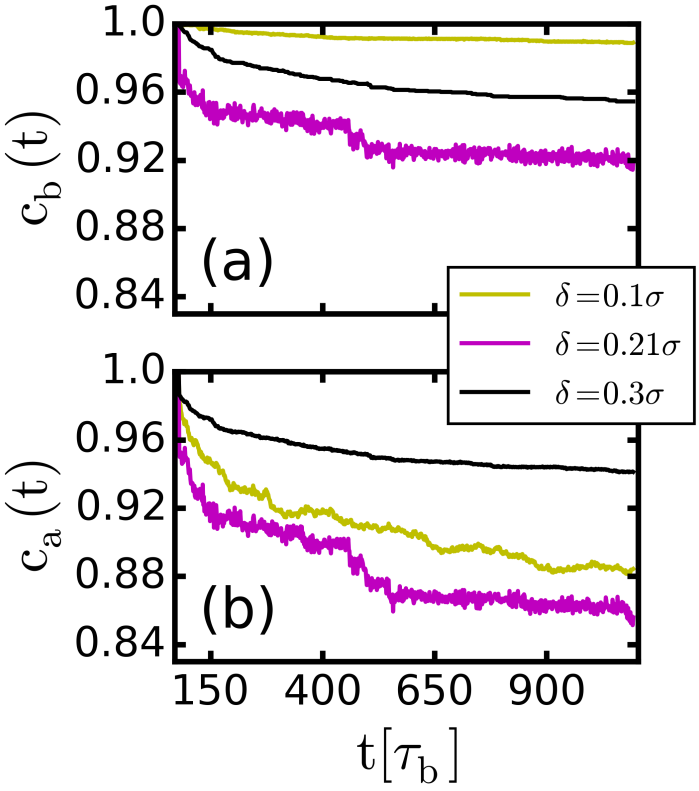

Figure 5.7: Time correlation functions obtained from simulations with $N = 1800$ at temperature $T^* = 0.05$ and density $\rho^* = 0.3$. (a) [(b)] Time evolution of the bond [angle] auto-correlation function $c_b(t)$ $[c_a(t)]$ for three different charge separations $\delta = 0.1\sigma, 0.21\sigma$ and 0.3σ colored in yellow, purple and black respectively.

reasonable to extract decay rates from these functions (as it is usually done) because in transient states, decay rates are, strictly speaking, functions of time themselves. Still, it is interesting to see whether the temporal correlation of bonds (bond angles) for different δ allows us to distinguish between *qualitatively* different aggregation regimes.

Numerical results for $c_b(t)$ and $c_a(t)$ are plotted in Figs. 5.7(a) and (b), respectively, where we consider a large time range up to $t \approx 10^3 \tau_b$. The time axis starts at the finite time when all the systems have formed stable aggregates. The data in Figs. 5.7(a) and (b) pertain to three representative values of the charge separation parameter related to the hexagonal structures ($\delta = 0.1\sigma$), rectangular structures ($\delta = 0.3\sigma$), and to the transition region ($\delta = 0.21\sigma$). In the square regime ($\delta = 0.3\sigma$) the decay of both $c_b(t)$ and $c_a(t)$ is almost identical

and very slow. From this we conclude that the square regime is characterized by almost unbreakable bonds with *fixed* orientations. This is different in the hexagonal regime ($\delta = 0.1\sigma$) where $c_b(t)$ remains nearly constant even after long times (meaning that bond-breaking is very unlikely), while $c_a(t)$ decays much faster. Thus, the directions of bonds are less restricted. We interpret this behavior as evidence that two particles, though being bonded, are still able to rotate around each other to some extent. This is a characteristic feature of *slippery* bonds. Finally, in the transition regime ($\delta = 0.21\sigma$) both functions $c_b(t)$ and $c_a(t)$ decay significantly faster than in the other cases, with the decay of the bond-angle correlation function being even more pronounced. In that sense we may consider the bonds in the transition region also as slippery (although less long-lived than in the other cases).

We conclude that the different structural regimes identified in the preceding section are indeed characterized by different relaxational dynamics. Moreover, all of the observed aggregates have lifetimes of at least several hundred τ_b. Such long-lived bonds are indicative of diffusion limited cluster-cluster aggregation. In the next section we therefore consider the fractal dimension.

5.2.4 The interaction anisotropy - Effect on large-scale fractal structure

In Fig. 5.8 the fractal dimension D_f is shown as a function of δ at time $t = 250\tau_b$, density $\rho^* = 0.3$ and temperature $T^* = 0.05$. We find that D_f increases slightly with δ but remains in a range between 1.4 and 1.5, except at $\delta = 0.21\sigma$. There, the fractal dimension exhibits a bimodal distribution, taking values between $D_f \approx 1.48$ and $D_f \approx 1.6$ (dashed line in Fig. 5.8).

Despite these variations and taking into account the error range, the values of D_f found here are significantly smaller than the fractal dimension $D_f = 1.71$ observed in earlier studies of DLCA in two-dimensional continuous (off-lattice) systems [124, 119]. Except for the case $\delta = 0.21\sigma$, the values in Fig. 5.8 are comparable with previous findings for DLCA in two-dimensional *lattice* systems and systems with spatial or interaction anisotropies [130, 131, 132]. The present system is indeed anisotropic in the sense that the external fields impose preferences on the directions of particle bonds and therefore also on the orientations of aggregates. This effect is most pronounced in the rectangular regime ($\delta = 0.3\sigma$). Therefore, it is plausible that our system undergoes a special case of anisotropic DLCA, in (quantitative) accordance with experimental results [98] and theoretical predictions [120, 130, 131, 127]. We should note

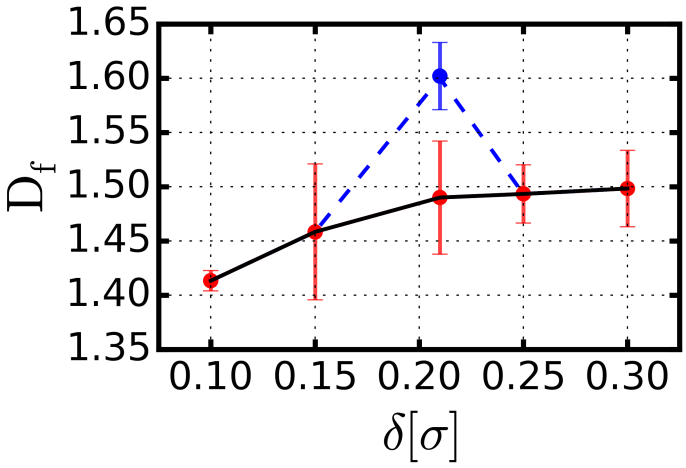

Figure 5.8: Fractal dimension D_f as a function of charge separation at $\rho^* = 0.3$ and $T^* = 0.05$. At $\delta = 0.21\sigma$ we find a bimodal distribution of fractal dimension with peaks at $D_f = 1.48$ (solid line) and 1.6 (dashed line).

that, due to our simulation method, the cluster sizes (typically involving $10^1 - 10^3$ particles) are relatively small compared to the particle numbers considered in the literature (10^6 particles) [119, 157, 120] and therefore most probably subject to finite size effects. A more accurate study of (the impact of anisotropic interactions on) the fractal dimension is beyond the scope of this study. Still, our results do indicate a non-typical diffusion limited aggregation behavior.

We also relate our findings to the newer concept of slippery DLCA [123, 116], where the bonds are essentially unbreakable but able to rotate. Indeed, as discussed in section 5.2.3, bonds are slippery in nature for small δ in the hexagonal regime. For three-dimensional systems it has been reported [123, 116] that the fractal dimension D_f remains the same for slippery and classical DLCA, while the mean coordination number $\bar{z}$ differs. Specifically, $\bar{z}$ is significantly higher for sDLCA [123, 116]. The same observation emerges when we consider our values of $\bar{z}$ plotted in Fig. 5.5(b), from which one sees a pronounced decrease of $\bar{z}$ upon entering the square (DLCA) regime. However, in contrast to earlier studies we find D_f to slightly increase with δ, especially in the hexagonal regime. We interpret this behavior as a consequence of the fact that binding energies in the hexagonal regime decrease with increasing values of δ, while they remain constant in the square regime (see Fig. 5.6). The corresponding stability of bonds should be correlated to the binding energies which explains the slightly increasing values of D_f in the hexagonal

regime. Note that the increase of D_f with δ turns out to be larger (but still comparable) than the error range in Fig. 5.8. Hence, the interpretation given above remains somewhat speculative.

Finally, in the transition region ($\delta = 0.21\sigma$) we found a bimodal distribution of the fractal dimensions D_f with maxima at $D_f \approx 1.48$ and $D_f \approx 1.6$. This second maximum corresponds to only $\approx 25\%$ of the considered cases (twelve independent simulation runs). The first maximum at $D_f \approx 1.48$ therefore clearly dominates and fits nicely to the functional dependence of D_f on δ (see Fig. 5.8). We assume that the less frequent peak results from a 'switching' of the local structures between hexagonal and rectangular arrangements, which is accompanied by a significantly larger bond-breaking probability (see Fig. 5.7(c)). Again this allows compactifaction of aggregates and increases the fractal dimension in the transition regime.

5.2.5 Beyond DLCA - Higher temperatures

Diffusion limited aggregation is restricted to systems with attractive particle interactions much stronger than $k_B T$. By increasing the temperature sufficiently, thermal fluctuations become able to break bonds which results in a faster decay of the the bond autocorrelation functions and a compactifaction of aggregates. Indeed, for square lattice models it was found that D_f is a monotonically increasing function of temperature [132, 129]. In Fig. 5.9(a) the fractal dimension D_f of the present model is plotted as a function of temperature T^* for charge separations $\delta = 0.1\sigma, 0.21\sigma$ and 0.3σ.

We first concentrate on the case $\delta = 0.3\sigma$, corresponding to the square regime at low T^*. In the range of very low temperatures $T^* < 0.25$, the fractal dimension is small and stays essentially constant. Increasing T^* towards slightly larger values then leads to an increase of D_f, reflecting the (expected) compactifaction. This increase of D_f is accompanied by an increase of the mean coordination number $\bar{z}$ [see Fig. 5.9(b)] within the temperature range considered, indicating the growing number of bonds due to local and global structural reconfigurations. The corresponding changes in the stability of the bonds are illustrated in Fig. 5.10, where we have plotted the time evolution of $c_b(t)$ for several temperatures (at $\delta = 0.3\sigma$). Clearly, the decay of $c_b(t)$ becomes faster for higher temperatures. This is the reason why structural reconfigurations and, in consequence, compactifaction of aggregates becomes possible.

These trends persist until $T^*_{f,sq} \approx 0.375$, beyond which the system at $\delta = 0.3\sigma$ starts to behave in a qualitatively different way. The mean coordination number $\bar{z}$ displays a maximum and subsequently a rapid decay. We also find that the fractal dimension has not yet

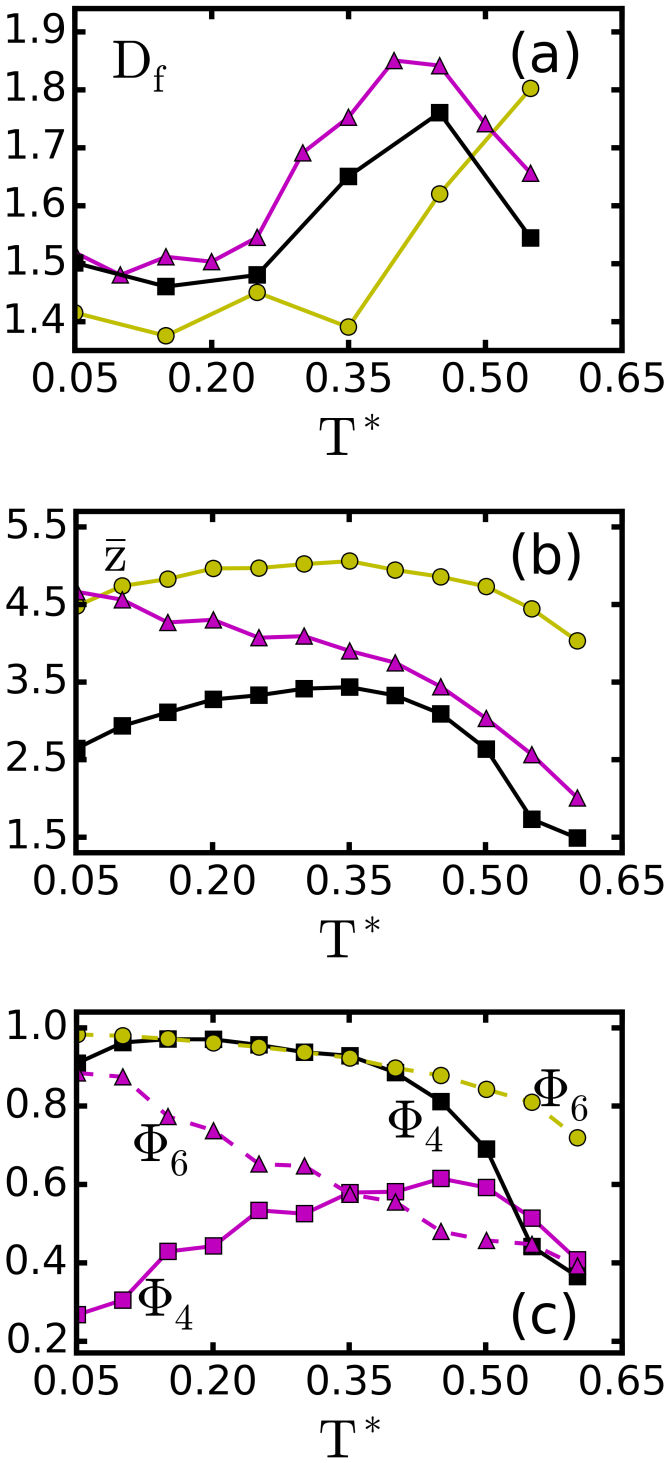

Figure 5.9: Temperature dependence of the system properties at density $\rho^* = 0.3$ for charge separations $\delta = 0.1, 0.21, 0.3\sigma$ colored in yellow, purple and black, respectively. (a) Fractal dimension D_f evaluated at $t \approx 250\tau_b$, (b) Mean coordination number, (c) Orientational order parameters Φ_4 and Φ_6.

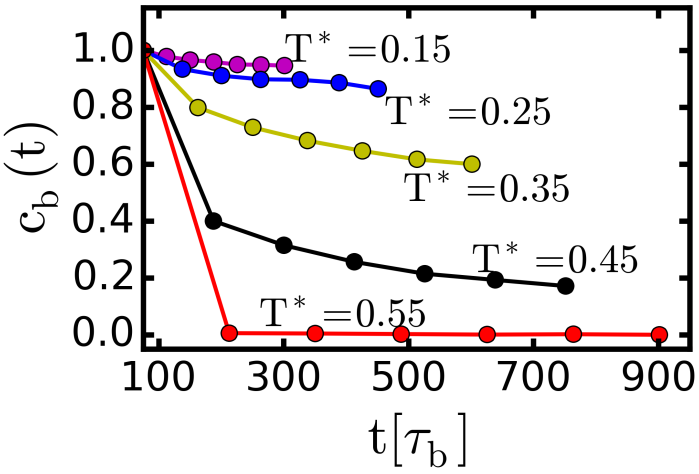

Figure 5.10: Bond auto correlation function $c_b(t)$ for different temperatures T^* at charge separation $\delta = 0.3\sigma$ and density $\rho^* = 0.3$.

reached its maximum value at $T^*_{f,sq}$; this maximum occurs at the slightly larger temperature $T^* \approx 0.42$ (see Fig. 5.9(a)). This 'delay' of D_f can be understood from the fact that, upon the entrance of bond-breaking, filigree parts of the aggregates are more likely affected than more compact ones. Hence, the fraction of 'compact' small aggregates still grows. Even more important, the function $\Phi_4(T^*)$ in Fig. 5.9(c) displays a pronounced decay of rectangular order for $T^* > T_{f,sq}$. From the sum of these indications we conclude that, at temperatures higher than $T^*_{f,sq} \approx 0.375$, the system transforms into a (stable or metastable) *fluid* phase. In this fluid phase, the *overall* structure starts to become homogeneous and isotropic, while the local structures involve only a small number of bonds with short bond-life times.

For the system at $\delta = 0.1\sigma$ (hexagonal structure at low T^*), an estimate of the "fluidization" temperature $T^*_{f,hex}$ based on the behavior of order parameters, coordination number and fractal dimension is more speculative. Nevertheless, the data suggest that $T^*_{f,hex} > T^*_{f,sq}$. This is indicated, first, by the fact that $\Phi_6(T^*)$ decays only very slowly with temperature until $T^* \approx 0.6$ (see Fig. 5.9(c)). Second, the mean coordination number shows only a weak maximum (and no fast decay after-wards) compared to the case $\delta = 0.3\sigma$. Third, the fractal dimension keeps increasing with T^* for all considered temperatures $T^* < 0.6$. Therefore we conclude that $T^*_{f,hex} > 0.6$. We understand this higher fluidization temperature at $\delta = 0.1\sigma$ from the fact that binding energies in hexagonal structures are larger; therefore, higher coupling energies must be overcome.

To further justify these interpretations, particularly the emergence

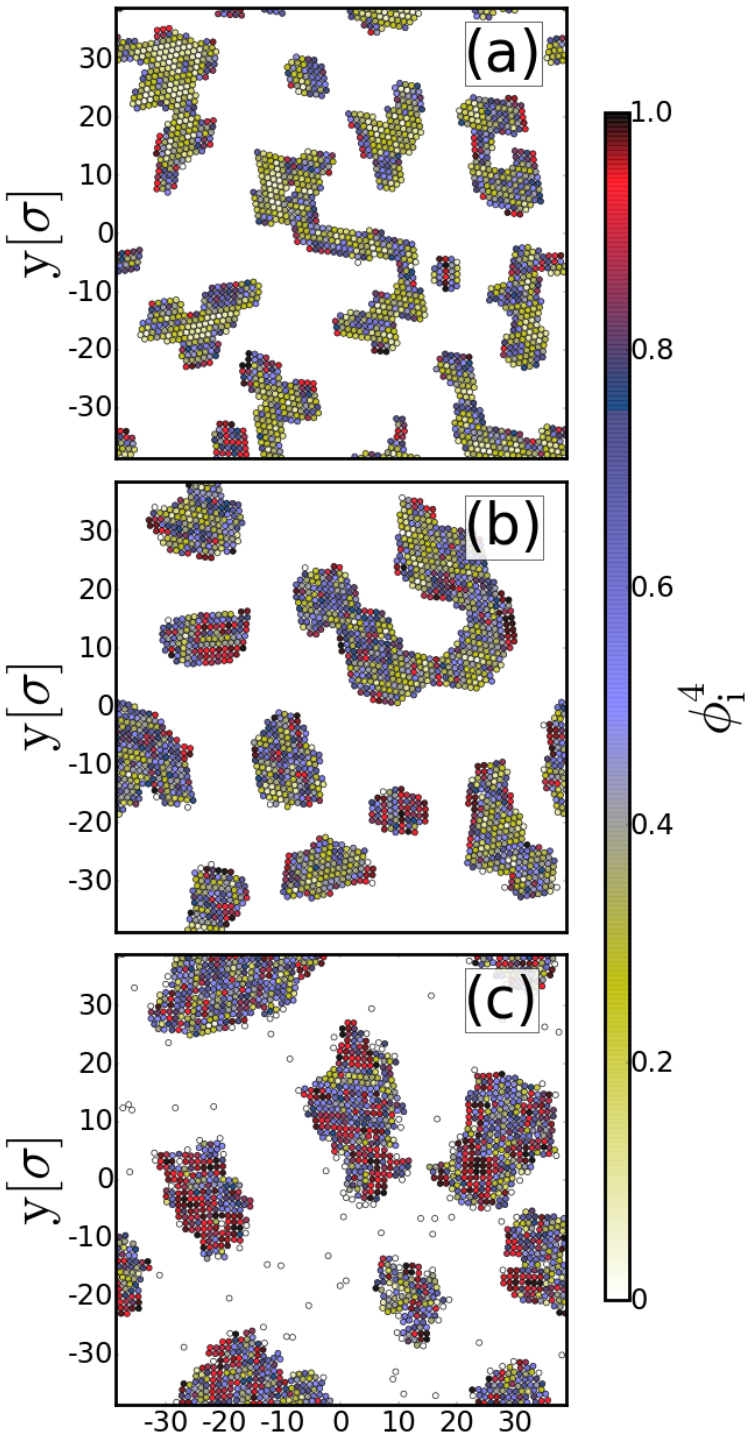

Figure 5.11: Simulation snapshots at $\rho^* = 0.3$ with $\delta = 0.21\sigma$ at (a) $T^* = 0.15$, (b) $T^* = 0.3$, and (c) $T^* = 0.45$. Particles are colored according to their value ϕ_i^4.

of fluid phases, we performed a stability analysis of the homogenous isotropic high temperature state based on mean-field density functional theory (DFT). Specifically, we consider the isothermal compressibility χ_T. Positive values of χ_T imply that the homogeneous (fluid) phase is stable, whereas negative values indicate that this phase is unstable. Specifically, the instability arises against long-wavelength density fluctuations, i.e. condensation. According to Kirkwood-Buff theory [156] one has

$$\chi_T^{-1} \propto 1 - \rho\tilde{c}(k=0), \tag{5.10}$$

where $\tilde{c}(0)$ is the Fourier transform of the direct correlation function (DCF) $c(\boldsymbol{r}_{12})$ in the limit of long-wavelengths ($k \to 0$). We approximate the DCF for distances $r_{ij} > \sigma$ according to a mean field (MF) approximation, that is

$$c_{MF}(\mathbf{r}_{12}) = -(k_B T)^{-1} U(\mathbf{r}_{12}), \quad r_{12} > \sigma, \tag{5.11}$$

and use the Percus-Yevick DCF $c_{HS}(r_{12})$ of a pure hard-sphere fluid [139] for $|\mathbf{r}_{12}| \leq \sigma$. The full DCF is then given by

$$c(\mathbf{r}_{12}) = c_{HS}(r_{12}) + c_{MF}(\mathbf{r}_{12}). \tag{5.12}$$

In Fig. 5.12 we present numerical results for the expression $1 - \rho\tilde{c}(0)$ at $\rho^* = 0.3$ as function of temperature. At low T^*, all systems are characterized by *negative* values of $1 - \rho\tilde{c}(0)$. This indicates that the homogeneous isotropic phase is unstable, consistent with the results

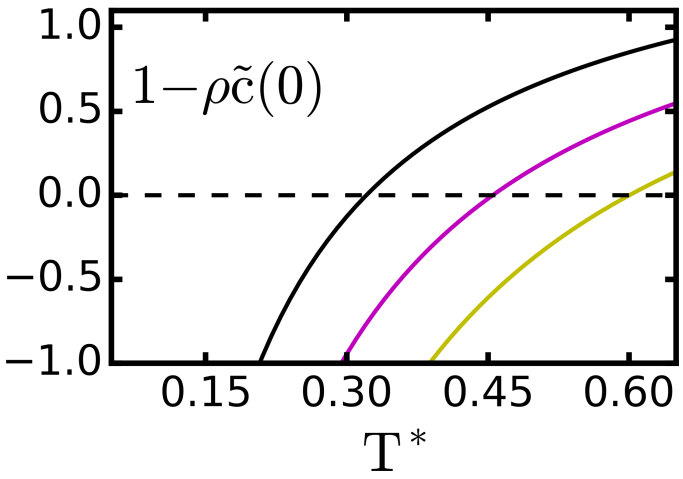

Figure 5.12: Numerical solutions to Eq.5.10 as function of T^* for density $\rho^* = 0.3$ and charge separations $\delta = 0.1, 0.21, 0.3\sigma$ colored in yellow, purple and black, respectively.

of our simulations. Upon increasing T^* the mean-field compressibility χ_T then becomes indeed positive for all charge separations considered. Specifically, for $\delta = 0.3\sigma$ the change of sign (related to a "spinodal point") occurs at $T^*_{f,sq} = 0.325$ and for $\delta = 0.1\sigma$ at the much higher temperature $T^*_{f,hex} = 0.6$. These values are in surprisingly good agreement with our estimates for the "fluidization" temperatures based on the order parameter plots.

The case $\delta = 0.21\sigma$ is again different. Here we find [see Fig. 5.9(b)] that, starting from low temperatures inside the DLCA regime, the mean coordination number monotonically decreases. However, this does not indicate "fluidization" but rather a *gradual* transition from a state with dominant hexagonal order towards a mixed state comprised of coexisting clusters with local hexagonal and square-like order. Indeed, [see Fig. 5.9(c)], the orientational order parameters Φ_4 and Φ_6 reveal that the fraction of particles bound in square clusters increases with T^* and finally overtakes the fraction of particles involved in hexagonal clusters at $T^* \approx 0.35$. Corresponding snapshots of simulation results are shown in Fig. 5.11. At all temperatures considered one observes separated clusters. With increasing temperature their shape becomes more regular, while the local rectangular order becomes more pronounced. Finally, at $T^* = 0.45$ the fractal dimension D_f and the square order parameter Φ_4 reach their maximum values, suggesting a "fluidization" similar to the behavior observed at other values of δ. Interestingly, our stability analysis [see Eq. (5.10)] indicates an instability at the same temperature $T^*_f = 0.45$. With this surprisingly accurate agreement between theory and simulation, we conclude that in the transition regime ($\delta = 0.21\sigma$), increasing thermal fluctuations first push the system from a dominantly hexagonal state into a rectangular one, which then enters a metastable fluid phase after passing the "spinodal point".

5.2.6 Spotlight on higher densities

In this section we revisit the systems behavior at the low temperature $T^* = 0.05$, but consider different densities in the range $\rho^* \leq 0.7$. Whereas low-density systems at $T^* = 0.05$ display DLCA as discussed in section 5.2.4, this aggregation mechanism is expected to disappear at higher densities: here, the particles are just unable to diffuse sufficiently freely. Rather, the particles will very frequently collide and then immediately form rigid bonds. A typical structure at the highest density considered, $\rho^* = 0.7$, and separation parameter $\delta = 0.21\sigma$ is shown in Fig. 5.13. Clearly, the system is percolated, that is, the particles form a single, system-spanning cluster. Interestingly, this cluster is composed of extended regions charac-

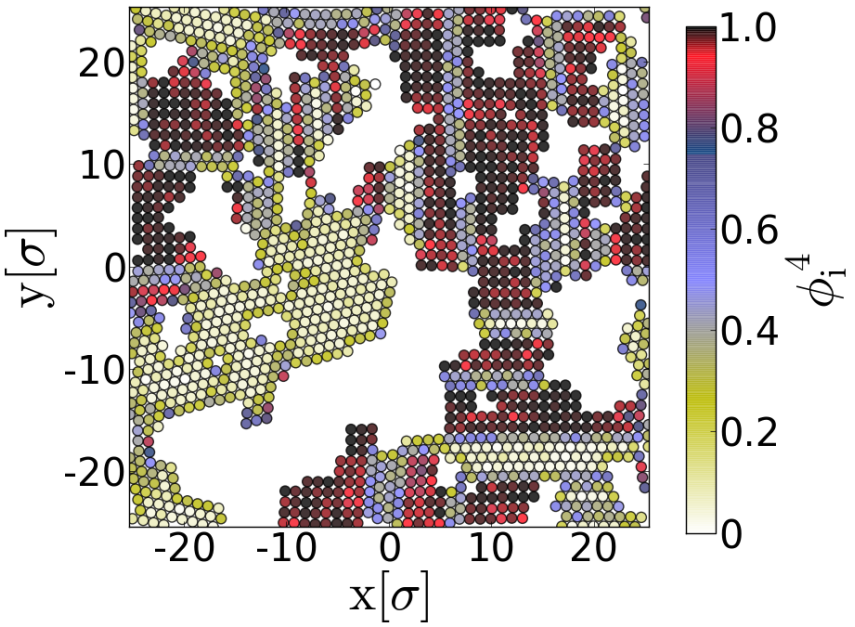

Figure 5.13: System at $T^* = 0.05$, density $\rho^* = 0.7$ and $\delta = 0.21\sigma$. The color-code gives the orientational bond-order parameter ϕ_i^4 of each particle i.

terized by either square-like order or hexagonal order. We note that, at $\delta = 0.21\sigma$, simultaneous appearance of clusters with both types of order also occurs at low densities and higher temperatures (see section 5.2.5). However, at the high density considered here the regions of each type are larger and the particle arrangements are much more regular (i.e., there are less defects).

To better understand the impact of the density on the cluster structures we plot in Fig. 5.14(a) the orientational bond order parameters Φ_4 and Φ_6 as functions of ρ^* for $\delta = 0.21\sigma$ (at $\delta = 0.1\sigma$ and $\delta = 0.3\sigma$ the order parameters are essentially independent of the density).

From Fig. 5.14(a) it is seen that the amount of rectangular (hexagonal) order sharply increases (decreases) at a density of $\rho^* \approx 0.45$. This is a surprising result as one would expect that, upon compressing the system, close-packed, hexagonal structures rather become more likely. However, at the low temperature considered here, structural reorganization is strongly hindered.

We also note that *all* of the systems investigated at densities $\rho^* > 0.45$ turned out to be percolated (suggesting that the value $\rho^* = 0.45$ is indeed related to the percolation transition). It thus seems that the percolation tends to stabilize the initially formed square-lattice symmetry, as the subsequent reorganization is hindered by the lack of mobility. In effect, we are faced with quenched states that could

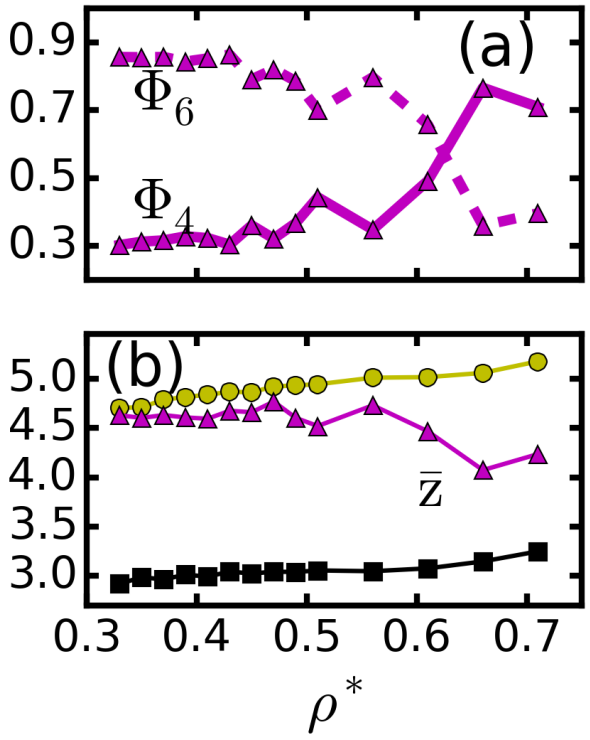

Figure 5.14: (a) Orientational bond order parameter Φ_4 and Φ_6 as function of density ρ^* for $\delta = 0.21\sigma$ at $T^* = 0.05$. (b) Mean coordination number $\bar{z}$ as function of ρ^* at $T^* = 0.05$ for different $\delta = 0.1\sigma, 0.21\sigma$ and 0.3σ colored in yellow, purple and black, respectively.

not density within the time domain studied. This interpretation is also consistent with the decrease of the mean coordination number once the system is percolated ($\rho^* > 0.45$) as shown in Fig. 5.14(b).

5.3 Small and Large-Scale Structures

In this final section we discuss the connection between our findings on field directed network formation in simulation studies of the extended dipole particle model (EDP) and the crossed dipole particle model (CDP). To this end, we first want to mention the visual similarity between the aggregates found in simulations of the EDP model in its rectangular regime (see Fig. 5.15(a)) and the *large scale* structures found in experiment (see Fig. 5.15(b)). However, it is clear that the *local* structures differ strongly between these two cases. Considering the CDP model, we find that it properly reproduces the *local* structure of the true experimental network structures as shown in Fig. 5.15 (c) and (d) and discussed (quantitatively) in Sec. 5.1.3. Hence, both models seem to be reasonable approaches towards a theoretical description of the real system, although on different length scales.

Interestingly, we found that the network structures formed by the CDP model undergo compactifaction by increasing the coupling strength. As discussed, from the ideal concept of diffusion limited aggregation the opposite behavior is expected, where an increase in the coupling strength results in less compact large-scale fractal aggregates [122]. However, it is not clear whether the observed compactifaction affects the fractal dimension on large length-scales. Our analysis was based on local properties, and the observed compactifaction is therefore a local one. Please note that it is well known that gels with long-ranged interactions and formed by a quench into the two-phase region undergo aging dynamics [114]. However, in this work we were investigating network structures at constant given times and it is not the temporal compactifaction which is discussed here. Revisiting the EDP model, we see that the *global* structure of the aggregates does not undergo compactifaction with increasing coupling strength, which is reflected in the constant values of the fractal dimension D_f by varying T^* (see Fig. 5.9(a)). Considering the *local* structure, which can be done via the mean coordination number $\bar{z}$, we find that structures become less compact with increasing coupling strength as $\bar{z}$ continuously decreases (see Fig. 5.9(b)). Hence, the EDP model behaves as it is expected from diffusion limited aggregation processes (but different than the CDP model).
The remaining question is why these models yield different behavior regarding compactifaction?

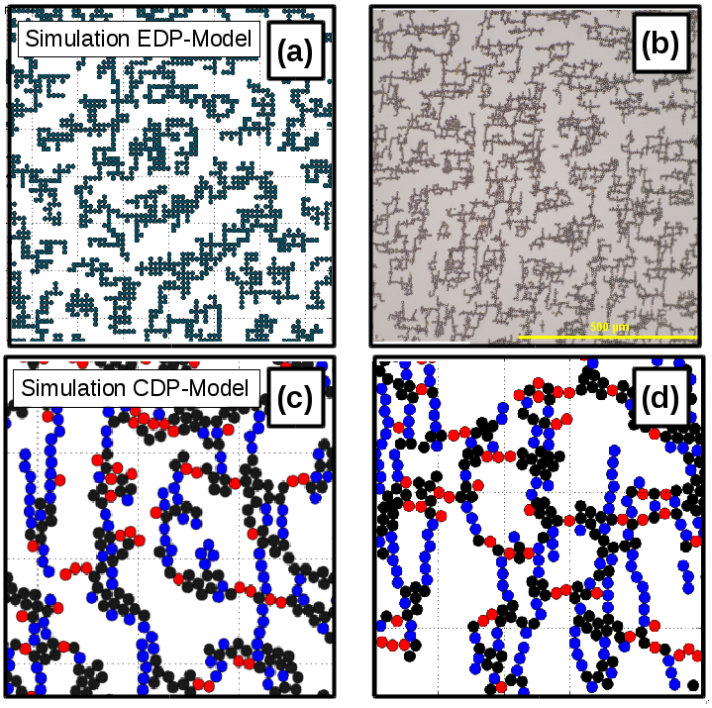

Figure 5.15: Small- and large-scale images of network structures in experiment and Simulation. Large-scale image from (a) Simulation of the EDP-model at $\rho^* = 0.3$, $T^* = 0.05$ and (b) Experiment at field strengths $E = 20V/mm, H = 90A/m$. Local network structures in (c) Simulation of the CDP-Model at $\rho^* = 0.35$, $\mu^{el} = \mu^{mg} = 0.4$ and (d) microscopic image at the same conditions as in (b). Particles in (c) and (d) are color-coded according to the method introduced in Sec. 3.5

Unfortunately, a general answer to this question can not be given here. Nevertheless, the following arguments and interpretations might provide an explanation, although a somewhat speculative one.

5.3.1 Strange compactifaction - A hybrid of anisotropic and slippery DLA?

The EDP model undergoes either anisotropic or slippery diffusion limited aggregation depending on the interaction anisotropy parameter δ (at strong coupling strengths $\lambda > 10$ or low temperatures $T^* \leq 0.2$). The transition between these aggregation regimes is very steep and solely controlled by δ. This is because the EDP model forms an one-component system of identical particles. In case the charge separation δ would be different for different particles, one would expect a different behavior. For example, if δ is distributed around the hexagonal-square transition parameter $\delta_{hex}^{sq} \approx 0.21\sigma$, some particles would clearly prefer rectangular arrangements, while other ones would prefer hexagonal arrangements. Building on our previous analysis, this means that some particles will form slippery bonds with their nearest neighbors, while other particles form orientationally fixed bonds. Hence, the system should reveal an *hybrid* aggregation process composed of anisotropic *and* slippery DLA. This means, that locally one could observe slippery DLA as well as anisotropic DLA, depending on the actual particles one is looking at. However, on large length-scales, it is uni-directional chains along one of the fields, which are the dominant structural elements. Inside the chains bond rotations are strongly suppressed, because such bond rotations involve massive structural reconfigurations and even bond-breaking events. For example, two particles connected by a slippery bond and forming a chain which is connecting two compact aggregates can only rotate around each other if either the chain breaks, or the aggregates move against each other. Hence, on larger length-scales the system should look like anisotropic DLCA.

However, one might expect that for stronger interaction energies these two particles might be able to induce or guide the motion of larger aggregates, bend the chain and maybe form more compact structures.

Coming back to the crossed dipole particle (CDP) model we find indeed a similar situation. The 'energy landscapes' for two *random* realizations of particles with randomly shifted magnetic moments are shown in Fig. 3.4 and reveal different interaction patterns. In a many particle system (simulation), various pairings of particles with different interaction patterns will be present. Therefore the CDP model

corresponds in principle to a multicomponent system, similar to the EDP-model variation discussed above. The irregular assembly of magnetic chains (see Fig. 5.1(c)) results from that multi-component character. This becomes obvious when comparing the magnetically assembled chains with the linear electrically assembled chains.

In consequence, it appears to us that the observed local compactifaction behavior with increasing interaction strength results from the 'multicomponent' character of the system. The underlying aggregation mechanism can be interpreted as a hybrid of slippery and anisotropic diffusion limited aggregation. While the EDP-model serves as a conceptional model which allows to identify the influence of anisotropic pair interactions on diffusion limited aggregation, it is not able to capture (in its present status) all features of the true system. Still, it allows to interpret them.

5.4 Summary

In this Chapter we presented the computer simulated aggregation of complex superparamagnetic colloids in *crossed* external fields. A detailed comparison between experiments and simulations of crossed dipole particle (CDP) model introduced in Sec. 3.4 was performed and yielded surprisingly similar structures. This analysis was done by a simple but powerful method previously introduced in Sec. 3.5. The central result of this section was a state diagram for the aggregation behavior under various field conditions but constant density. Our simulations revealed, that the system undergoes counter-intuitive local compactifaction by lowering the temperature and demonstrated the usefulness of using computer simulations as supporting tools for understanding experiments, where certain parameters (here the number density) can not be controlled properly.

In addition to the CDP model, our theoretical study of the extended dipole particle (EDP) model focused on understanding the formation of *transient* aggregates at low-temperatures. Performing large-scale BD simulations we found that, depending on the patchiness of particles (which is governed by the distribution of the field-induced attractive "sites" in the particles) different aggregation mechanisms arise. These have been analyzed via appropriate structural order parameters, bond time-correlation functions as well as by the fractal dimension. Our BD results demonstrated that by varying the patchiness of pair interactions, that is, the distribution of attractive sites, the systems transform from DLCA (essentially rigid bonds) towards sDLCA (slippery bonds). Moreover, we showed that the change of aggregation behavior is accompanied by significant changes of the local cluster structure.

Indeed, the cluster structure can be easily manipulated by exploiting the interplay between temperature, density and model parameter δ. This allows formation of unexpected structures e.g., pronounced rectangular packing instead of closed packed hexagonal structures by increasing density. This unusual behavior appears to be dictated by the inability of the originally formed lattices with hexagonal symmetry to rearrange into less dense square lattices.

Finally, the two models were compared with respect to the small and large-scale structures they form. The local compactifaction of network structures with decreasing temperature was then interpreted as a hybrid of slippery and anisotropic diffusion limited aggregation although these final comments remained speculative and further studies are needed for definite conclusions.

6

Conclusion and Outlook

In this work, we have used computer simulations to study the non-equilibrium self-assembly of complex colloidal particles with field induced dipolar interactions. The actual systems investigated are motivated by recent experimental observations in quasi two-dimensional setups of colloids confined to a surface. Theoretical models for the experimental particles and systems have been developed and compared to results from experiments. But also more generic models have been designed to allow insights into the underlying mechanisms of the colloidal assembly.

After giving a general introduction to non-equilibrium colloidal systems and presenting in detail two experimental examples in Chapter 1, we briefly reviewed some basic theoretical descriptions of simple fluids in Chapter 2. Special attention was paid to the concept of phase separation.

In Chapter 3 we then developed and discussed four different models for the two experimental systems presented in Chapter 1. To this end, we used 'energy landscapes' to represent two-particle interaction patterns, which allows an intuitive understanding of the complex dipolar character of our models. Furthermore, we took advantage of the basic symmetry of the dipole-dipole interaction and introduced an method to analyze colloidal networks on a single particle level. This method was exemplary applied to an experimental and a simulated network structure and turned out to be a simple but powerful tool.

In this method, two decoupled types of fictitious dipole moments are associated with each particle and are used to calculate fictitious energy spectra of the considered structures, which allows a proper characterization of the systems state. Furthermore, the energy spectra allow to identify for each particle the 'role' it is playing inside the network, which is either an edge or a node. Given this information it is in principle possible to deduce the adjacency matrix of the colloidal networks. From a mathematical point of view, this means that the topological properties of the network become accessible [158] and it is an interesting question how true physical properties (e.g., thermal and electrical conductivity) are related to topological properties (e.g., scale freeness or bipartiteness and of course percolation). Although designed to analyze rectangular real space network structures in two-dimensions this method can be extended towards other types of structures, which do not necessarily correspond to Bravais lattices i.e., non-Bravais clusters as formed by the dipolar Janus-particles and described in Sec. 4.2.1.

In the following Chapters we investigated the self-organization and self-assembly processes of the different particle models by means of Brownian dynamics computer simulations, basic concepts of density functional theory and heuristic theoretical considerations.

Lane formation of dipolar microswimmers

In Chapter 4 we investigated a system of colloidal microswimmers under the presence of an external electric field. The experimental setup motivating this work has been introduced in Sec. 1.2.4. The complex model used for this study is a double dipolar Janus particle with two induced dipole moments of different strengths and an orientation ally fixed propulsion direction (see Sec. 3.2). In a two-dimensional setup this means that the system is effectively binary; there exist two particle species with opposite orientations and propulsion directions. Such configurations are generally assumed to undergo lane formation if the propulsion force is strong enough. We have shown that this is indeed the case for our dipolar model and that the induced dipolar interactions stabilize the formation of lanes over a wide range of interaction strengths. This is surprising, as the anisotropic interactions show a strong tendency of the particles to self-assemble into chains which, in the present model, are oriented *perpendicular* to the driving force. These self-assembly processes result in complex staggered chains, when no driving force is present and the observed structures are in qualitative agreement with experimental observations. The underlying mechanisms for lane forma-

tion were then identified by investigating a simple binary Lennard-Jones fluid with oppositely driven particle species. Here, the onset of lane formation is closely related to the phase separation of the corresponding , well known, equilibrium system. By simple theoretical considerations we could also estimate the spinodal point in the double dipole model and show that the same connection is present there. Importantly, the (effective) attractiveness of the particle interactions in both models enables the system to undergo lane formation at propulsion speeds approximately one order of magnitude smaller than in previously known systems [91]. In addition, the presence of attractive interactions can also suppress lane formation. Using force balance arguments, the breakdown of lane formation due to 'freezing' was estimated in very good agreement with the simulation results. Finally, our observation of lane formation should be directly measurable in real systems of field-propelled metallo-dielectric particles, for which the model has been designed.
Starting from the present study, there is several further intriguing questions to be explored.

Outlook on lane formation

The model we were investigating contains several parameters, the dislocation of the dipole moments δ and the ratio between the dipole strengths μ^1/μ^2 which have not been varied systematically. As the values chosen in this work are 'educated guesses' but have not been derived quantitatively from microscopic particle properties, it would be of interest to investigate their influence on the lane formation process. Importantly, the dipole moments are symmetrically shifted out of the particle center. Decreasing the shift parameter δ strongly influences the anisotropy of interactions and increases the systems tendency to form chains perpendicular to the drive, as test simulations revealed. At smaller dipole shifts, the competition between lane formation and (perpendicular) chain formation should be more pronounced and the internal structure of lanes might be tuned.

Importantly, as the intra lane structures serve as 'backbones' of lanes, tuning these structures would most probably affect the width of lanes. Unfortunately, it is and remains unclear whether there exists a characteristic lane width at all. It would be of great interest to answer this question. Due to the more pronounced competition between laning and chaining it might become possible to quantify lane widths.

Also, is the behavior observed here related to a Raleigh-Taylor (RT) instability occurring in driven, macroscopically phase-separated

mixtures? In the context of RT, the critical wavelength [159] can be estimated by a simple criterion involving the surface tension between the phases; this might provide an additional way to quantify the lane width of our system and in general.

Our results on lane formation in attractively interacting systems may open up the door towards a deeper understanding of the laning transition as they show that laning in systems with attractive interactions is intimately related to phase separation, irrespective of the detailed form of the interaction potential. In recent years, the study of pseudo-phase separation processes in 'classically self-propelling' systems, where the propulsion direction is subject to rotational diffusion, has become a very lively field of research [69, 16, 58]. Especially hard sphere systems, which do not undergo phase separation in equilibrium, undergo a separation process into high and low density pseudo-phases if the propulsion forces are strong enough. A deeper understanding of this process is based on mimicking the influence of self-propulsion by an effectively attractive potential [69]. Interestingly, adding attractive interactions to the active hard-sphere system can enhance as well as suppress pseudo-phase separation [70, 71] similar to the effect on lane formation presented here. And the same behavior has also been reported for driven magnetic mixtures [42]. Obviously, it would be of major interest to have a general theory for pseudo-phase transitions in active systems, which, as our study indicates, should then connect pseudo-phase transitions to true equilibrium phase transitions in a conceptional way. A promising approach towards such an understanding might be based on the driven Lennard Jones fluid. This simple system allows large scale computer simulations which can be accompanied by standard methods from (dynamical) density functional theory. First studies using such techniques have been performed [91, 42] on soft-sphere systems. However, the (binary) Lennard Jones system presented here has not been investigated so far, but may serve as a generic model. In fact, in collaboration with Christopher Wächtler and Sabine H. L. Klapp at TU Berlin, an extensive study on lane formation in the binary driven Lennard-Jones fluid has been performed and will be published soon [160].

Accordingly, we expect our findings to be transferable to other driven colloidal systems with direction-dependent interactions, examples being "patchy" particles which, similar to our system, display both equilibrium aggregation *and* condensation [103], or dipolar colloids under shear flow [43]. In this context it is an interesting question whether lane formation can be interpreted as a *directed* spinodal decomposition. Here, an effective Cahn Hillard theory might be a reasonable approach [75]. The latter then would

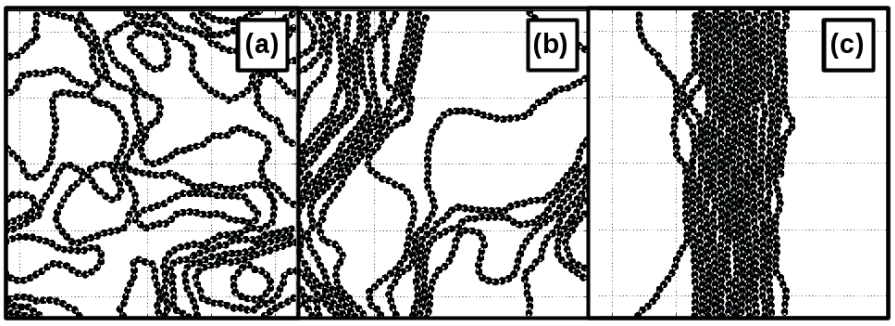

Figure 6.1: Simulation snapshots at $\rho^* = 0.3$, $T^* = 1$ and $\mu^* = 3.5$ for driving forces (a) $f_d^* = 1$, (b) $f_d^* = 3$ and (c) $f_d^* = 5$. Brighter dots in particles indicate the particle orientation.

raise again the question about dynamical characteristic length scales (lane widths) usually found in decomposing systems.

Finally, we shortly want to propose an interesting model system for an active dipolar fluid or one might call it an active ferrofluid. In experiment, self-propelling Janus Particles (e.g., metal coated) are often activated by light or localized chemical reactions [53, 52, 16]. Then the propulsion direction is fixed to the particle orientation, which itself is subject to rotational diffusion. Additionally, the metal-coated surface part might be made of a magnetic material e.g., iron oxide. Hence, a system of active magnetic/dipolar particles is realized and applying an external magnetic field should in principle allow to orientate these particles and their propulsion directions as the propulsion direction is fixed with respect to the particle body. Starting from the soft-sphere dipole fluid [22] (soft-sphere particles with centered dipole moments $\boldsymbol{\mu}_i$), one possibility of modeling activity is to associate a driving force $\mathbf{f}_i = f_i \boldsymbol{\mu}_i / \mu_i$ with each particle i. Thus, the particle moves along its dipole moment, although other geometries are also of interest. In fact, we performed two dimensional test simulations allowing the dipoles to rotate in three dimensions according to the equations of motion for a dipolar particle with constant propulsion force f_d and interaction potential $U_i = \sum_{j=1}^{N} U_{SS}(\mathbf{r}_{ij}) + U_{dip}(\mathbf{r}_{ij})$ (see Eq. [3.6])

$$\dot{\mathbf{r}}_i = -\frac{D^T}{k_B T} \nabla_i U_i + f_d \frac{\boldsymbol{\mu}_i}{\mu_i} + \zeta_i^T \tag{6.1}$$

$$\dot{\boldsymbol{\mu}}_i = -\frac{D^R}{k_B T} (\boldsymbol{\mu}_i \times \nabla_{\boldsymbol{\mu}_i} U_i) + \zeta_i^R \tag{6.2}$$

with rotational and translational diffusion coefficients D^R and D^T and white noise fulfilling the Eqs. [2.5,2.6]. In Fig. 6.1, we show

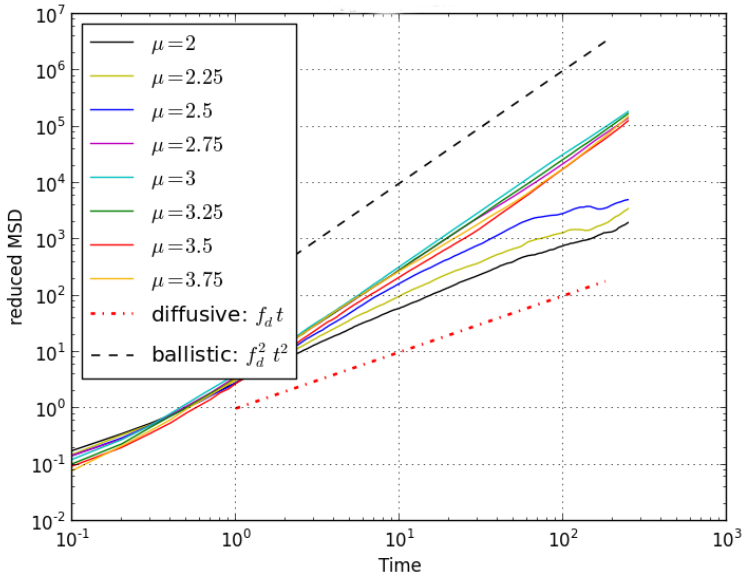

Figure 6.2: Mean square displacement in the active dipole fluid at $\rho^* = 0.6$, $T^* = 1$ and $f^* = 2$ for different dipole strengths.

simulation snapshots at constant density and dipole strength for different driving forces.

The overall scenario these test simulations indicate is the following. Given the dipolar coupling is strong enough, the self-propulsion enhances the systems ability to form a quasi-ferromagnetic state, where dipole moments mostly point in the same direction. Furthermore, this transition enhances the diffusion properties and allows the system to be super-diffusive in the long-time limit. Corresponding results showing the mean square displacement [134] for different dipole strengths are shown in Fig. 6.2. Despite the details of this transition, we want to note that in equilibrium there is no ferromagnetic transition of the two-dimensional dipole fluid [22]. The general interest of this system is given by its connection to various other model systems. On the one hand, it yields an alignment mechanism similar to the Vicsek-model [59, 57] (which also shows the motility induced ferromagnetic transition) but it is based on true physical interactions (steric and dipole-dipole interaction). On the other hand, it is closely connected to non-equilibrium structure formation of dipole fluids as it can be tuned by external fields. In general, external fields allow a tremendous variety of structure formation in passive dipole fluids, e.g., chaining [2] or layering [41]. The interplay between these phenomena and active motion most probably opens the door towards a new field of research concerned with tunable active dipole fluids.

Field directed aggregation

The effect of anisotropic pair interactions on colloidal self-assembly processes is itself an interesting question and in Chapter 5 a system of double dipolar (patchy) particles has been investigated. The corresponding experimental setup and the observed self-assembled structures have been introduced in Sec. 1.3.3 and a paper publication is preparation [161].

Here, the assembly of chain and network structures under the presence of crossed magnetic and electric fields was tunable by the respective field strengths. Importantly, it is not Janus particles which were considered here, but polymer particles with an unknown internal distribution of superparamagnetic (nanometer scale) iron-oxide aggregates. Again, a complex model (CDP-model) with explicit dipole-dipole interactions has been developed in Sec. 3.4. The model is based on the assumption that different particles carry different amounts of magnetic material and that the distribution of the magnetic material inside the particles is not homogenous but rather characterized by an off-centered effective magnetic interaction site. Based on a new and rather simple method to analyze colloidal networks, a detailed comparison of simulated and experimental colloidal aggregates was performed. The simulated structures turned out to be in surprisingly good agreement with the experimental ones. A precise control of the local and global density was not possible in experiment and no clear understanding of the non-equilibrium state diagram at different external field strengths could be established. The advantage of the theoretical approach was that it allowed to close this gap in the experimental understanding. Simulations revealed that at fixed intermediate density there exist in principle four different states, corresponding to magnetic and electric field aligned string fluids and fine and coarse colloidal networks. The main result here is the non-equilibrium state diagram from simulation and the newly developed method to characterize colloidal networks. We found that there exists a smooth crossover from fine to coarse networks by increasing both field strengths, which could not be explained at this point. It also remained unclear whether these network states do undergo gelation. This is mostly due to computational reasons because the analysis of the prerequisites of gelation, namely very slow relaxational dynamics and percolation, requires very long simulation times and large particle numbers (finite size scaling). Such procedures were not feasible with this model.

In addition, a generic model (EDP model) with tunable directionality of effective dipole-like interactions was developed in Sec. 5.2. In an extensive study of its aggregation behavior we investigated the

influences of temperature and of the 'degree' of patchiness of pair interactions. The focus of the study of the generic model was to understand the formation of *transient*, aggregated structures appearing at low-temperatures. Performing large-scale BD simulations we have found that, depending on the patchiness of particles, which is governed by the distribution of the field-induced attractive "sites" in the particles, different aggregation mechanisms arise. These have been analyzed via appropriate structural order parameters, bond time-correlation functions as well as by the fractal dimension. Our BD results demonstrate that by varying the charge separation parameter, that is, the distribution of attractive sites, the systems transform from DLCA (essentially rigid bonds) towards sDLCA (slippery bonds). Moreover, we show that the change of aggregation behavior is accompanied by significant changes of the local cluster structure. Based on our understanding of these *ideal* aggregation regimes of a *one component* system, we interpret the strange compactifaction observed on the local scale in CDP model as a *hybrid* of slippery and anisotropic DLA in a *multi component* system.

Outlook on field directed aggregation

Although this interpretation remains somewhat speculative, as discussed in Sec. 5.3, we assume that it can be tested by introducing a random distribution of the shift parameter δ in the generic model such that different particles have different charge separations. This will most probably result in a smoother transition between the hexagonal and rectangular regime and lead to a situation, where rectangular chaining and branching persist while the local order is already hexagonal and the generic (EDP) model could be related much more closely to the complex (CDP) model. Then, its computational and conceptional advantages could be exploited more efficiently. For example, it remained an open question whether the system undergoes gelation. Computationally it should be possible to determine the percolation transition and characterize the relaxational dynamics in the generic model. These results should then be transferable to the complex model and to the real system. Besides, it remains an open question whether it is the range of interactions which governs the compactifaction process. Finally, having access to large-scale network structures allows to extract topological information (adjacency matrix of the underlying graph) via the structure analysis method discussed above. A large zoo of potentially interesting correlations emerges here. For instance, the interplay between fractal dimension and graph connectivity [158].

From a technological point of view the presented multi-directional

field approach yields strong potential for the design of adjustable materials. In fact, the cluster structures can be easily manipulated (except of particle density) by exploiting the interplay between different fields of different strengths and orientations. This allows formation of unexpected structures e.g., pronounced rectangular packing instead of closed packed hexagonal structures by increasing density, as observed in the generic model.

It has potentially important consequences for colloidal assembly, as is points out the ability to use mutidirectional field-driven assembly for the making of lower-density, yet highly interconnected, phases. The formation of particle networks with multiple percolation directions can find application in a range of new materials with anisotropic electrical and thermal conduction, magnetic or electric polarizability or unusual rheological properties. The aggregated clusters can be dispersed in liquid, while the percolated networks can be embedded in a polymer or gel medium [162]. The key to the fabrication of such novel classes of materials containing particle clusters and networks is the control of the process parameters to obtain the desired inter-connectivity, density and structure. In addition, the general setup allows also to change the angle between the electric and magnetic field which should result in new interaction patterns and exotic structures. Future research should also focus on a more detailed investigation of the interplay between the aggregation mechanisms observed here (anisotropic and slippery DLCA), and the *equilibrium* phase behavior, particularly the location of a condensation transition. This includes investigation of the influence of entropy which we did not discuss but may strongly influence the aggregation behavior [163]. Furthermore, connections to transient and directional cluster formation mediated by DNA-links [164], long-ranged repulsion [165], anisotropic particle shapes [10, 1, 12] or other non-equilibrium mechanisms such as activity [68, 166] and/or hydrodynamics [167] are of interest.

In this work, two types of non-equilibrium processes have been considered, namely 'Hit and Stick' aggregation and lane formation, which are characterized by strong anisotropic interactions and self-propulsion, respectively. The combination of these particle properties is a next step towards colloidal systems of increased complexity. Such systems might result in a 'super-diffusion limited aggregation' process, meaning that particles are able to self-propel *and* to undergo field directed aggregation. By now, 'Hit and Stick' aggregation of ballistically moving particles has been considered [117, 118], but the interplay of self-propulsion and 'Hit and Stick' aggregation remains an open question. However, our findings on lanes formed by dipolar microswimmers point in this direction.

Appendix

Brownian Dynamics Computer Simulations

The solutions of Eqs. [2.12,2.13] are the trajectories of the colloidal particles. However, an analytical solution for a many particle system is in general not possible. An alternative is to integrate Eqs. [2.12,2.13] numerically; a procedure which is usually called Brownian dynamics (BD) computer simulation [134, 135].

Numerical Integration

The overdamped Eqs. [2.12,2.13] are of first order which allows to use the Euler integration-scheme [134, 135]. Throughout this work, directional pair interactions with fixed orientations have been considered. Therefore, torques and rotational motion of particles has not been calculated. For completeness we present here the full solution of the translational and rotational equations of motion. The numerical integration of Eqs. [2.12,2.13] then reads

$$\mathbf{r}_i(t+\Delta t) = \mathbf{r}_i(t+\Delta t) + \frac{D^T}{k_B T}\mathbf{F}_i \Delta t + \tilde{\mathbf{F}}_i^D \tag{6.3}$$

$$\mathbf{e}_i(t+\Delta t) = \mathbf{e}_i(t) + \frac{D^R}{k_B T}\mathbf{T}_i \Delta t \times \mathbf{e}_i(t) + \tilde{\mathbf{T}}_i^D \times \mathbf{e}_i(t), \tag{6.4}$$

with an integration step width Δt and orientational unit vectors $\mathbf{e}_i(t)$. In this numerical integration scheme, the stochastic contributions $\tilde{\mathbf{F}}_i^D$ and $\tilde{\mathbf{T}}_i^D$ obey again Gaussian distributions with mean

$$< \tilde{\mathbf{F}}_i^D(t) >= 0 \tag{6.5}$$

$$< \tilde{\mathbf{T}}_i^D(t) >= 0 \tag{6.6}$$

and with variance

$$< \tilde{\mathbf{F}}_i^D(t) \cdot \tilde{\mathbf{F}}_j^D(t+\Delta t) >= 2D^T \delta_{ij} \Delta t \mathbb{1} \tag{6.7}$$

$$< \tilde{\mathbf{T}}_i^D(t) \cdot \tilde{\mathbf{T}}_j^D(t+\Delta t) >= 2D^R \delta_{ij} \Delta t \mathbb{1}. \tag{6.8}$$

The forces and torques $\mathbf{F}_i$ and $\mathbf{T}_i$ are stemming from interactions with other colloidal particles or might result from external potentials e.g., an electric field exerting the force $\mathbf{F}_{ext}$ and torque $\mathbf{T}_{ext}$) on particle i. Therefore the total force and torque on particle i due to all other particles ($j \neq i$) is given by the superposition of the forces $\mathbf{F}_{ij}$ and torques $\mathbf{T}_{ij}$ imposed on particle i by the particles j

$$\mathbf{F}_i = \Sigma_{j=1}^{N} \mathbf{F}_{ij} + \mathbf{F}_{ext}. \tag{6.9}$$

$$\mathbf{T}_i = \Sigma_{j=1}^{N} \mathbf{T}_{ij} + \mathbf{T}_{ext} \tag{6.10}$$

whereas N is the number of particles in the system.

Accordingly, their calculation (in a computer simulation) requires knowledge about the pair interactions between two specific colloids. In fact, these interactions define the colloidal models and important examples have been considered in Sec. 3.1.

Importantly, in case the pair interactions are long-ranged special methods have to be utilized to overcome difficulties related to the periodic boundary conditions and computational efficiency.

Long-range interactions

In single particle resolved computer simulations, pair interactions are calculated for particle separations smaller than a certain, interaction dependent, cut-off distance r^c. Under periodic boundary conditions, this cut-off has to be smaller than half the size of the central simulation box. However, there are certain types of interactions which decay very slow with the particle separation: Examples for such long-ranged interactions are the Coulomb potential or the dipole-dipole interaction. Hence, these potentials cannot be simply truncated because otherwise major errors would be introduced. In the following we present a common approach to handle this difficulty via the Ewald-summation method.

Ewald summation of the Coulomb potential

In this section we introduce the Ewald summation technique for ionic systems in three dimensions, which then will allow a straight forward generalization for dipolar systems in the next section. Thereby we follow closely the derivation of Klapp and Schön in [150]. A detailed review of special aspects of the two-dimensional Ewald summation is found in [144].
The pair-interaction $U_{cou}(r)$ between two charged particles is given

by Eq. 3.4. By scaling prefactors into the charges q, the total energy due to the Coulomb interaction between N particles is given by

$$U_c = \frac{1}{2}\sum_{i=1}^{N} q_i \Phi(\mathbf{r}_i) \quad \text{with} \quad \Phi(\mathbf{r}_i) = \sum_{j=1}^{N} \frac{q_j}{|\mathbf{r}_i|}. \tag{6.11}$$

In the following we assume that the system is neutral, meaning that $\sum_{i=1}^{N} q_i = 0$, and that it is a three dimensional bulk system constructed of a (cubic $V = L^3$) central simulation cell of size L with periodic boundary conditions. The later condition allows to write the electrostatic potential as

$$\Phi(\mathbf{r}_i) = \sum_{\{\mathbf{n}\}}{}' \sum_{j=1}^{N} \frac{q_j}{|\mathbf{r}_{ij} + \mathbf{n}|}, \tag{6.12}$$

with $\mathbf{r}_{ij} = \mathbf{r}_j - \mathbf{r}_i$ and $\{\mathbf{n}\}$ being the set of lattice vectors naming the periodic images of the central cell, meaning that $\mathbf{n} = (n_x, n_y, n_z)L$ with $n_\alpha \in \mathbb{Z}$. In the central cell, denoted by $\mathbf{n} = 0$, the contribution $j = i$ is excluded from the summation, which is indicated by the prime in the summation over $\mathbf{n}$ in Eq. 6.12. In this general setup we now derive the Ewald summation technique.
To this end, we consider the charge density $\rho_i(\mathbf{r})$ which is connected to the electrostatic potential $\Phi(\mathbf{r}_i)$ via Poisson's equation [142]

$$\Phi(\mathbf{r}_i) = \int d\mathbf{r}' \rho_i(\mathbf{r}') |\mathbf{r}_i - \mathbf{r}'|^{-1}. \tag{6.13}$$

The distribution of charges seen by particle i can be written a sum of delta-functions

$$\rho_i(\mathbf{r}') = \sum_{\{\mathbf{n}\}}{}' \sum_{j=1}^{N} q_j \delta(\mathbf{r}' - \mathbf{r}_j + \mathbf{n}). \tag{6.14}$$

Importantly, the decay of the potential Φ resulting from this charge density is rather slow (proportional to the inverse distance). Hence, also the lattice sum converges (for a given ordering) slowly. Furthermore, the sum is only *conditionally convergent*, meaning that the order of summation determines the result. The idea of Ewald summation is now to split the charge distribution $\rho_i(\mathbf{r}')$ into three parts $\rho_i^a(\mathbf{r}')$, $\rho_i^b(\mathbf{r}')$, $\rho_i^c(\mathbf{r}')$ which generate a electrostatic potential converging in a more favorable way. This is done by superimposing each δ-function in Eq. 6.14 with a continuous distribution of opposite point-charges q_j. Usually, one uses a Gaussian distribution

$$\rho_{j,\mathbf{n}}(\mathbf{r}') = -q_j(\alpha/\sqrt{\pi})^3 \exp\left[-\alpha^2(\mathbf{r}' - \mathbf{r}_j + \mathbf{n})^2\right]. \tag{6.15}$$

Here, α acts as a parameter controlling the width of the distribution, similar but inverse to the variance. The overall number of charges

in the system thereby increases because the artificially introduced distributions are normalized by

$$-q_j = \int d\mathbf{r}' \rho_{j,\mathbf{n}}(\mathbf{r}'). \tag{6.16}$$

Adding Eq. 6.15 to Eq. 6.14 results in the artificial charge density

$$\rho_i^{(a)}(\mathbf{r}') = \sum_{\{\mathbf{n}\}}{}' \sum_{j=1}^{N} q_j \delta(\mathbf{r}' - \mathbf{r}_j + \mathbf{n} + \rho_{j,\mathbf{n}}(\mathbf{r}')) \tag{6.17}$$

which can be interpreted as a density of 'screened' charges. The associated potential [150]

$$\Phi^{(a)}(\mathbf{r_i}) = \sum_{\{\mathbf{n}\}}{}' \sum_{j=1}^{N} q_j \mathrm{erfc}(\alpha|\mathbf{r}_{ij} + \mathbf{n}|)/|\mathbf{r}_{ij} + \mathbf{n}| \tag{6.18}$$

shows a much more rapid decay than $\Phi(\mathbf{r}_i)$, because of the monotonically decreasing complementary error function erfc(). Here, α controls the decay or screening. And indeed, the expression for $\Phi^{(a)}(\mathbf{r_i})$ reminds of the yukawa interaction, whereas the screening constant κ corresponds to α and the exponential decay is replaced by the erfc().

By now, we have artificially introduced further charges into system. Therefore we now reformulate the charge density $\rho_{j,\mathbf{n}}(\mathbf{r}'))$ of these fictitious charges to increase its convergence properties and add it later as an effectively negative charge density to $\Phi^{(a)}$. Hence, we will finally pertain the original setup. From Eq. 6.17 we see that

$$\rho_i(\mathbf{r}') - \rho_i^{(a)}(\mathbf{r}') = -\sum_{\{\mathbf{n}\}}{}' \sum_{j=1}^{N} \rho_{j,\mathbf{n}}(\mathbf{r}') \tag{6.19}$$

where again the prime in the lattice sum indicates that the terms $i = j$ are excluded for $\mathbf{n} = 0$, which is also the reason why $\rho_i(\mathbf{r}')$ depends on i. Now we introduce the charge density

$$\begin{aligned} \rho^{(b)}(\mathbf{r}') &= -\sum_{\{\mathbf{n}\}} \sum_{j=1}^{N} \rho_{j,\mathbf{n}}(\mathbf{r}') \\ &= -\sum_{\{\mathbf{n}\}} \sum_{j=1}^{N} q_j \alpha^3 \sqrt{\pi}^{-3} \exp[-\alpha^2(\mathbf{r}' - \mathbf{r}_i + \mathbf{n})^2]. \end{aligned} \tag{6.20}$$

Note that the lattice sum is carried out here without any restrictions (no prime). Therefore $\rho^{(b)}(\mathbf{r}')$ is independent of i and periodic in space and contains the contribution from the central cell

($i = j$ when $\mathbf{n} = 0$). The later is given by

$$\rho_i^{(c)}(\mathbf{r}') = \rho_{i,0}(\mathbf{r}') = -q_i \alpha^3 \sqrt{\pi}^{-3} \exp[-\alpha^2(\mathbf{r}' - \mathbf{r}_i)^2]. \tag{6.21}$$

This is an important difference to the right hand side of Eq. 6.19, and allows the charge density $\rho^{(b)}(\mathbf{r}')$ to be calculated in reciprocal space. The later is spanned by the lattice vectors

$$\mathbf{k} = 2\pi/L(m_x, m_y, m_z) \quad \text{with} \quad m_\alpha \in \mathbb{Z}. \tag{6.22}$$

It can be shown [150] that the (discrete) Fourier transform of the charge density $\rho^{(b)}(\mathbf{r}')$ results in the potential

$$\Phi^{(b)}(\mathbf{r}_i) = \frac{4\pi}{V} \sum_{\mathbf{k}\neq 0} \sum_{j=1}^{N} \frac{q_j}{k^2} \exp[-k^2/4\alpha^2] \exp[-i\mathbf{k}\cdot\mathbf{r}_{ij}] + \Phi_{LR}^{(b)}(\mathbf{r}_i). \tag{6.23}$$

The term $\Phi_{LR}^{(b)}(\mathbf{r}_i)$ is the contribution for zero wave vectors $\mathbf{k} = 0$ and given by

$$\Phi_{LR}^{(b)}(\mathbf{r}_i) = 4\pi/(V(2\epsilon' + 1)) \sum_{j=1}^{N} q_j \mathbf{r}_i \cdot \mathbf{r}_j \tag{6.24}$$

if the system is seen as a large sphere surrounded by a dielectric continuum with dielectric constant ϵ'. The advantage of this representation is, that damping is controlled by the wave-number $k = |\mathbf{k}|$ and sufficient convergence is already achieved for relatively small wave-numbers $k \approx 20 - 30$ if α is chosen in such a way, that only the central simulation cell $\mathbf{n} = 0$ has to be evaluated in $\Phi^{(a)}(\mathbf{r}_i)$ (see Eq. 6.18).
The potential according to $\rho_i^{(c)}(\mathbf{r}')$ compensates for the unphysical self-interaction hidden in $\Phi^{(b)}(\mathbf{r_i})$ and is given by [150]

$$\Phi^{(c)} = -q_i 2\alpha/\sqrt{\pi}. \tag{6.25}$$

At this point, we have split up the original electrostatic potential $\Phi(\mathbf{r}_i)$ (see Eq. 6.12) into various contributions with controllable convergence properties. Making use of Eq. 6.11 allows to write down the corresponding parts of the Ewald potential energy U_{cou}^{EW} as:

· the contribution from real space

$$\begin{aligned} U_{cou}^{real} &= \frac{1}{2} \sum_{i=1}^{N} q_i \Phi^{(a)}(\mathbf{r}_i) \\ &= \frac{1}{2} \sum_{i=1}^{N} \sum_{\{\mathbf{n}\}}{}' \sum_{j=1}^{N} q_i q_j \frac{\operatorname{erfc}(\alpha|\mathbf{r}_{ij} + \mathbf{n}|)}{|\mathbf{r}_{ij} + \mathbf{n}|} \end{aligned} \tag{6.26}$$

· contribution from the Fourier sum

$$\begin{aligned} U_{cou}^{fourier} &= \frac{1}{2}\sum_{i=1}^{N} q_i[\Phi^{(b)}(\mathbf{r}_i) - \Phi_{LR}^{(b)}(\mathbf{r}_i)] \\ &= \frac{2\pi}{V}\sum_{i=1}^{N}\sum_{\mathbf{k}\neq 0}\sum_{j=1}^{N}\frac{q_i q_j}{k^2}\exp[-k^2/4\alpha^2]\exp[-i\mathbf{k}\cdot\mathbf{r}_{ij}] \end{aligned} \tag{6.27}$$

· contribution from long-range interaction

$$U_{cou}^{long} = \frac{1}{2}\sum_{i=1}^{N} q_i\Phi_{LR}^{(b)}(\mathbf{r}_i) = \frac{2\pi}{V(2\epsilon'+1)}|\sum_{j=1}^{N} q_j\mathbf{r}_i\cdot\mathbf{r}_j|^2 \tag{6.28}$$

· the contribution from self-interaction

$$U_{cou}^{self} = \frac{1}{2}\sum_{i=1}^{N} q_i\Phi^{(c)} = -\alpha/\sqrt{\pi}\sum_{i=1}^{N} q_i^2. \tag{6.29}$$

The total potential energy is then given by

$$U_{cou}^{EW} = U_{cou}^{real} + U_{cou}^{fourier} + U_{cou}^{long} + U_{cou}^{self}. \tag{6.30}$$

Ewald summation of the dipole-dipole potential

With this background, we are now able to formulate the Ewald sum for dipolar systems. Interestingly, the dipole-dipole potential U_{dip} (see Eq. 3.6) is related to the functional form of the Coulomb potential of a unit point charge

$$\Psi(r_{ij}) = r_{ij}^{-1} \tag{6.31}$$

via

$$U_{dip}(\mathbf{r}_{ij}, \boldsymbol{\mu}_i, \boldsymbol{\mu}_j) = (\boldsymbol{\mu}_i\cdot\boldsymbol{\nabla}_i)(\boldsymbol{\mu}_i\cdot\boldsymbol{\nabla}_j)\Psi(r_{ij}). \tag{6.32}$$

Formally, this means nothing more than replacing the charges q_γ in U_{cou} by the operators $\boldsymbol{\mu}_\gamma\cdot\boldsymbol{\nabla}_\gamma$ results in the dipole-dipole potential U_{dip}. Applying this transformation to the explicit expressions inin Eqs. 6.26, 6.27, 6.28 and 6.29 allows to write down the corresponding parts of the Ewald dipole-dipole energy U_{dip}^{EW} as:

· the contribution from real space

$$\begin{aligned} U_{dip}^{real} = \frac{1}{2}\sum_{i=1}^{N}{\sum_{\{\mathbf{n}\}}}'\sum_{j=1}^{N}&(\boldsymbol{\mu}_i\cdot\boldsymbol{\mu}_j)B(|\mathbf{r}_{ij}+\mathbf{n}|,\alpha) \\ &-[\boldsymbol{\mu}_i\cdot(\mathbf{r}_{ij}+\mathbf{n})][\boldsymbol{\mu}_j\cdot(\mathbf{r}_{ij}+\mathbf{n})]C(|\mathbf{r}_{ij}+\mathbf{n}|,\alpha) \end{aligned} \tag{6.33}$$

· the contribution from Fourier space

$$U_{dip}^{fourier} = \frac{2\pi}{V} \sum_{k \neq 0} \frac{1}{k^2} \exp[-k^2/4\alpha^2] F(\mathbf{k}) F^*(\mathbf{k}) \tag{6.34}$$

· the contribution from long-range interaction

$$U_{dip}^{long} = \frac{2\pi}{V(2\epsilon' + 1)} (\sum_{j=1}^{N} \boldsymbol{\mu}_i)^2 \tag{6.35}$$

The functions $B(|\mathbf{r}_{ij} + \mathbf{n}|, \alpha), C(|\mathbf{r}_{ij} + \mathbf{n}|, \alpha)$ and $F(\mathbf{k})$ are defined as:

$$B(|\mathbf{r}_{ij} + \mathbf{n}|, \alpha) = \frac{1}{r^3} [\frac{2\alpha r}{\sqrt{\pi}} \exp -\alpha^2 r^2 + \operatorname{erfc}(\alpha r)] \tag{6.36}$$

$$C(|\mathbf{r}_{ij} + \mathbf{n}|, \alpha) = \frac{1}{r^5} [\frac{2\alpha r}{\sqrt{\pi}} (3 + 2\alpha^2 r^2) \exp -\alpha^2 r^2 + 3\operatorname{erfc}(\alpha r)] \tag{6.37}$$

$$F(\mathbf{k}) = \sum_{i=1}^{N} (\boldsymbol{\mu}_i \cdot \mathbf{k}) \exp(-i\mathbf{k} \cdot \mathbf{r}_i). \tag{6.38}$$

The self-part of the dipolar Ewald sum does not follow directly by applying the transformation $q_\gamma \rightarrow \boldsymbol{\mu}_\gamma \cdot \boldsymbol{\nabla}_\gamma$. For details see Ref. [150].

$$U_{dip}^{self} = -\frac{2\alpha}{3\sqrt{\pi}} \sum_{i=1}^{N} \mu_i^2. \tag{6.39}$$

The total potential energy is then given by

$$U_{dip}^{EW} = U_{dip}^{real} + U_{dip}^{fourier} + U_{dip}^{long} + U_{dip}^{self}. \tag{6.40}$$

Ewald summation for quasi two-dimensional dipoles

Most of this work is concerned with the behavior of complex dipolar colloids at interfaces. Such quasi two-dimensional systems are treated by restricting translational motion to a plane of area $A = L^2$, while allowing the dipole moments to rotate in three dimensions. The Ewald summation for dipolar interactions has to be adapted to these geometrical restrictions. To distinguish between the three-dimensional and quasi two-dimensional cases, the lattice vectors of the Fourier contributions are denoted by $\mathbf{g} = 2\pi(m_x, m_y)L$ here, with m_x, $m_y \in \mathbb{Z}$. Specifically, the total energy can be split up in contributions [22, 144]

parallel

$$U_{dip}^{\parallel}(\mathbf{r}_{ij},\boldsymbol{\mu}_i^{\parallel},\boldsymbol{\mu}_j^{\parallel}) = -\frac{1}{2}\sum_{i,j=1}^{N}[B^{q2d}(r_{ij})\boldsymbol{\mu}_i^{\parallel}\cdot\boldsymbol{\mu}_j^{\parallel} + C^{q2d}(r_{ij})(\boldsymbol{\mu}_i^{\parallel}\cdot\mathbf{r}_{ij})(\boldsymbol{\mu}_j^{\parallel}\cdot\mathbf{r}_{ij})] + \frac{\pi}{A}\sum_{\mathbf{g}\neq 0}\frac{\mathrm{erfc}(g/2\alpha)}{g}F_{\parallel}(\mathbf{g})F_{\parallel}^{*}(\mathbf{g}) - \frac{2\alpha^3}{3\sqrt{\pi}}\sum_{i=1}^{N}|\boldsymbol{\mu}_i^{\parallel}|^2 \tag{6.41}$$

and perpendicular

$$U_{dip}^{\perp}(\mathbf{r}_{ij},\boldsymbol{\mu}_i^{\perp},\boldsymbol{\mu}_j^{\perp}) = -\frac{1}{2}\sum_{i,j=1}^{N}[B^{q2d}(r_{ij})\boldsymbol{\mu}_i^{\perp}\cdot\boldsymbol{\mu}_j^{\perp} + \frac{\pi}{A}\sum_{\mathbf{g}\neq 0}[\frac{2\alpha}{\sqrt{g}}\exp-\frac{g^2}{4\alpha^2} - g\mathrm{erfc}(g/2\alpha)]F_{\perp}^{q2d}(\mathbf{g})F_{\perp}^{q2d^*}(\mathbf{g}) - \frac{2\alpha\sqrt{\pi}}{A}\sum_{i,j=1}^{N}\boldsymbol{\mu}_i^{\perp}\cdot\boldsymbol{\mu}_j^{\perp} - \frac{2\alpha^3}{3\sqrt{\pi}}\sum_{i=1}^{N}|\boldsymbol{\mu}_i^{\perp}|^2 \tag{6.42}$$

to the plane, whereas $\boldsymbol{\mu}_{\gamma}^{\perp}$ and $\boldsymbol{\mu}_{\gamma}^{\parallel}$ denote the perpendicular and parallel components of dipole moment $\boldsymbol{\mu}_{\gamma}$, respectively.

(6.43)

The functions $B^{q2d}(|\mathbf{r}_{ij}+\mathbf{n}|,\alpha)$, $C^{q2d}(|\mathbf{r}_{ij}+\mathbf{n}|,\alpha)$ and $F_{\perp,\parallel}^{q2d}(\mathbf{g})$ are defined as:

$$B^{q2d}(|\mathbf{r}_{ij}+\mathbf{n}|,\alpha) = -\frac{\mathrm{erfc}(\alpha r)}{r^3} - \frac{2\alpha r}{\sqrt{\pi}}\frac{\exp-\alpha^2r^2}{r^2}] \tag{6.44}$$

$$C^{q2d}(|\mathbf{r}_{ij}+\mathbf{n}|,\alpha) = 3\frac{\mathrm{erfc}(\alpha r)}{r^5} + \frac{2\alpha r}{\sqrt{\pi}}(3/r^2+2\alpha^2)\frac{\exp-\alpha^2r^2}{r^2} \tag{6.45}$$

$$F_{\perp}^{q2d}(\mathbf{g}) = \sum_{i=1}^{N}\boldsymbol{\mu}_i^{\perp}\exp(i\mathbf{g}\cdot\mathbf{r}_i) \tag{6.46}$$

$$F_{\parallel}^{q2d}(\mathbf{g}) = \sum_{i=1}^{N}(\boldsymbol{\mu}_i^{\parallel}\cdot\mathbf{g})\exp(i\mathbf{g}\cdot\mathbf{r}_i). \tag{6.47}$$

In Brownian Dynamics computer simulations, it is not the interac-

tion energy but rather the forces

$$\begin{aligned} f_i^{q2d} &= -\nabla_{\mathbf{r}_i}(U_{dip}^{\parallel} + U_{dip}^{\perp}) \\ &= \sum_{j=1}^{N} {\sum_{\{\mathbf{n}\}}}' \{C^{q2d}(r_{ij})[(\boldsymbol{\mu}_i \cdot \boldsymbol{\mu}_j)\mathbf{r}_{ij} + (\boldsymbol{\mu}_i(\boldsymbol{\mu}_j \cdot \mathbf{r}_{ij}) + (\boldsymbol{\mu}_j(\boldsymbol{\mu}_i \cdot \mathbf{r}_{ij})] \\ &\qquad - D^{q2d}(r_{ij})(\boldsymbol{\mu}_i \cdot \mathbf{r}_{ij})(\boldsymbol{\mu}_j \cdot \mathbf{r}_{ij})\mathbf{r}_{ij}\} \\ &+ \frac{2\pi}{A} \sum_{\mathbf{g}\neq=0} \frac{\operatorname{erfc}(g/2\alpha)}{g}(\mathbf{g} \cdot \boldsymbol{\mu}_i^{\parallel})\mathbf{g} \\ &\qquad \times [\sin(\mathbf{g} \cdot \mathbf{r}_i)\mathrm{Re}N(\mathbf{g}) - \cos(\mathbf{g} \cdot \mathbf{r}_i)\mathrm{Im}N(\mathbf{g})] \\ &+ \frac{2\pi}{A} \sum_{\mathbf{g}\neq 0} [\frac{2\alpha}{\sqrt{\pi}} \exp(-g^2/4\alpha^2) - \operatorname{erfc}(g/2\alpha)g]\mathbf{g} \\ &\qquad \times [\sin(\mathbf{g} \cdot \mathbf{r}_i)\mathrm{Re}O(\mathbf{g}) - \cos(\mathbf{g} \cdot \mathbf{r}_i)\mathrm{Im}O(\mathbf{g})] \end{aligned} \tag{6.48}$$

which are or interest. Here we have defined the functions

$$\begin{aligned} D^{q2d}(r_{ij}) = \frac{1}{r_{ij}^7}[&\frac{2\alpha r_{ij}}{\sqrt{pi}}(15 + 10\alpha^2 r_{ij}^2 \\ &+ 4\alpha^4 r_{ij}^4)\exp(-\alpha^2 r_{ij^2}) + 15\operatorname{erfc}(\alpha r_{ij})] \end{aligned} \tag{6.49}$$

$$N(\mathbf{g}) = \sum_{j=1}^{N} (\mathbf{g} \cdot \boldsymbol{\mu}_j^{\parallel}) \exp(i\mathbf{g} \cdot \mathbf{r}_j) \tag{6.50}$$

$$O(\mathbf{g}) = \sum_{j=1}^{N} (\boldsymbol{\mu}_j^{\perp}) \exp(i\mathbf{g} \cdot \mathbf{r}_j) \tag{6.51}$$

In this work, explicit expressions for torques are not needed, as only induced dipole moments are simulated.

Computational aspects of Ewald Summation

As previously stated, Ewald summation is a technique used to overcome difficulties associated with the interaction range, system size and convergence of interaction sums in many-particle computer simulations. These difficulties are also closely related to the computational efficiency. Here we shortly comment on these aspects.

The convergence of the Ewald sum is controlled by the parameter α, which is usually chosen in such a way that only interactions between particles with distances smaller than half the central simulation cell $r_c^{EW} = L/2$ have to be calculated in real space. The actual value $\alpha = 6.5/L$ we are using also determines the maximum number of lattice vectors $m_{max} = \sqrt{m_x^2 + m_y^2}$ we had to take into account. Including

lattice vectors up to $m_{max} \approx 30$ (depending on the studied particle numbers $N \in [512, 1024]$) ensures, that the dipole-dipole interaction decays to values smaller than $10^{-6} k_B T$.

Transferring parts of the summation into reciprocal space is, in addition to the absolute convergence, also much faster than calculating everything in real space. In the two-dimensional setups we are considering, one can additionally take advantage out of certain symmetries. For example, the periodic image with $\mathbf{g} = (1, 0)2\pi/L$ yields the same contribution to the Ewald sum as the one with $\mathbf{g} = (0, 1)2\pi/L$.

Furthermore, the quantities $N(\mathbf{g})$ and $O(\mathbf{g})$ defined in Eqs. 6.50 and 6.51 are single particle sums, meaning that its is only $2N$ terms which need to be calculated instead of N^2. This results in a tremendous speed up of the simulation and allows larger systems sizes and/or particle numbers.

Finally, the fact that the Fourier contributions are essentially single particle sums allows to use simple and straight forward parallelization methods like OpenMP when using the programming languages C or C++. Especially on quad-, hex- or octa-core computer systems with shared memory such methods are easy to apply and show significant reduction in simulation time.

Bibliography

[1] Glotzer Sharon C. and Solomon Michael J. Anisotropy of building blocks and their assembly into complex structures. *Nat Mater*, 6(7):557–562, aug 2007. 10.1038/nmat1949.

[2] Jelena Jordanovic, Sebastian Jäger, and Sabine H. L. Klapp. Crossover from normal to anomalous diffusion in systems of field-aligned dipolar particles. *Phys. Rev. Lett.*, 106:038301, Jan 2011.

[3] Stefano Scanna, Laura Rossi, and David J. Pine. Magnetic click colloidal assembly. *Journal of the American Chemical Society*, 134(14):6112–6115, 2012.

[4] Yufeng Wang, Yu Wang, Dana R. Breed, Vinothan N. Manoharan, Lang Feng, Andrew D. Hollingsworth, Marcus Weck, and David J. Pine. Colloids with valence and specific directional bonding. *Nature*, 491(7422):51–55, 2012.

[5] Randall M. Erb, Nathan J. Jenness, Robert L. Clark, and Benjamin B. Yellen. Towards holonomic control of janus particles in optomagnetic traps. *Advanced Materials*, 21(47):4825–4829, 2009.

[6] Yan Jing, Bloom Moses, Bae Sung Chul, Luijten Erik, and Granick Steve. Linking synchronization to self-assembly using magnetic Janus colloids. *Nature*, 491(7425):578–581, nov 2012. 10.1038/nature11619.

[7] J. K. G. Dhont. An introduction to dynamics of colloids. *Elsevier*, (Amsterdam), 2003.

[8] Emanuela Bianchi, Gerhard Kahl, Christos N Likos, and Francesco Sciortino. Patchy particles. *Journal of Physics: Condensed Matter*, 27(23):230301, 2015.

[9] Woltman Scott J., Jay Gregory D., and Crawford Gregory P. Liquid-crystal materials find a new order in biomedical applications. *Nat Mater*, 6(12):929–938, dec 2007. 10.1038/nmat2010.

[10] Joe W. Tavacoli, Pierre Bauer, Marc Fermigier, Denis Bartolo, Julien Heuvingh, and Olivia du Roure. The fabrication and di-

rected self-assembly of micron-sized superparamagnetic nonspherical particles. *Soft Matter*, 9:9103–9110, 2013.

[11] Pietro Tierno. Recent advances in anisotropic magnetic colloids: realization, assembly and applications. *Phys. Chem. Chem. Phys.*, 16:23515–23528, 2014.

[12] C. Wyatt Shields IV, Shan Zhu, Ye Yang, Bhuvnesh Bharti, Jonathan Liu, Benjamin B. Yellen, Orlin D. Velev, and Gabriel P. Lopez. Field-directed assembly of patchy anisotropic microparticles with defined shape. *Soft Matter*, 9:9219–9229, 2013.

[13] Denis Rodríguez-Fernández and Luis M. Liz-Marzán. Metallic janus and patchy particles. *Particle and Particle Systems Characterization*, 30(1):46–60, 2013.

[14] Andreas Walther and Axel H. E. Müller. Janus particles. *Soft Matter*, 4(5):663–668, 2008.

[15] Sumit Gangwal, Olivier J. Cayre, and Orlin D. Velev. Dielectrophoretic assembly of metallodielectric janus particles in ac electric fields. *Langmuir*, 24(23):13312–13320, 2008.

[16] Ivo Buttinoni, Julian Bialké, Felix Kümmel, Hartmut Löwen, Clemens Bechinger, and Thomas Speck. Dynamical clustering and phase separation in suspensions of self-propelled colloidal particles. *Phys. Rev. Lett.*, 110:238301, Jun 2013.

[17] Gerald Rosenthal, Keith E. Gubbins, and Sabine H. L. Klapp. Self-assembly of model amphiphilic janus particles. *The Journal of Chemical Physics*, 136(17):174901, 2012.

[18] Ankit Kumar, Bum Jun Park, Fuquan Tu, and Daeyeon Lee. Amphiphilic janus particles at fluid interfaces. *Soft Matter*, 9:6604–6617, 2013.

[19] Yusei Kobayashi and Noriyoshi Arai. Self-assembly of janus nanoparticles with a hydrophobic hemisphere in nanotubes. *Soft Matter*, pages –, 2015.

[20] Pietro Tierno, Sathavaram V. Reddy, Michael G. Roper, Tom H. Johansen, , and Thomas M. Fischer. Transport and separation of biomolecular cargo on paramagnetic colloidal particles in a magnetic ratchet. *The Journal of Physical Chemistry B*, 112(12):3833–3837, 2008. PMID: 18318526.

[21] Jones Matthew R. and Mirkin Chad A. Materials science: Self-assembly gets new direction. *Nature*, 491(7422):42–43, nov 2012. 10.1038/491042a.

[22] J.-J. Weis. Simulation of quasi-two-dimensional dipolar systems. *Journal of Physics: Condensed Matter*, 55(15):1471, 2003.

[23] Fuduo Ma, David T. Wu, and Ning Wu. Formation of colloidal molecules induced by alternating-current electric fields. *Journal of the American Chemical Society*, 135(21):7839–7842, 2013.

[24] S. O. Lumsdon, E. W. Kaler, and O. D. Velev. Two-dimensional crystallization of microspheres by a coplanar ac electric field. *Langmuir*, 20(6):2108–2116, 2004.

[25] Bhuvnesh Bharti and Orlin D. Velev. Assembly of reconfigurable colloidal structures by multidirectional field-induced interactions. *Langmuir*, 31(29):7897–7908, 2015.

[26] Sumit Gangwal, Amar Pawar, Ilona Kretzschmar, and Orlin D. Velev. Programmed assembly of metallodielectric patchy particles in external ac electric fields. *Soft Matter*, 6(6):1413–1418, 2010.

[27] Marco Klinkigt, Rudolf Weeber, Sofia Kantorovich, and Christian Holm. Cluster formation in systems of shifted-dipole particles. *Soft Matter*, 9:3535–3546, 2013.

[28] Aleksey Ruditskiy, Bin Ren, and Ilona Kretzschmar. Behaviour of iron oxide (fe304) janus particles in overlapping external ac electric and static magnetic fields. *Soft Matter*, 9(38):9174–9181, 2013.

[29] Hartmut Löwen. Colloidal dispersions in external fields: recent developments. *J. Phys.: Condens. Matter*, 20(20):404201, 2008.

[30] Tassilo Ott, Hartmut Löwen, and M. Bonitz. Dynamics of two-dimensional one-component and binary yukawa systems in a magnetic field. *Phys. Rev. E*, 89:013105, Jan 2014.

[31] Eric M. Furst. Directed self-assembly. *Soft Matter*, 9:9039–9045, 2013.

[32] S. Elborai, D.-K. Kim, X. He, S.-H. Lee, S. Rhodes, and M. Zahn. Self-forming, quasi-two-dimensional, magnetic-fluid patterns with applied in-plane-rotating and dc-axial magnetic fields. *Journal of Applied Physics*, 97(10):10Q303, 2005.

[33] Anit Dawar and Amita Chandra. Electric field driven fractal growth dynamics in polymeric medium. *Physics Letters A*, 378(40):2951–2958, 2014.

[34] Michael J. Solomon. Directions for targeted self-assembly of anisotropic colloids from statistical thermodynamics. *Current Opinion in Colloid & Interface Science*, 16(2):158–167, 2011.

[35] G. De Magistris and D. Marenduzzo. An introduction to the physics of active matter. *Physica A: Statistical Mechanics and*

its Applications, 418:65 – 77, 2015. Proceedings of the 13th International Summer School on Fundamental Problems in Statistical Physics.

[36] Yashodhan Hatwalne, Sriram Ramaswamy, Madan Rao, and R. Aditi Simha. Rheology of active-particle suspensions. *Phys. Rev. Lett.*, 92:118101, Mar 2004.

[37] Browne Wesley R. and Feringa Ben L. Making molecular machines work. *Nat Nano*, 1(1):25–35, oct 2006. 10.1038/nnano.2006.45.

[38] Andrew Cressman, Yuichi Togashi, Alexander S. Mikhailov, and Raymond Kapral. Mesoscale modeling of molecular machines: Cyclic dynamics and hydrodynamical fluctuations. *Phys. Rev. E*, 77:050901, May 2008.

[39] M. E. Cates and J. Tailleur. When are active brownian particles and run-and-tumble particles equivalent? consequences for motility induced phase separation. *Eur. Phys. Lett.*, 101:20010, 2013.

[40] Igor S. Aranson. Collective behavior in out-of-equilibrium colloidal suspensions. *Comptes Rendus Physique*, 14(6):518 – 527, 2013. Living fluids / Fluides vivants.

[41] S. Jäger and S. H. L. Klapp. Pattern formation of dipolar colloids in rotating fields: layering and synchronization. *Soft Matter*, 7:6606, 2011.

[42] K. Lichtner and S. H. L. Klapp. Novel structure formation of a phase separating colloidal fluid in a ratchet potential. *Europhys. Lett.*, 106:56004, 2014.

[43] Dmitry Borin, Andrey Zubarev, Dmitry Chirikov, Robert Müller, and Stefan Odenbach. Ferrofluid with clustered iron nanoparticles: Slow relaxation of rheological properties under joint action of shear flow and magnetic field. *Journal of Magnetism and Magnetic Materials*, 323(10):1273 – 1277, 2011. Proceedings of 12th International Conference on Magnetic Fluid.

[44] Jason J. Benkoski, Jennifer L. Breidenich, O. Manuel Uy, Allen T. Hayes, Ryan M. Deacon, H. Bruce Land, Jane M. Spicer, Pei Yuin Keng, and Jeffrey Pyun. Dipolar organization and magnetic actuation of flagella-like nanoparticle assemblies. *J. Mater. Chem.*, 21:7314–7325, 2011.

[45] A. Snezhko, M. Belkin, I. S. Aranson, and W.-K. Kwok. Self-assembled magnetic surface swimmers. *Phys. Rev. Lett.*, 102:118103, Mar 2009.

[46] T. Glanz and H. Löwen. The nature of the laning transition in two dimensions. *Journal of Physics: Condensed Matter*, 24(46):464114, 2012.

[47] Stephen J. Ebbens and Jonathan R. Howse. In pursuit of propulsion at the nanoscale. *Soft Matter*, 6:726–738, 2010.

[48] Dreyfus Remi, Baudry Jean, Roper Marcus L., Fermigier Marc, Stone Howard A., and Bibette Jerome. Microscopic artificial swimmers. *Nature*, 437(7060):862–865, oct 2005. 10.1038/nature04090.

[49] Shradha Mishra and Sriram Ramaswamy. Active nematics are intrinsically phase separated. *Phys. Rev. Lett.*, 97:090602, Aug 2006.

[50] Xiaogang Yang and Qi Wang. Role of the active viscosity and self-propelling speed in channel flows of active polar liquid crystals. *Soft Matter*, pages –, 2016.

[51] Jonathan R. Howse, Richard A. L. Jones, Anthony J. Ryan, Tim Gough, Reza Vafabakhsh, and Ramin Golestanian. Self-motile colloidal particles: From directed propulsion to random walk. *Phys. Rev. Lett.*, 99:048102, Jul 2007.

[52] Ramin Golestanian. Collective behavior of thermally active colloids. *Phys. Rev. Lett.*, 108:038303, Jan 2012.

[53] Hong-Ren Jiang, Natsuhiko Yoshinaga, and Masaki Sano. Active motion of a janus particle by self-thermophoresis in a defocused laser beam. *Phys. Rev. Lett.*, 105:268302, Dec 2010.

[54] Alicia M. Boymelgreen and Touvia Miloh. Alternating current induced-charge electrophoresis of leaky dielectric janus particles. *Physics of Fluids*, 24(8):082003–082003, 2012.

[55] Sumit Gangwal, Olivier J. Cayre, Martin Z. Bazant, and Orlin D. Velev. Induced-charge electrophoresis of metallodielectric particles. *Phys. Rev. Lett.*, 100:058302, Feb 2008.

[56] J. Elgeti, R. G. Winkler, and G. Gompper. Physics of microswimmers—single particle motion and collective behavior: a review. *Reports on Progress in Physics*, 78(5):056601, 2015.

[57] Tamás Vicsek and Anna Zafeiris. Collective motion. *Physics Reports*, 517(3–4):71 – 140, 2012. Collective motion.

[58] Julian Bialké, Thomas Speck, and Hartmut L˙ Active colloidal suspensions: Clustering and phase behavior. *Journal of Non-Crystalline Solids*, 407:367 – 375, 2015. 7th IDMRCS: Relaxation in Complex Systems.

[59] Tamás Vicsek, András Czirók, Eshel Ben-Jacob, Inon Cohen, and Ofer Shochet. Novel type of phase transition in a system

of self-driven particles. *Phys. Rev. Lett.*, 75:1226–1229, Aug 1995.

[60] Udo Erdmann, Werner Ebeling, and Alexander S. Mikhailov. Noise-induced transition from translational to rotational motion of swarms. *Phys. Rev. E*, 71:051904, May 2005.

[61] Romanczuk, P., Bär, M., Ebeling, W., Lindner, B., and Schimansky-Geier, L. Active brownian particles. *Eur. Phys. J. Special Topics*, 202:1–162, 2012.

[62] H. Chaté, F. Ginelli, G. Grégoire, F. Peruani, and F. Raynaud. Modeling collective motion: variations on the vicsek model. *The European Physical Journal B*, 64(3-4):451–456, 2008.

[63] Gabriel Baglietto and Ezequiel V. Albano. Nature of the order-disorder transition in the vicsek model for the collective motion of self-propelled particles. *Phys. Rev. E*, 80:050103, Nov 2009.

[64] Julian Bialké, Thomas Speck, and Hartmut Löwen. Crystallization in a dense suspension of self-propelled particles. *Phys. Rev. Lett.*, 108:168301, Apr 2012.

[65] J. Dzubiella and H. Löwen. Pattern formation in driven colloidal mixtures: tilted driving forces and re-entrant crystal freezing. *J. Phys.: Condens. Matter*, 14(40):9383, 2002.

[66] Dirk Helbing, Illés J. Farkas, and Tamás Vicsek. Freezing by heating in a driven mesoscopic system. *Phys. Rev. Lett.*, 84:1240–1243, Feb 2000.

[67] Robert Großmann, Pawel Romanczuk, Markus Bär, and Lutz Schimansky-Geier. Vortex arrays and mesoscale turbulence of self-propelled particles. *Phys. Rev. Lett.*, 113:258104, Dec 2014.

[68] I. Theurkauff, C. Cottin-Bizonne, J. Palacci, C. Ybert, and L. Bocquet. Dynamic clustering in active colloidal suspensions with chemical signaling. *Phys. Rev. Lett.*, 108:268303, Jun 2012.

[69] A. Cacciuto M. E. Cates D. Marenduzzo A. N. Morozov J. Schwarz-Linek, C. Valeriani and W. C. K. Poon. Phase separation and rotor self-assembly in active particle suspensions. *PNAS*, 109(11):4052–4057, 2012.

[70] Gabriel S. Redner, Michael F. Hagan, and Aparna Baskaran. Structure and dynamics of a phase-separating active colloidal fluid. *Phys. Rev. Lett.*, 110:055701, Jan 2013.

[71] Gabriel S. Redner, Aparna Baskaran, and Michael F. Hagan. Reentrant phase behavior in active colloids with attraction. *Phys. Rev. E*, 88:012305, Jul 2013.

[72] Ethayaraja Mani and Hartmut Löwen. Effect of self-propulsion on equilibrium clustering. *Phys. Rev. E*, 92:032301, Sep 2015.

[73] Yaouen Fily and M. Cristina Marchetti. Athermal phase separation of self-propelled particles with no alignment. *Phys. Rev. Lett.*, 108:235702, Jun 2012.

[74] T. F. F. Farage, P. Krinninger, and J. M. Brader. Effective interactions in active brownian suspensions. *Phys. Rev. E*, 91:042310, Apr 2015.

[75] Thomas Speck, Julian Bialké, Andreas M. Menzel, and Hartmut Löwen. Effective cahn-hilliard equation for the phase separation of active brownian particles. *Phys. Rev. Lett.*, 112:218304, May 2014.

[76] Félix Ginot, Isaac Theurkauff, Demian Levis, Christophe Ybert, Lydéric Bocquet, Ludovic Berthier, and Cécile Cottin-Bizonne. Nonequilibrium equation of state in suspensions of active colloids. *Phys. Rev. X*, 5:011004, Jan 2015.

[77] S. C. Takatori and J. F. Brady. Towards a thermodynamics of active matter. *Phys. Rev. E*, 91:032117, Mar 2015.

[78] Julian Bialké, Jonathan T. Siebert, Hartmut Löwen, and Thomas Speck. Negative interfacial tension in phase-separated active brownian particles. *Phys. Rev. Lett.*, 115:098301, Aug 2015.

[79] Andreas Kaiser, Katarina Popowa, and Hartmut Löwen. Active dipole clusters: From helical motion to fission. *Phys. Rev. E*, 92:012301, Jul 2015.

[80] J. Dzubiella, G. P. Hoffmann, and H. Löwen. Lane formation in colloidal mixtures driven by an external field. *Phys. Rev. E*, 65:021402, Jan 2002.

[81] Leunissen Mirjam E., Christova Christina G., Hynninen Antti-Pekka, Royall C. Patrick, Campbell Andrew I., Imhof Arnout, Dijkstra Marjolein, van Roij Rene, and van Blaaderen Alfons. Ionic colloidal crystals of oppositely charged particles. *Nature*, 437(7056):235–240, sep 2005. 10.1038/nature03946.

[82] Teun Vissers, Adam Wysocki, Martin Rex, Hartmut Lowen, C. Patrick Royall, Arnout Imhof, and Alfons van Blaaderen. Lane formation in driven mixtures of oppositely charged colloids. *Soft Matter*, 7:2352–2356, 2011.

[83] Roland. R. Netz. Conduction and diffusion in two-dimensional electrolytes. *Europhys. Lett.*, 63:616, 2003.

[84] K R Sütterlin, A Wysocki, C Räth, A V Ivlev, H M Thomas, S Khrapak, S Zhdanov, M Rubin-Zuzic, W J Goedheer, V E

Fortov, A M Lipaev, V I Molotkov, O F Petrov, G E Morfill, and H Löwen. Non-equilibrium phase transitions in complex plasma. *Plasma Physics and Controlled Fusion*, 52(12):124042, 2010.

[85] C.-R. Du, K. R. Sütterlin, A. V. Ivlev, H. M. Thomas, and G. E. Morfill. Model experiment for studying lane formation in binary complex plasmas. *Europhys. Lett.*, 99(4):45001, 2012.

[86] K. R. Sütterlin, A. Wysocki, A. V. Ivlev, C. Räth, H. M. Thomas, M. Rubin-Zuzic, W. J. Goedheer, V. E. Fortov, A. M. Lipaev, V. I. Molotkov, O. F. Petrov, G. E. Morfill, and H. Löwen. Dynamics of lane formation in driven binary complex plasmas. *Phys. Rev. Lett.*, 102:085003, Feb 2009.

[87] K. Jiang, C.-R. Du, K. R. Sütterlin, A. V. Ivlev, and G. E. Morfill. Lane formation in binary complex plasmas: Role of non-additive interactions and initial configurations. *EPL (Europhysics Letters)*, 92(6):65002, 2010.

[88] V. E. Fortov and G. E. Morfill. Strongly coupled dusty plasmas on iss: experimental results and theoretical explanation. *Plasma Physics and Controlled Fusion*, 54(12):124040, 2012.

[89] A. M. Menzel. Unidirectional laning and migrating cluster crystals in confined self-propelled particle systems. *Journal of Physics: Condensed Matter*, 25(50):505103, 2013.

[90] I. D. Couzin and N. R. Franks. Self-organized lane formation and optimized traffic flow in army ants. *Proceedings of the Royal Society of London B: Biological Sciences*, 270(1511):139–146, 2003.

[91] Dzubiella J. Chakrabarti J. and Löwen H. Reentrance effect in the lane formation of driven colloids. *Physical Review E*, 70(1):012401, 2004.

[92] M. Rex and H. Löwen. Influence of hydrodynamic interactions on lane formation in oppositely charged driven colloids. *The European Physical Journal E*, 26(1-2):143–150, 2008.

[93] Masahiro Ikeda, Hirofumi Wada, and Hisao Hayakawa. Instabilities and turbulence-like dynamics in an oppositely driven binary particle mixture. *Europhys. Lett.*, 99(6):68005, 2012.

[94] H. Ohta. Lane formation in a lattice model for oppositely driven binary particles. *EPL (Europhysics Letters)*, 99(4):40006, 2012.

[95] Heiko Schmidle, Sebastian Jäger, Carol K. Hall, Orlin D. Velev, and Sabine H. L. Klapp. Two-dimensional colloidal networks induced by a uni-axial external field. *Soft Matter*, 9(9):2518–2524, 2013.

[96] Martin Z. Bazant and Todd M. Squires. Induced-charge electrokinetic phenomena: Theory and microfluidic applications. *Phys. Rev. Lett.*, 92:066101, Feb 2004.

[97] Sciortino Francesco. Disordered materials: One liquid, two glasses. *Nat Mater*, 1(3):145–146, nov 2002. 10.1038/nmat752.

[98] Julie Byrom and Sibani Lisa Biswal. Magnetic field directed assembly of two-dimensional fractal colloidal aggregates. *Soft Matter*, 9(9):9167–9173, 2013.

[99] Rajesh Ganapathy, Mark R. Buckley, Sharon J. Gerbode, and Itai Cohen. Direct measurements of island growth and step-edge barriers in colloidal epitaxy. *Science*, 327(5964):445–448, 2010.

[100] Bommel S., Kleppmann N., Weber C., Spranger H., Schäfer P., Novak J., Roth S.V., Schreiber F., Klapp S.H.L., and Kowarik S. Unravelling the multilayer growth of the fullerene C60 in real time. *Nat Commun*, 5, nov 2014.

[101] E. Zaccarelli. Colloidal gels: equilibrium and non-equilibrium routes. *J. Phys.: Condens. Matter.*, 19(32):323101, 2007.

[102] Amar B. Pawar and Ilona Kretzschmar. Fabrication, assembly, and application of patchy particles. *Macromolecular Rapid Communications*, 31(2):150–168, 2010.

[103] E. Bianchi, J. Largo, P. Tartaglia, E. Zaccarelli, and F. Sciortino. Phase diagram of patchy colloids: Towards empty liquids. *Phys. Rev. Lett.*, 97(16):168301, 2006.

[104] T. Tlusty and S. A. Safran. Defect-induced phase separation in dipolar fluids. *Science*, 290(5495):1328–1331, 2000.

[105] J. Russo, J. M. Tavares, P. I. C. Teixeira, M. M. Telo da Gama, and F. Sciortino. Reentrant phase diagram of network fluids. *Phys. Rev. Lett.*, 106(106):085703, 2011.

[106] Mark A. Miller, Ronald Blaak, Craig N. Lumb, and Jean-Pierre Hansen. Dynamical arrest in low density dipolar colloidal gels. *The Journal of Chemical Physics*, 130(11):–, 2009.

[107] R. Blaak, M. A. Miller, and J.-P. Hansen. Reversible gelation and dynamical arrest of dipolar colloids. *EPL (Europhysics Letters)*, 78(2):26002, 2007.

[108] H. Schmidle, C. K. Hall, O. D. Velev, and S. H. L. Klapp. Phase diagram of two-dimensional systems of dipole-like colloids. *Soft Matter*, 8(8):1521–1531, 2012.

[109] Lorenzo Rovigatti, John Russo, and Francesco Sciortino. No

evidence of gas-liquid coexistence in dipolar hard spheres. *Phys. Rev. Lett.*, 107:237801, Nov 2011.

[110] Zhan-Wei Li, You-Liang Zhu, Zhong-Yuan Lu, and Zhao-Yan Sun. A versatile model for soft patchy particles with various patch arrangements. *Soft Matter*, pages –, 2015.

[111] Florian Kogler, Orlin D. Velev, Carol K. Hall, and Sabine H. L. Klapp. Generic model for tunable colloidal aggregation in multidirectional fields. *Soft Matter*, 11:7356–7366, 2015.

[112] Peter J. Lu, Jacinta C. Conrad, Hans M. Wyss, Andrew B. Schofield, and David A. Weitz. Fluids of clusters in attractive colloids. *Phys. Rev. Lett.*, 96:028306, Jan 2006.

[113] Rui Zhang, Prateek K. Jhab, and Monica Olvera de la Cruz. Non-equilibrium ionic assemblies of oppositely charged nanoparticle. *Soft Matter*, 9(20):5042–5051, 2013.

[114] Lisa J. Teece, Malcolm A. Faers, and Paul Bartlett. Ageing and collapse in gels with long-range attractions. *Soft Matter*, 7:1341–1351, 2011.

[115] Florian Johannes Maier and Thomas Martin Fischer. Critical nucleation mesh-size of coarsening transient colloidal networks. *Soft Matter*, pages –, 2015.

[116] Clair R. Seager and Thomas G. Mason. Slippery diffusion-limited aggregation. *Physical Review E*, 75(1):011406, 2007.

[117] Isadora R. Nogueira, Sidiney G. Alves, and Silvio C. Ferreira. Scaling laws in the diffusion limited aggregation of persistent random walkers. *Physica A: Statistical Mechanics and its Applications*, 390(23–24):4087 – 4094, 2011.

[118] S. G. Alves and S. C. Ferreira. Aggregation in a mixture of brownian and ballistic wandering particles. *Phys. Rev. E*, 73:051401, May 2006.

[119] Susan Tolman and Paul Meakin. Off-lattice and hypercubic-lattice models for diffusion-limited aggregation in dimensionalities 2-8. *Phys. Rev. A*, 40:428–437, Jul 1989.

[120] Paul Meakin. Progress in dla research. *Physica D: Nonlinear Phenomena*, 86(2):104–112, 1995.

[121] S. Corezzi, C. De Michele, E. Zaccarelli, P. Tartaglia, and F. Sciortino. Connecting irreversible to reversible aggregation: Time and temperature. *The Journal of Physical Chemistry B*, 113(5):1233–1236, 2009.

[122] M. D. Haw, M. Sievwright, W. C. K. Poon, and P. N. Pusey. Cluster-cluster gelation with finite bond energy. *Advances in Colloid and Interface Science*, 62(1):1–16, 1995.

[123] S. Babu, J. C. Gimel, and T. Nicolai. Diffusion limited cluster aggregation with irreversible slippery bonds. *Eur. Phys. J. E*, 27(3):297–308, 2008.

[124] T. A. Witten and L. M. Sander. Diffusion-limited aggregation: a kinetic critical phenomenon. *Phys. Rev. Lett.*, 47:1400–1403, Nov 1981.

[125] Silvia Corezzi, Cristiano De Michele, Emanuela Zaccarelli, Daniele Fioretto, and Francesco Sciortino. A molecular dynamics study of chemical gelation in a patchy particle model. *Soft Matter*, 4(4):1173–1177, 2008.

[126] Silvia Corezzi, Daniele Fioretto, and Francesco Sciortino. Chemical and physical aggregation of small-functionality particles. *Soft Matter*, 8(8):11207–11216, 2012.

[127] G. Helgesen, A. T. Skjeltorp, P. M. Mors, R. Botet, and R. Jullien. Aggregation of magnetic microspheres: Experiments and simulations. *Phys. Rev. Lett.*, 61:1736–1739, Oct 1988.

[128] N. Yoshioka, Imre Varga, Ferenc Kun, Satoshi Yukawa, and Nobuyasu Ito. Attraction-limited cluster-cluster aggregation of ising dipolar particles. *Phys. Rev. E*, 72:061403, Dec 2005.

[129] Masaru Suzuki, Ferenc Kun, and Nobuyasu Ito. Cluster-cluster aggregation of ising dipolar particles under thermal noise. *Phys. Rev. E*, 80:021402, Aug 2009.

[130] M. N. Popescu, H. G. E. Hentschel, and F. Family. Anisotropic diffusion-limited aggregation. *Phys. Rev. E*, 69:061403, Jun 2004.

[131] R. C. Ball. Diffusion limited aggregation and its response to anisotropy. *Physica A: Statistical Mechanics and its Applications*, 140(1):62–69, 1986.

[132] J.-M. Jin, K. Parbhakar, L. H. Dao, and K. H. Lee. Gel formation by reversible cluster-cluster aggregation. *Phys. Rev. E*, 54:997–1000, Jul 1996.

[133] B. Bharti, F. Kogler, S. H. L. Klapp, C. K. Hall, and O. D. Velev. *preprint*.

[134] M. P. Allen and D. J. Tildesley. Computer simulation of liquids. *Oxford University Press*, (New York), 2009.

[135] D. L. Ermak. A computer simulation of charged particles in solution. i. technique and equilibrium properties. *J. Chem. Phys.*, 62(10):4189, 1975.

[136] J. P. Hansen and I. R. McDonald. Theory of simple liquids (third edition). *Academic Press*, (Burlington), 2006.

[137] M. S. Wertheim. Exact solution of the percus-yevick integral equation for hard spheres. *Phys. Rev. Lett.*, 10:321–323, 1963.

[138] M. Baus and J. L. Colot. Thermodynamics and structure of a fluid of hard rods, disks, spheres, or hyperspheres from rescaled virial expansions. *Phys. Rev. A*, 36:3912–3925, Oct 1987.

[139] X. Guo and U. Riebel. Theoretical direct correlation function for two-dimensional fluids of monodisperse hard spheres. *Journal of Chemical Physics*, 125(14):144504–144508, 2006.

[140] Franz Schwabel. Statistische mechanik. *Springer*, 1st edition, 2000.

[141] Gabriel M. Range and Sabine H. L. Klapp. Demixing in simple dipolar mixtures: Integral equation versus density functional results. *Phys. Rev. E*, 70:031201, Sep 2004.

[142] David J. Griffiths. Introduction to electrodynamics (3rd ed.). *Addison-Wesley*, 1999.

[143] Andreas Engel and Peter Reimann. Thermal ratchet effects in ferrofluids. *Phys. Rev. E*, 70:051107, Nov 2004.

[144] Martial Mazars. Long ranged interactions in computer simulations and for quasi-2d systems. *Physics Reports*, 500(2):43–116, 2011.

[145] David Griffiths. Introduction to electrodynamics. (Addison-Wesley), 2012. 4th ed.

[146] James E. Martin, Robert A. Anderson, and Rodney L. Williamson. Generating strange magnetic and dielectric interactions: Classical molecules and particle foams. *Journal of Chemical Physics*, 118(3):1557–1570, 2003.

[147] N. Osterman, I. Poberaj, J. Dobnikar, D. Frenkel, P. Ziherl, and D. Babić. Field-induced self-assembly of suspended colloidal membranes. *Phys. Rev. Lett.*, 103:228301, Nov 2009.

[148] K. Müller, N. Osterman, D. Babič, C. N. Likos, J. Dobnikar, and A. Nikoubashman. Pattern formation and coarse-graining in 2d colloids driven by multiaxial magnetic fields. *Langmuir*, 30(18):5088–5096, 2014.

[149] Maarten M. van Oene, Laura E. Dickinson, Francesco Pedaci, Mariana Köber, David Dulin, Jan Lipfert, and Nynke H. Dekker. Biological magnetometry: Torque on superparamagnetic beads in magnetic fields. *Phys. Rev. Lett.*, 114:218301, May 2015.

[150] Sabine H. L. Klapp and Martin Schoen. Reviews in computational chemistry volume 24. *John Wiley & Sons*, (New Jersey), 2007.

[151] Francesco Sciortino and Emanuela Zaccarelli. Reversible gels of patchy particles. *Current Opinion in Solid State and Materials Science*, 15(15):246–253, 2011.

[152] Amit Goyal, Carol K. Hall, and Orlin D. Velev. Phase diagram for stimulus-responsive materials containing dipolar colloidal particles. *Phys. Rev. E*, 77:031401, Mar 2008.

[153] F. Kogler and S. H. L. Klapp. Lane formation in a system of dipolar microswimmers. *EPL (Europhysics Letters)*, 110(1):10004, 2015.

[154] James M. Phillips, L. W. Bruch, and R. D. Murphy. The two-dimensional lennard-jones system: Sublimation, vaporization and melting. *J. Chem. Phys.*, 75(0):5907, 1981.

[155] B. Smit and D. Frenkel. Vapor-liquid equilibria of the tw-dimensional lennard-jones fluid(s). *J. Chem. Phys.*, 94(0):5663, 1991.

[156] John G. Kirkwood and Frank P. Buff. The statistical mechanical theory of solutions. *The Journal of Chemical Physics*, 19(6):774–777, 1951.

[157] F. L. Braga and M. S. Ribeiro. Diffusion limited aggregation: Algorithm optimization revisited. *Computer Physics Communications*, 182(8):1602–1605, 2011.

[158] Mark Newman. Networks: An introduction. (Oxford University Press), 2010. 4th ed.

[159] A. Wysocki and H. Löwen. Instability of a fluid–fluid interface in driven colloidal mixtures. *J. Phys.: Condens. Matter*, 16(14):7209, 2004.

[160] Christopher Wächtler, Florian Kogler, and Sabine H. L. Klapp. Lane formation of the two-dimensional lennard-jones fluid. 2016. In preparation.

[161] Bhuvnesh Bharti, Florian Kogler, Carol K. Hall, Sabine H. L. Klapp, and Orlin D. Velev. Multidirectional colloidal assembly in concurrent electric and magnetic fields. 2016. In preparation.

[162] Peter J. Krommenhoek and Joseph B. Tracy. Magnetic field-directed self-assembly of magnetic nanoparticle chains in bulk polymers. *Particle & Particle Systems Characterization*, 30(9):759–763, 2013.

[163] Mao Xiaoming, Chen Qian, and Granick Steve. Entropy favours open colloidal lattices. *Nat Mater*, 12(3):217–222, mar 2013. 10.1038/nmat3496.

[164] Marie-Pierre Valignat, Olivier Theodoly, John C. Crocker, William B. Russel, and Paul M. Chaikin. Reversible self-assembly and directed assembly of dna-linked micrometer-sized colloids. *PNAS*, 102(12):4225–4229, 2005.

[165] Andrew I. Campbell, Valerie J. Anderson, Jeroen S. van Duijneveldt, and Paul Bartlett. Dynamical arrest in attractive colloids: The effect of long-range repulsion. *Phys. Rev. Lett.*, 94:208301, May 2005.

[166] Oliver Pohl and Holger Stark. Dynamic clustering and chemotactic collapse of self-phoretic active particles. *Phys. Rev. Lett.*, 112:238303, Jun 2014.

[167] Jonathan K. Withmer and Erik Luijten. Influence of hydrodynamics on cluster formation in colloid-polymer mixtures. *The Journal of Physical Chemistry B*, 115(22):7294–7300, 2011.